Functional Renormalization Group Studies on Competing Orders in the Square Lattice

Von der Fakultät für Mathematik, Informatik und Naturwissenschaften der RWTH Aachen University zur Erlangung des akademischen Grades eines Doktors der Naturwissenschaften genehmigte Dissertation

vorgelegt von

Julian Lichtenstein, M.Sc.
aus Rheine

Berichter: Prof. Dr. Carsten Honerkamp
Prof. Dr. Sabine Andergassen

Tag der mündlichen Prüfung: 19.06.2018

Acknowledgments

At this point I would like to thank all the people that supported me during the years of my doctoral studies.

First of all, I thank Carsten Honerkamp for his supervision, the opportunity to work on this interesting project, and his valuable advice. In addition, I thank him for supporting my attendance at various conferences and workshops, at which I experienced many productive discussions and a fruitful scientific exchange. Sabine Andergassen is thanked for co-refereeing this thesis.

I sincerely appreciated the close cooperation with David Sánchez de la Peña and am grateful for the numerous and productive conversations we had. For the pleasant atmosphere during my time at the institute, I am thankful to my current and former colleagues Jannis Ehrlich, Michael Golor, Michael Kinza, Guido Klingschat, Maximilian Lohöfer, Stefan Maier, Timo Reckling, Giulio Schober, Stefan Uebelacker, and Jie Yuan. Daniel Rohe supported me in writing my first hybrid parallelized code and the collaboration with Edoardo Di Napoli and Jan Winkelmann provided me with many insights into high-performance computing, for which I am grateful. Moreover, the discussions with Cornelia Hille and Agnese Tagliavini on details of the method have been very helpful for me. For proofreading the manuscript of this thesis I thank Giulio Schober and David Sánchez de la Peña. The everyday workflow, including data generation and management, has greatly been facilitated by the JUBE environment [1], for which I am thankful to Sebastian Luehrs et al..

I gratefully acknowledge the computing time granted by the JARA-HPC Vergabegremium on the supercomputer JURECA [2] at Forschungszentrum Jülich and financial support through the DFG.

On the personal side, I thank my parents for their advice and I thank Katharina for her love and her support in difficult situations in life.

Abstract

In this thesis a novel computational approach for functional Renormalization Group (fRG) investigations regarding interacting fermions on two-dimensional lattices is derived. The approach is based on the exchange-parametrization fRG [3] concerning the two-fermion interaction, with additional insertions of truncated partitions of unity that are inspired by the singular-mode fRG [4]. These insertions decouple the fermionic propagators from the exchange propagators and thereby lead to a separation of the underlying equations. It is argued that this separation is numerically advantageous and may pave the way for refined, large-scale computational fRG investigations. Furthermore, on the basis of speedup data gained from an implementation of the novel scheme, it is shown that the new equation structure facilitates efficient calculations on a large number of multicore CPUs. Utilizing the methodical development, two applications are presented afterwards:

Firstly, the scheme is applied to the t-t' Hubbard model on a square lattice. In order to test the method, the convergence of the results with respect to increasing truncation length of the partition of unity is analyzed and a comparison to findings from previous fRG studies is drawn. The test yields a fast convergence in most parts of the investigated parameter range. Moreover, it was found that the older findings are approximately reproduced using a short truncation length, while quantitative corrections to the previous results are obtained using longer truncation lengths. In addition to these method focused investigations, the high momentum-space resolution of the implementation was utilized to study ordering vectors of antiferromagnetic phases. A comparison to calculations solely based on the magnetic channel revealed that the inter-channel feedback, as contained in the fRG, generates support for commensurate antiferromagnetic orderings.

The second application addresses a modified version of the previous model, in which a Coulomb-like long-range interaction term is added to the local Hubbard interaction. In this work a solution is presented on how the long-range interaction can be implemented in a momentum-space fRG scheme without encountering singularities. Afterwards, phase diagrams are given that compare the results of calculations using short- and long-ranged interactions, showing significantly lower critical scales in the long-range scenario. Finally, screening lengths are extracted from the fRG outcome and are compared to those calculated in a 'random phase approximation'. The comparison reveals quantitative differences between both

values. However, the results indicate that the charge screening is not changed qualitatively by the feedback from other channels, i.e., at van Hove filling the screening length tends to zero in both cases.

Zusammenfassung

In dieser Dissertation wird eine neuartige Herangehensweise für computergestützte Untersuchungen mittels der funktionalen Renormierungsgruppe (fRG) hergeleitet. Untersuchungsgegenstand sind dabei wechselwirkende Fermionen in zweidimensionalen Gittersystemen. Die vorgestellte Herangehensweise basiert auf der Austauschparametrisierung [3] der Zwei-Fermionen-Wechselwirkung, wobei zusätzlich Zerlegungen der Eins in die Gleichungen eingeschoben werden. Diese Einschübe, die durch die Singulärmoden-fRG [4] inspiriert sind, entkoppeln die fermionischen Propagatoren von den Austauschpropagatoren und führen dadurch zu einer Separation der zugrundeliegenden Gleichungen. Es wird argumentiert, dass diese Separation für numerische Behandlungen vorteilhaft ist und den Weg für groß angelegte, computergestützte Untersuchungen bereiten kann. Darüber hinaus wird gezeigt, dass die neue Struktur der Gleichungen effiziente Rechnungen auf einer Vielzahl von multi-Kern CPUs erleichtert. Diese Aussage beruht auf Laufzeit-Daten einer Implementierung der neuen Methode. Danach werden zwei Anwendungen präsentiert, die unter Verwendung der methodischen Weiterentwicklung durchgeführt worden sind:

Zunächst wird die Methode auf das t-t'-Hubbard-Modell auf einem Quadratgitter angewendet. Um hierbei die Methode zu testen, werden die Resultate auf Konvergenz bezüglich zunehmender Trunkierungslänge der zerlegten Einsen analysiert und es wird ein Vergleich zu Ergebnissen früherer fRG-Studien gezogen. Dabei hat sich in einem Großteil des untersuchten Parameterbereichs gutes Konvergenzverhalten gezeigt. Desweiteren konnten die Ergebnisse der früheren Studien näherungsweise reproduziert werden, wenn eine kurze Trunkierungslänge eingestellt worden ist. Größere Trunkierungslängen ergeben daher quantitative Korrekturen zu den früheren Resultaten. Zusätzlich zu diesen Untersuchungen, die auf die Methode selbst fokussiert sind, wird die hohe Impulsraum-Auflösung der Implementierung genutzt, um Ordnungsvektoren von antiferromagnetischen Phasen zu betrachten. Ein Vergleich mit Berechnungen, die einzig auf dem magnetischen Kanal beruhen, hat ergeben, dass die in der fRG enthaltene Rückwirkung der anderen Kanäle eine kommensurable Ausprägung antiferromagnetischer Ordnung unterstützt.

Die zweite Anwendung behandelt eine modifizierte Version des vorherigen Modells, bei der ein Coulomb-artiger Wechselwirkungsterm mit langer Reichweite zur lokalen Hubbard-Wechselwirkung hinzugefügt wird. Zunächst wird eine

Lösung präsentiert, wie eine solche Wechselwirkung in einer Impulsraum-fRG betrachtet werden kann, ohne dass Singularitäten auftreten. Danach werden anhand von Phasendiagrammen die Ergebnisse von Rechnungen mit kurz- und langreichweitigen Wechselwirkungen verglichen. Dabei zeigen sich für die Wechselwirkung mit langer Reichweite signifikant tiefere kritische Skalen. Abschließend sind Screening-Längen aus den fRG-Daten extrahiert und mit denen einer ‚Random Phase Approximation' verglichen worden. Der Vergleich zeigt quantitative Unterschiede zwischen diesen beiden Werten, jedoch deuten die Ergebnisse darauf hin, dass sich das Screening der Ladungswechselwirkung qualitativ nicht ändert, wenn die Rückwirkung der anderen Kanäle miteinbezogen wird. Das heißt, dass die Screening-Länge bei van-Hove-Füllung in beiden Fällen gegen null geht.

Contents

Chapter 1.

Introduction

In recent decades, the study of materials in terms of their low-temperature properties has been an active field of research in condensed-matter physics. Many of these properties, such as magnetism and superconductivity, arise from astonishing states of the material's electronic structure. While the fundamental laws that describe an interacting electron are well known and can be used to set up a microscopic model for a solid's electronic system, these laws do not reveal the nature of a macroscopic object containing an almost endless number of electrons interacting with each other. As P. W. Anderson pointed out in his prominent article 'More Is Different' (Ref. [5])—while providing a more general perspective on the hierarchical structure of science—, the state of a macroscopic system can only be understood as the consequence of the electrons' collective behavior rather than as a sum of contributions from single constituents. Consequently, effective descriptions based on adapted degrees of freedom, e.g., Ginzburg-Landau theory for superconductivity, are essential. Thus, the question arises how the most relevant degrees of freedom that effectively describe the electronic system can be revealed or, in other words, how the low-temperature state of a material can be determined.

Answering the above question is a topic of current research. Even though microscopic models that only consider electronic excitations in a smaller energy window around the Fermi level are often unsuitable for directly reading off material properties with quantitative precision, they serve as a good starting point for theoretical investigations regarding collective states. In view of a particular investigation there are basically two different ways to obtain an appropriate model: In a study that focuses on certain materials, a comparison of those, or on aspects like the influence of material-specific details contained in the electronic structure, a model calculated by density-functional theory is an advisable choice. By contrast, in other cases in which the study is, for instance, guided by the idea of abstraction, simplified models that are specified by only a few parameters are useful. Such models are intended to be reduced versions of more complex ones while preserving the features that are essential for the low-temperature behavior. One of the simplest models which, at the same time, contains a big variety of

many-fermion phenomena is the Hubbard model on the square lattice. Although it was initially introduced in the three independent works [6–8] in 1963, large interest in this model awoke in 1987 when P. W. Anderson related it to the then new high-temperature superconductivity in La_2CuO_4 based cuprates (see Ref. [9]).[1]

In order to study microscopic models in terms of their low-temperature properties, one has to apply a suitable method for investigations on fermionic many-body systems. Exact methods, such as Quantum Monte Carlo (QMC), are available but limited in applicability. For instance, in a QMC treatment many interesting models lead to the so-called 'sign problem' resulting in an exponentially growing statistical error with respect to increasing particle number. In contrast, within the framework provided by the functional Renormalization Group it is possible to investigate a broad scope of models without restrictions to specific parameter values.[2] Renormalization Group (RG) methods directly connect the microscopic description to an effective one by successive inclusion of contributions originating from the electrons' collective behavior. This procedure is controlled by a scale parameter that separates the modes that are already included from the ones that are not yet contained in the effective values. Changes in the effective theory with respect to variations of the scale parameter are described by RG equations. Functional RG (fRG) approaches formulate the RG idea (see Ref. [11] for the original formulation) in terms of generating functionals for many-particle Green or vertex functions. By expanding the used functional in the external source fields one obtains a full hierarchy of RG equations for the respective type (Green or vertex) of function. In recent years, especially the formulation based on the generator for one-particle irreducible (1PI) vertices has brought many insights regarding a variety of different model systems (cf. the reviews [12, 13]). The latter fRG version was originally introduced by C. Wetterich (Ref. [14]) for investigations on bosonic systems, while a fermionic version was presented later by M. Salmhofer and C. Honerkamp in Ref. [15]. Formally, the 1PI fRG connects the microscopic action of the model system with an effective one via a trajectory that is parametrized by the scale parameter. Although the scheme provides an exact hierarchy of RG equations for all orders of vertex functions, truncations of that hierarchy are unavoidable in practical calculations. A commonly used form is the 'level-two truncation' in which, as a consequence of the truncation, the validity of the method is limited to weakly coupled fermions. However, besides the renormalization of the two-particle vertex, the self-energy feedback can be treated conveniently within this scheme. Furthermore, the contributions that may lead to instabilities of the Fermi liquid in two dimensions are already included on a one-loop level and are

[1] Actually, the general relevance of the Hubbard model for unconventional superconductivity induced rather by electronic and magnetic fluctuations than by phonons had already been investigated somewhat before—albeit for three-dimensional materials with much smaller critical temperatures (see Ref. [10]).

[2] Although the full set of fRG equations provides an analytically exact methodical framework, the truncated versions that are used for the actual computations only yield approximate results.

treated on equal footing, i.e., the method is unbiased regarding different kinds of ordered states.

Since its first application to an interacting Fermi system, published in 2001 (see Ref. [16]), the 1PI fRG has been refined and developed further. On a formal level, there have been works that addressed an efficient parametrization of the two-particle vertex in combination with a restructuring of the equations (cf. Refs. [3, 4, 17]) and, moreover, it was found that the inaccuracies arising from the level-two truncation are reduced by a slight modification of the remaining equations (cf. Ref. [18]). Complementarily, on the technical side it was demonstrated in Ref. [19] that the fRG can profit highly from massively parallel computing architectures, provided that a program code is used that implements a sophisticated parallelization strategy. However, the development process is far from being completed. In view of predictions of critical temperatures and gap sizes the fRG still lacks quantitative accuracy. In order to pave the way for investigations on existing materials in terms of their ground state properties with quantitative precision, regarding energy scales and parameter ranges, as well as for discovering new materials with superior features, method development has to combine both aspects mentioned above: improvements on the formal level and sophisticated usage of high-performance computers. In this thesis I report on recent progress in the method development achieved by focusing on both aspects.

This thesis is organized as follows:

In order to clarify the notation and to define the starting point for the following developments, the derivation of the 1PI fRG equations is recapitulated briefly in Ch. 2. Besides the full hierarchy of equations the level-two truncation is introduced and symmetries are exploited. Furthermore, selected strategies for applying the method to model systems are described, while two of these strategies have strongly inspired the development described in the subsequent chapter.

By building on the previous achievements a novel approach with a numerically advantageous structure is derived in Ch. 3, supplemented by a discussion on its benefits compared to previous schemes. In addition, a high-performance oriented implementation of that approach is described, focusing on algorithmic choices and parallelization strategies, and speedups resulting from executions on parallel computing platforms are given.

In Ch. 4 the results from the first application of the new approach—a study of the Hubbard model on a square lattice—are presented. As the first part of this application is focused on the functionality of the approach, the model-parameter ranges are chosen according to previous fRG studies, whose results serve as comparative values. The two following questions are addressed: Is the new approach capable of reproducing the previous findings? And, provided that the answer to the first question is ‘yes’, does the current implementation allow for producing

quantitative corrections to these findings by increasing the computational accuracy? In the second part, a high momentum resolution is utilized to investigate ordering vectors in the magnetic channel.

After the application to the Hubbard model, in which the fermionic interaction is given by a purely local term, the new scheme was used to investigate the consequences of extending the model by a Coulomb-like long-range interaction. This study is presented in Ch. 5. As a first step, a solution is revealed on how the long-range interaction can be implemented in a momentum-space fRG scheme without encountering singularities. Afterwards it is illustrated how optimal values for technical parameters are obtained by conducting convergence tests in the space spanned by these parameters. Building on the preceding deliberations, the following questions are addressed: How does the additional long-range interaction term affect resulting phase diagrams? Does the charge-screening effect that the fRG contains produce finite screening lengths in cases in which the 'Random Phase Approximation' yields vanishing ones?

Finally, in Ch. 6 conclusions are drawn and an outlook is provided.

As some parts of this work have already been published in Ref. [20], the text of this introduction contains paraphrases of the one from the publication. As it is not always possible to reformulate a statement without changing its connotation, some formulations used here may be close or, in rare cases, even identical to the ones from Ref. [20].

Chapter 2.

Functional Renormalization Group

Due to the variety of different RG schemes present in the literature—including many different *functional* RG approaches—this chapter is meant to introduce that theoretical framework on which the rest of this thesis is based. The presented scheme provides a set of differential equations that describe the evolution of *one-particle irreducible (1PI)* vertices as functions of an artificial *scale parameter*. Therefore, this variant is often called 1PI fRG. In short, the fRG procedure used to study ground state properties has the following threefold structure: *(i)* The artificial scale parameter is set to an initial value that allows for a straightforward calculation of 1PI vertex functions. *(ii)* Starting from the vertices at the initial scale, the aforementioned differential equations are integrated in the direction of decreasing scale parameter. *(iii)* When predefined conditions are met, the integration is stopped and information on the system under investigation can be extracted from the resulting values of scale and vertices. The integration of differential equations in step *(ii)* is often referred to as fRG *flow*. In relation thereto, the equations themselves are called *flow equations*.

In Sec. 2.1 a derivation of the flow equations is provided. As symmetries of the investigated system can be exploited to reduce the number of independent vertex components, considerations of symmetry properties can be valuable. Sec. 2.2 addresses this topic. Subsequently, Sec. 2.3 contains a brief overview of strategies that are frequently used in the literature for applying the 1PI fRG to model systems.

2.1. 1PI FRG Flow Equations

The derivation given in this section was presented by M. Salmhofer and C. Honerkamp in 2001 (cf. Ref. [15]) and recapitulated in two review articles (cf. Refs. [12, 13]) in the more recent past. While the statements formulated in this chapter are meant to introduce notational details as well as to summarize aspects that are important in the context of this thesis, reference is made to the above mentioned papers for a more comprehensive overview. From a structural point of view the

following derivation is close to the one shown in Ref. [12], whereas the notation is also inspired by Refs. [13, 21].

This section is structured as follows: After a brief part on generating functionals, a scale (or *flow*) parameter is introduced and exact flow equations are derived. Then, a standard truncation of the resulting infinite hierarchy of differential equations is discussed and different ways of implementing the flow parameter in terms of *cutoff* schemes are presented.

2.1.1. Generating Functionals

In this section the fermionic system is described using a functional integral formulation. Considering the action

$$\mathcal{S}[\bar{\psi},\psi] = -(\bar{\psi}, G_0^{-1}\psi) + \mathcal{S}_I[\bar{\psi},\psi] \tag{2.1}$$

the partition function of the system can be written as

$$Z = \int \mathcal{D}[\bar{\psi},\psi]\, e^{-\mathcal{S}[\bar{\psi},\psi]}\,. \tag{2.2}$$

Here the term $(\bar{\psi}, G_0^{-1}\psi) = \sum_K \bar{\psi}(K)\,(G_0^{-1}\psi)(K)$ in Eq. (2.1) is a scalar product with $(G_0^{-1}\psi)(K) = \sum_{K'} G_0^{-1}(K,K')\,\psi(K')$ and $\int \mathcal{D}[\bar{\psi},\psi] = \int \prod_K d\bar{\psi}(K) d\psi(K)$ symbolizes the functional integration over the Grassmann fields $\bar{\psi}$ and ψ in Eq. (2.2). In favor of a short notation a multi-index $K = (k_0, \mathbf{k}, \sigma)$ is introduced that collects Matsubara frequency and all quantum numbers used for the single-particle description—which are momentum and spin in the case of the present thesis. As this work is focused on translation and spin-rotation invariant systems, the bare one-particle Green function $G_0(K,K') = \delta_{K,K'} G_0(K)$ is diagonal, and spin independent. The diagonal terms are given by

$$G_0(K) = \frac{1}{ik_0 - \xi(\mathbf{k})}\,, \tag{2.3}$$

in which $\xi(\mathbf{k}) = \epsilon(\mathbf{k}) - \mu$ is the energy of a particle relative to the chemical potential μ. The second part of the action in Eq. (2.1)—i.e., $\mathcal{S}_I[\bar{\psi},\psi]$—is a two-particle interaction which is quartic in the fields $\bar{\psi}$ and ψ.

The derivation of RG equations from a field theory can be done most conveniently by using generating functionals, as these objects contain the information of all orders of Green and vertex functions, respectively. By adding terms containing external source fields $\bar{\eta}$ and η to the action, the generating functional

$$\mathcal{G}[\bar{\eta},\eta] = \frac{1}{Z}\int \mathcal{D}[\bar{\psi},\psi]\, e^{-\mathcal{S}[\bar{\psi},\psi]+(\bar{\eta},\psi)+(\bar{\psi},\eta)} \tag{2.4}$$

can be constructed. It is straightforward to show that the n-particle Green function $G^{(n)}$ is obtained by conducting $2n$ derivatives with respect to the source fields and setting the external fields to zero afterwards:

$$G^{(n)}(K_1,\ldots,K_n;K_1',\ldots,K_n') = (-1)^n \left.\frac{\delta^{2n}\mathcal{G}[\bar{\eta},\eta]}{\delta\bar{\eta}(K_1)\ldots\delta\bar{\eta}(K_n)\delta\eta(K_n')\ldots\delta\eta(K_1')}\right|_{\bar{\eta}=\eta=0} . \tag{2.5}$$

While $G^{(n)}$ contains both connected and disconnected diagrams, a generator for connected Green functions $G_c^{(n)}$ is defined by

$$\mathcal{W}[\bar{\eta},\eta] = -\ln\int \mathcal{D}[\bar{\psi},\psi]\, e^{-\mathcal{S}[\bar{\psi},\psi]+(\bar{\eta},\psi)+(\bar{\psi},\eta)} . \tag{2.6}$$

Unlike the disconnected Green functions the connected ones solely sum up diagrams in which each substructure is connected via at least one interaction or propagator to all other parts of the diagram. As a next step, one defines 1PI vertex functions, which only contain diagrams that stay connected even if one propagator is cut. Using the latter diagrams as nodes, the connected ones can be seen as tree-like diagrams with all the closed propagator loops contained in the 1PI vertex nodes. Since divergences that appear in the renormalization process arise from loop integrations, the 1PI vertices play an important role in this context. In order to investigate instabilities of the normal electronic state, these functions appear as the most natural choice of an object of study. The corresponding generating functional is defined by the Legendre transform

$$\Gamma[\bar{\psi},\psi] = (\bar{\psi},\eta) + (\bar{\eta},\psi) + \mathcal{W}[\bar{\eta},\eta] , \tag{2.7}$$

with

$$\psi = -\frac{\delta\mathcal{W}}{\delta\bar{\eta}} \quad \text{and} \quad \bar{\psi} = \frac{\delta\mathcal{W}}{\delta\eta} . \tag{2.8}$$

2.1.2. Flow Parameter and Exact Flow Equations

The first step in deriving fRG flow equations is to insert a scalar flow parameter Λ into the generating functionals defined in the previous subsection. This modification should be implemented in a way that a closed expression of the functionals is known at $\Lambda = \Lambda_0$ and that the generators recover their original structure at $\Lambda = 0$. Usually, the modification is done at the level of the bare propagator by changing G_0 to G_0^Λ, with $G_0^{\Lambda=\Lambda_0} = 0$ and $G_0^{\Lambda=0} = G_0$. This replacement directly leads to parameter dependent functionals $\mathcal{G}^\Lambda$, $\mathcal{W}^\Lambda$, and Γ^Λ that recover their full structure at $\Lambda = 0$. In contrast to $\mathcal{G}^\Lambda$, and $\mathcal{W}^\Lambda$, which are zero at $\Lambda = \Lambda_0$, the 1PI vertex generator becomes

$$\Gamma^{\Lambda=\Lambda_0}[\bar{\psi},\psi] = \mathcal{S}[\bar{\psi},\psi] - (\bar{\psi},(Q_0^{\Lambda_0} - Q_0)\psi) , \tag{2.9}$$

which can be seen as the regularized form of the action from Eq. (2.1). Here, $Q_0^{(\Lambda)} = (G_0^{(\Lambda)})^{-1}$ is the inverse of the (regularized) bare propagator. This is another argument in favor of an 1PI-vertex based RG, as in this case information on the original system is already contained in the functional at the initial stage of the calculation.

In order to calculate the 1PI vertex generator at values of the flow parameter less than Λ_0, an initial value problem has to be solved with Γ^{Λ_0} serving as initial value. The corresponding differential equation is derived starting with differentiating $\mathcal{W}^\Lambda$, which yields

$$\frac{d}{d\Lambda}\mathcal{W}^\Lambda[\bar{\eta},\eta] = \left(\frac{\delta\mathcal{W}^\Lambda}{\delta\eta}, \dot{Q}_0^\Lambda \frac{\delta\mathcal{W}^\Lambda}{\delta\bar{\eta}}\right) + \mathrm{tr}\left(\dot{Q}_0^\Lambda \frac{\delta^2\mathcal{W}^\Lambda}{\delta\bar{\eta}\,\delta\eta}\right), \tag{2.10}$$

while the dot above a quantity denotes a derivative with respect to Λ. In a second step, the Λ derivative of Eq. (2.7) is performed. At this stage one has to take into account that $\bar{\eta}^\Lambda$ and η^Λ are Λ dependent themselves due to their definition in Eq. (2.8). These dependencies lead to canceling terms and, as a result, only the direct derivative of $\mathcal{W}^\Lambda$—in which $\bar{\eta}^\Lambda$ and η^Λ are held constant—is left:

$$\frac{d}{d\Lambda}\Gamma^\Lambda[\bar{\psi},\psi] = \left.\frac{d}{d\Lambda}\mathcal{W}^\Lambda[\bar{\eta}^\Lambda,\eta^\Lambda]\right|_{\bar{\eta}^\Lambda,\eta^\Lambda \text{ fixed}}. \tag{2.11}$$

Eq. (2.10) is now inserted on the right-hand side resulting in the 1PI flow equation (see Ref. [14])

$$\frac{d}{d\Lambda}\Gamma^\Lambda[\bar{\psi},\psi] = -\left(\bar{\psi}, \dot{Q}_0^\Lambda\psi\right) - \frac{1}{2}\mathrm{tr}\left(\dot{\boldsymbol{Q}}_0^\Lambda \left(\boldsymbol{\Gamma}^{(2)\Lambda}[\bar{\psi},\psi]\right)^{-1}\right), \tag{2.12}$$

with definitions

$$\boldsymbol{Q}_0^\Lambda = \begin{pmatrix} Q_0^\Lambda & 0 \\ 0 & -\left(Q_0^\Lambda\right)^t \end{pmatrix} \tag{2.13}$$

and

$$\boldsymbol{\Gamma}^{(2)\Lambda}[\bar{\psi},\psi] = \begin{pmatrix} \frac{\delta^2\Gamma^\Lambda}{\delta\bar{\psi}\,\delta\psi} & \frac{\delta^2\Gamma^\Lambda}{\delta\bar{\psi}\,\delta\bar{\psi}} \\ \frac{\delta^2\Gamma^\Lambda}{\delta\psi\,\delta\psi} & \frac{\delta^2\Gamma^\Lambda}{\delta\psi\,\delta\bar{\psi}} \end{pmatrix}. \tag{2.14}$$

In order to substitute derivatives of $\mathcal{W}^\Lambda$ with respect to the fields, Eq. (2.8) was used besides the reciprocity relation $\boldsymbol{\Gamma}^{(2)\Lambda}[\bar{\psi},\psi] = (\boldsymbol{\mathcal{W}}^{(2)\Lambda}[\bar{\eta},\eta])^{-1}$.

Based on Eq. (2.12), the flow equations for 1PI vertex functions are derived by an expansion in powers of the fields $\bar{\psi}$ and ψ followed by a comparison of coefficients. For this purpose the matrix $\boldsymbol{\Gamma}^{(2)\Lambda}$ is split into a zeroth order, field independent term and higher order terms

$$\boldsymbol{\Gamma}^{(2)\Lambda}[\bar{\psi},\psi] = \boldsymbol{\Gamma}^{(2)\Lambda}[\bar{\psi},\psi]\big|_{\bar{\psi},\psi=0} - \boldsymbol{U}^\Lambda[\bar{\psi},\psi], \tag{2.15}$$

where the first term on the right-hand side is equal to the inverse of the full propagator $\boldsymbol{G}^\Lambda = \mathrm{diag}(G^\Lambda, -(G^\Lambda)^t)$. The resulting expression for $(\boldsymbol{\Gamma}^{(2)\Lambda})^{-1}$ is expanded using the geometric series and an insertion into Eq. (2.12) yields

$$\begin{aligned}\frac{d}{d\Lambda}\Gamma^\Lambda[\bar\psi,\psi] = &-\mathrm{tr}\Big(\dot Q_0^\Lambda G^\Lambda\Big) - \Big(\bar\psi, \dot Q_0^\Lambda \psi\Big) \\ &+ \frac{1}{2}\mathrm{tr}\Big(\boldsymbol{S}^\Lambda\left(\boldsymbol{U}^\Lambda[\bar\psi,\psi] + \boldsymbol{U}^\Lambda[\bar\psi,\psi]\boldsymbol{G}^\Lambda\boldsymbol{U}^\Lambda[\bar\psi,\psi] + \dots\right)\Big)\,.\end{aligned} \tag{2.16}$$

As—at least in many cases—the object $\boldsymbol{S}^\Lambda = \mathrm{diag}(S^\Lambda, -(S^\Lambda)^t) = -\boldsymbol{G}^\Lambda\dot{\boldsymbol{Q}}_0^\Lambda\boldsymbol{G}^\Lambda$ mainly contributes at single-particle energies close to the value of Λ, it is often called *single-scale propagator*. From Eq. (2.16) the flow equations for 1PI vertex functions are identified by comparison of coefficients. It is conventional to use the self-energy Σ^Λ instead of the one-particle vertex $\Gamma^{(2)\Lambda}$, which can be reconstructed by $\Gamma^{(2)\Lambda} = Q_0^\Lambda - \Sigma^\Lambda$. Finally, the equation for Σ^Λ reads

$$\frac{d}{d\Lambda}\Sigma^\Lambda(K',K) = \sum_{\bar K,\bar K'} S^\Lambda(\bar K,\bar K')\Gamma^{(4)\Lambda}(K',\bar K';K,\bar K) \tag{2.17}$$

and a comparison of the quartic terms yields

$$\begin{aligned}&\frac{d}{d\Lambda}\Gamma^{(4)\Lambda}(K_1',K_2';K_1,K_2) = \\ &-\sum_{\bar K,\bar K'} S^\Lambda(\bar K,\bar K')\Gamma^{(6)\Lambda}(K_1',K_2',\bar K';K_1,K_2,\bar K) \\ &+\sum_{\bar K_1,\bar K_1'}\sum_{\bar K_2,\bar K_2'} G^\Lambda(\bar K_1,\bar K_1')S^\Lambda(\bar K_2,\bar K_2') \\ &\quad\times\Big[\ \Gamma^{(4)\Lambda}(K_1',K_2';\bar K_1,\bar K_2)\Gamma^{(4)\Lambda}(\bar K_1',\bar K_2';K_1,K_2) \\ &\qquad-\big[\Gamma^{(4)\Lambda}(K_1',\bar K_2';K_1,\bar K_1)\Gamma^{(4)\Lambda}(\bar K_1',K_2';\bar K_2,K_2) + (\bar K_1\leftrightarrow\bar K_2,\bar K_1'\leftrightarrow\bar K_2')\big] \\ &\qquad+\big[\Gamma^{(4)\Lambda}(K_2',\bar K_2';K_1,\bar K_1)\Gamma^{(4)\Lambda}(\bar K_1',K_1';\bar K_2,K_2) + (\bar K_1\leftrightarrow\bar K_2,\bar K_1'\leftrightarrow\bar K_2')\big]\ \Big]\,.\end{aligned} \tag{2.18}$$

From Eqs. (2.17) and (2.18)—and their diagrammatic representations in Fig. 2.1—it can be seen that the derivatives of Σ^Λ and $\Gamma^{(4)\Lambda}$ contain contributions from the next higher oder vertex $\Gamma^{(4)\Lambda}$ and $\Gamma^{(6)\Lambda}$, respectively. A closer look at Eq. (2.16) shows that this statement holds for all orders of vertex functions—i.e., $\Gamma^{(2m+2)\Lambda}$ contributes to $\frac{d}{d\Lambda}\Gamma^{(2m)\Lambda}$—which results in an infinite flow equation hierarchy.

2.1.3. Truncations of the Flow-Equation Hierarchy

Due to the hierarchical coupling between the different orders of vertex functions, numerical treatments of the lowest order terms demand a truncation at a certain

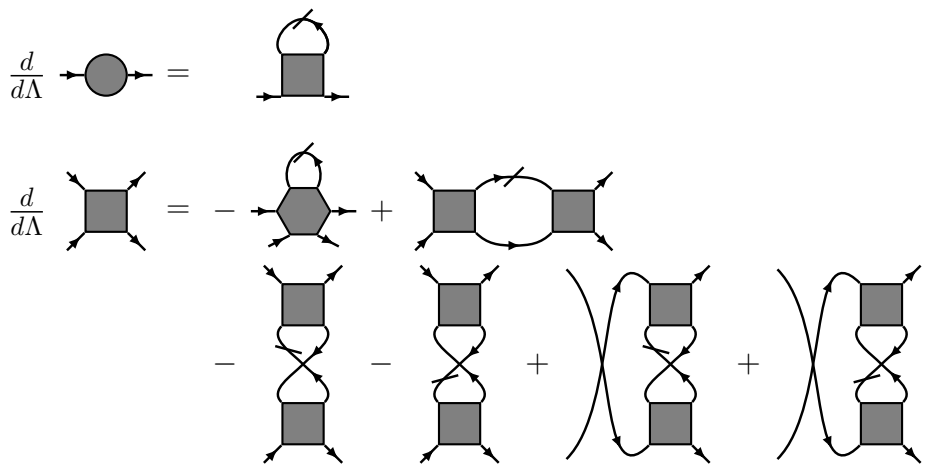

Figure 2.1. The flow equations (2.17) and (2.18) are given in diagrammatic representation. The filled circle denotes the self-energy Σ^Λ, while the filled squares and hexagons represent $\Gamma^{(4)\Lambda}$ and $\Gamma^{(6)\Lambda}$, respectively. Solid lines marked with a dash symbolize single-scale propagators S^Λ, whereas unmarked lines stand for full propagators G^Λ.

order vertex. The level-two truncation—in which $\Gamma^{(6)\Lambda}$ and higher orders are set to zero at all values of Λ—is commonly used in the context of fRG studies for interacting lattice electrons in two dimensions. Within this truncated approach, corrections that enter $\Gamma^{(4)\Lambda}$ via the first term on the right-hand side of Eq. (2.18) are neglected. In Ref. [15] the size of these corrections is discussed in detail. It is found that at high values of Λ—a concrete criterion for Λ being 'large' or 'small' is given in [15]—a small $\Gamma^{(4)\Lambda}$ is needed to ensure that corrections are negligible. Unlike the latter case, at intermediate Λ the corrections are small even when the two-particle vertex is not small, provided that the Fermi surface is smooth and curved. This is based on the fact that momentum space overlaps in internal loop integrations vanish as Λ gets smaller. At low values of the flow parameter, $\Gamma^{(4)\Lambda}$ diverges and its feedback to $\Gamma^{(6)\Lambda}$ outweighs the curvature effects. As in this case the corrections get significantly large, the level-two truncated flow has to be stopped before entering the latter regime.[1] In order to access properties of the symmetry broken phase—such as gap sizes and critical temperatures—from an fRG-flow purely based on fermionic degrees of freedom, the resulting two-particle vertex may be processed further using mean-field theory as described in Ref. [24].

Despite neglecting the three-particle vertex and higher order ones within the level-two truncation, it is possible to include contributions into the flow of $\Gamma^{(4)\Lambda}$ that originate from the fRG equation for $\Gamma^{(6)\Lambda}$. As it is shown by A. A. Katanin in

[1] However, there are fRG setups that allow for continuing the flow into the symmetry broken phase, for instance, see Refs. [22, 23].

Ref. [18], in the level-two truncation the replacement $S^\Lambda \to \frac{d}{d\Lambda} G^\Lambda$ preserves a specific type of diagrams on the right-hand side of Eq. (2.18) that stem from the $\Gamma^{(6)\Lambda}$ contribution in the case of an untruncated flow. A side benefit from this replacement is the following: If one restricts the flow equation for the two-particle vertex to a single channel, it can be solved by the ladder summation in that channel. Such a feature is desirable in order to compare fRG results against standard resummations.

In this work the level-two truncation is used and the self-energy is set to zero during the whole flow. The only object remaining is the two-particle vertex which, however, still contains a lot of interesting physics—like the interplay of fluctuations from particle-particle and particle-hole channels—and which is essential for investigations on low temperature behavior. Even in this simplified scheme, one has to come up with efficient strategies in order to solve the remaining equation for $\Gamma^{(4)\Lambda}$ with high accuracy using a reasonable amount of time and computer resources. Some commonly used strategies are recapitulated in Sec. 2.3, while a newly developed strategy is presented in Ch. 3 as one of the central topics of this thesis.

2.1.4. Cutoff Schemes

The derivation of the flow equations in Subsection 2.1.2 is completely independent of details of how the flow parameter is implemented in the bare propagator G_0^Λ. Besides some fundamental constraints—e.g., the above mentioned conditions $G_0^{\Lambda=\Lambda_0} = 0$, and $G_0^{\Lambda=0} = G_0$ and that a non-zero flow parameter has to regularize infrared divergences to ensure that the flow equation is well defined—there is much freedom in choosing a cutoff scheme. Due to the fact that the level-two truncated flow has to be stopped before entering the strong-coupling regime—as discussed in the last subsection—, different cutoff schemes are not equivalent in practice. Even in an exact flow without approximations, in which the vertex functions at $\Lambda = 0$ would be the same for all valid choices of the cutoff scheme, the results at finite Λ would differ. In a sense, the 'path' that connects the initial and final values $\Gamma^{\Lambda=\Lambda_0}$ and $\Gamma^{\Lambda=0}$ depends on the cutoff scheme. Thus the information contained in the two-particle vertex at a certain Λ is not unique and the cutoff scheme should therefore be suited to the problem under investigation.

A commonly used scheme to regularize G_0 is based on a cutoff function multiplied to the bare propagator, resulting in

$$G_0^\Lambda(k_0, \mathbf{k}) = \theta^\Lambda(k_0, \mathbf{k}) G_0(k_0, \mathbf{k})\,. \tag{2.19}$$

With regard to the regularization of G_0, the cutoff function has to vanish for $k_0 \to 0$, $\xi(\mathbf{k}) \to 0$ at finite Λ and the initial and final conditions translate to $\theta^{\Lambda=\Lambda_0} = 0$ and $\theta^{\Lambda=0} = 1$, respectively. Momentum cutoffs as used in Ref. [16], in

which $\theta^\Lambda(k_0, \mathbf{k}) = \theta^\Lambda(\mathbf{k})$, do not interfere with the frequency space and, therefore, make an analytic treatment of internal frequency summations possible—at least in the case of vertex functions that are independent of internal frequencies. As discussed by C. Honerkamp and M. Salmhofer in Ref. [25], a major drawback of this kind of cutoff is the artificial suppression of instabilities in the particle-hole channel with ordering vector $\mathbf{q} = 0$. This suppression is due to the fact that such a regulator suspends the summation of the corresponding contributions until $\Lambda \lesssim T$. Other instabilities may already occur at higher energies and the level-two truncated flow would need to be stopped before summing the $\mathbf{q} = 0$ contributions in the particle-hole channel. In order to avoid this discrimination of a specific type of instability, a frequency cutoff—e.g., the Ω scheme introduced by C. Husemann and M. Salmhofer in Ref. [3]—can be used. As it regularizes the singularities on the frequency axis, all ordering vectors are treated on equal footing. The cutoff function in the Ω scheme is given by

$$\theta^\Omega(k_0) = \frac{k_0^2}{k_0^2 + \Omega^2}\,, \tag{2.20}$$

in which—following the notation from Ref. [3]—the flow parameter is denoted by Ω in this case. When the frequency dependence of the two-particle vertex is neglected, an analytic treatment of the frequency summation is possible using this regulator. In contrast to a momentum cutoff, which can fulfill the initial condition of the propagator by choosing Λ_0 larger than the bandwidth, $G_0^{\Omega_0} = 0$ cannot be satisfied exactly with a finite Ω_0. For this reason one has to check the results for convergence with increasing initial flow-parameter value. The scale of convergence may also be decreased by using the result of second (or even higher) order perturbation theory as initial interaction instead of the bare one.

There exist other schemes—like the temperature flow introduced in Ref. [25] and the interaction flow as presented in Ref. [26]—that are not based on the original RG idea of successively integrating out degrees of freedom, but that identify parameters of the microscopic system as regulators. In the temperature flow, the fermionic fields undergo a rescaling that shifts the temperature dependence of the action into its quadratic part. The temperature T can then be used as a flow parameter and takes the place of Λ in the above deliberations. In contrast, within the interaction flow scheme a factor g^{-1} is multiplied to the quadratic part of the action and by a rescaling of the fields this prefactor can be transformed into coefficients of the interaction terms. Thus, a flow in the parameter g from 0 to 1 can be seen as a flow from a system containing free particles to the original one containing interacting particles.

Each of the above mentioned regulation schemes has its strengths and weaknesses and there are also many other schemes thinkable. In this work the Ω scheme is used, as it allows for an instability analysis of the normal electronic state towards an ordered state—including those with ordering vectors close to zero in

the particle-hole channel (e.g. ferromagnetic ordering). Since an fRG scheme based on the one presented in Ref. [3] is derived in Ch. 3, a comparison of the results from this work to the previous results given in [3] is appropriate and provided in Ch. 4. In addition to the above argument, using the same cutoff scheme as in the previous study—which is the Ω scheme—is the most convenient choice in terms of a comparison. Following the notation of Ref. [3], the flow parameter is denoted by Ω from now on.

2.2. Symmetry Considerations

In the derivation of the flow equations from the previous section, it was already made use of some symmetry properties. The assumption of $\mathbf{Q}_0^\Omega$, $\mathbf{G}^\Omega$ and $\mathbf{S}^\Omega$ being diagonal implies $U(1)$ invariance—i.e., charge conservation—and restricts the fRG flow to the $U(1)$-symmetric phase. However, as done in the studies [22, 27–30], it is possible to enter the symmetry broken phase by allowing for nonzero off-diagonal terms, which need to be seeded by infinitesimally small values in the initial action.

In addition, demanding spin $SU(2)$ symmetry, the one-particle Green function has to be proportional to the identity matrix in spin space. Even though this simplifying property was already stated in the previous section, Eq. (2.18) is still valid in both $SU(2)$-symmetric and non-$SU(2)$-symmetric cases. In Ref. [23] an fRG study is presented that continues the flow inside the phase of broken $SU(2)$ symmetry by taking into account a spin dependent Green function. In the present study, however, the focus is on instabilities of the symmetric phase that can already be detected at scales sightly above the transition scale by strongly growing susceptibilities. Thus, $SU(2)$-symmetry properties can be exploited—as done in Refs. [15, 16]—, which lead to a reduction of the number of interaction components. More precisely, the tensor

$$\gamma^{(4)\Omega}_{\sigma_1',\sigma_2';\sigma_1,\sigma_2}(k_1',k_2';k_1,k_2) := \Gamma^{(4)\Omega}((k_1',\sigma_1'),(k_2',\sigma_2');(k_1,\sigma_1),(k_2,\sigma_2)) \tag{2.21}$$

is representable in terms of the superposition

$$\begin{aligned}\gamma^{(4)\Omega}_{\sigma_1',\sigma_2';\sigma_1,\sigma_2}(k_1',k_2';k_1,k_2) = &- V^\Omega(k_1',k_2';k_1,k_2)\,\delta_{\sigma_1',\sigma_1}\delta_{\sigma_2',\sigma_2} \\ &+ \tilde{V}^\Omega(k_1',k_2';k_1,k_2)\,\delta_{\sigma_1',\sigma_2}\delta_{\sigma_2',\sigma_1}\,,\end{aligned} \tag{2.22}$$

as these two contributions are the only $SU(2)$ invariant terms. Due to anti-commutation of Grassmann fields, the two exchanges $(k_1',\sigma_1') \leftrightarrow (k_2',\sigma_2')$ and $(k_1,\sigma_1) \leftrightarrow (k_2,\sigma_2)$ are compensated independently by a minus sign, when applied to the two-particle vertex $\gamma^{(4)\Omega}_{\sigma_1',\sigma_2',\sigma_1,\sigma_2}(k_1',k_2';k_1,k_2)$. This yields the relation

$$\begin{aligned}\tilde{V}^\Omega(k_1',k_2';k_1,k_2) &= V^\Omega(k_2',k_1';k_1,k_2) \\ &= V^\Omega(k_1',k_2';k_2,k_1)\,.\end{aligned} \tag{2.23}$$

In this work, lattice systems are studied that exhibit a discrete translational symmetry which leads to a conservation of (lattice) momentum and, in addition, time translation symmetry results in a conservation of Matsubara frequency. These two conservation laws guarantee diagonal Green functions $G^{\Omega}((k,\sigma);(k',\sigma')) = G^{\Omega}(k)\delta_{k,k'}\delta_{\sigma,\sigma'}$ in the case of one band systems. Furthermore, the two-particle coupling simplifies to

$$V^{\Omega}(k_1,k_2;k_1',k_2') = V^{\Omega}(k_1,k_2,k_2')\,\delta_{k_1+k_2,k_1'+k_2'}\,. \tag{2.24}$$

Using Eqs. (2.21), (2.22), (2.23), and (2.24) the flow equation for $\Gamma^{(4)\Omega}$ (cf. Eq. (2.18)) leads to

$$\frac{d}{d\Omega}V^{\Omega}(k_1,k_2,k_3) = \mathcal{T}^{\Omega}_{\text{pp}}(k_1,k_2,k_3) + \mathcal{T}^{\Omega}_{\text{cr-ph}}(k_1,k_2,k_3) + \mathcal{T}^{\Omega}_{\text{d-ph}}(k_1,k_2,k_3)\,, \tag{2.25}$$

in which the contributions on the right-hand side are classified as a *particle-particle* term

$$\begin{aligned}\mathcal{T}^{\Omega}_{\text{pp}}(k_1,k_2,k_3) = -\int dp\,\Big[\partial_{\Omega}G^{\Omega}(p)\,G^{\Omega}(k_1+k_2-p)\Big] \\ \times V^{\Omega}(k_1,k_2,p)\,V^{\Omega}(k_1+k_2-p,p,k_3)\,,\end{aligned} \tag{2.26}$$

a *crossed particle-hole* term

$$\begin{aligned}\mathcal{T}^{\Omega}_{\text{cr-ph}}(k_1,k_2,k_3) = -\int dp\,\Big[\partial_{\Omega}G^{\Omega}(p)\,G^{\Omega}(p+k_3-k_1)\Big] \\ \times V^{\Omega}(k_1,p+k_3-k_1,k_3)\,V^{\Omega}(p,k_2,p+k_3-k_1)\,,\end{aligned} \tag{2.27}$$

and three *direct particle-hole* terms

$$\begin{aligned}\mathcal{T}^{\Omega}_{\text{d-ph}}(k_1,k_2,k_3) = \int dp\,\Big[\partial_{\Omega}G^{\Omega}(p)\,G^{\Omega}(p+k_2-k_3)\Big] \\ \times\Big[2V^{\Omega}(k_1,p+k_2-k_3,p)\,V^{\Omega}(p,k_2,k_3) \\ - V^{\Omega}(k_1,p+k_2-k_3,k_1+k_2-k_3)\,V^{\Omega}(p,k_2,k_3) \\ - V^{\Omega}(k_1,p+k_2-k_3,p)\,V^{\Omega}(p,k_2,p+k_2-k_3)\Big]\,.\end{aligned} \tag{2.28}$$

The above flow equation applies to $U(1)$ and $SU(2)$ invariant systems that exhibit translation invariance in lattice vectors and imaginary time. According to the deliberations from Subsection 2.1.3, Eq. (2.25) corresponds to the level-two truncation and the Katanin replacement is used. A diagrammatic representation of the five contributions from Eqs. (2.26)–(2.28) is given in Fig. 2.2.

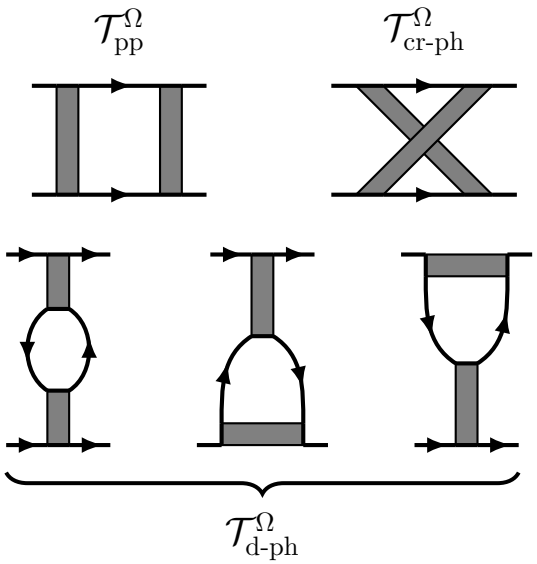

Figure 2.2. In the case of $U(1)$ and $SU(2)$ invariance, the diagrams contributing to the flow of $V^{\Omega}(k_1, k_2, k_3)$ are shown. A gray bar represents the two-particle coupling, while the spin is conserved along the short edge. Closed loops imply a derivative with respect to the scale Ω. The diagrams are classified as particle-particle (pp), crossed particle-hole (cr-ph), and direct particle-hole (d-ph) terms, respectively.

Moreover, the coupling function V^{Ω} itself contains symmetries that may be utilized to reduce the numerical effort of solving Eq. (2.25):

$$\text{Grassmann antisymmetry:} \quad V^{\Omega}(k_1, k_2, k_3) = V^{\Omega}(k_2, k_1, k_1 + k_2 - k_3) \tag{2.29}$$

$$\text{particle-hole symmetry:} \quad V^{\Omega}(k_1, k_2, k_3) = V^{\Omega}(k_1 + k_2 - k_3, k_3, k_2) \tag{2.30}$$

$$\text{point-group symmetries:} \quad V^{\Omega}(k_1, k_2, k_3) = V^{\Omega}(\hat{P}\, k_1, \hat{P}\, k_2, \hat{P}\, k_3) \tag{2.31}$$

While the Grassmann antisymmetry can directly be read off from Eq. (2.23), the particle-hole symmetry reflects the invariance of the action with respect to the transformation $\psi \to i\bar{\psi}$, $\bar{\psi} \to i\psi$. The operator $\hat{P}$ acts on momentum $\hat{P}\, k = (k_0, \hat{P}\, \mathbf{k})$ and has to be chosen from the set of point group operations that correspond to the underlying lattice.

As this work is focused on the momentum dependence of the two-particle coupling, symmetries that do not affect momentum space—like time reversal symmetry—are out of scope. With regard to a more universal perspective, Ref. [31] gives a generalized approach that translates symmetries of a given system into properties of vertex functions, as it is done here exemplary for the above considered symmetries.

2.3. Application Strategies

In applications to two-dimensional systems, the exact solution of the flow equation (2.25)—or rather of Eq. (2.18) in a less symmetric situation—is usually inaccessible. Therefore, numerical treatments become necessary which, in turn, necessitate the reduction of continuous function dependencies to a set of discrete components evaluated at a finite number of sampling points. In this section, three different strategies used in the literature for discretizing the momentum dependencies of V^{Ω} are recapitulated. Especially the first one of these three—often referred to as *Fermi Surface patching*—has been used frequently to study two-dimensional systems in terms of competing electronic ordering tendencies. As frequency dependencies are left unchanged, the corresponding labels are omitted within this section. Furthermore, with regard to a more transparent notation, dependences on the flow parameter are kept implicit. Therefore, the focus is on the object $V(\mathbf{k_1}, \mathbf{k_2}, \mathbf{k_3})$.

2.3.1. Fermi Surface Patching

The Fermi Surface (FS) patching is built upon the argument that the most important coupling terms at low temperatures are those with in- and outgoing momenta originating from the FS. In order to support this argument—at least in cases in which the structure of V is not too dominant—one may focus on loop terms[2] of the form

$$\dot{\chi}_{\mathrm{ph/pp}}(l, \mathbf{p}) = \int dp_0 \left[\partial_{\Omega} G(p)\, G(l \pm p)\right]. \tag{2.32}$$

Assuming a frequency independent coupling in Eqs. (2.26)–(2.28), the V terms can be pulled out of the p_0 integral and Eq. (2.32) contributes as a factor to the integrands of the momentum integrals. At low temperatures and scales Ω this factor evolves a strongly peaked structure with maximum absolute values where both momenta $\mathbf{p}$ and $\mathbf{l} \pm \mathbf{p}$ lie on the FS. This momentum structure of $\dot{\chi}_{\mathrm{ph/pp}}$ causes that the most important contributions to the renormalization of V are kept by concentrating on momenta originating from the FS.

Following the above argumentation, a discretization of the first Brillouin Zone (BZ) into patches can be achieved by choosing sampling points on the FS, while each of these points serves as a representative for the surrounding patch. In order to cover the variation of the two-particle coupling along the FS, the distance between two neighboring sampling points should be small. This means, in turn, that the patches should be narrow in the direction along the FS. However, in the direction perpendicular to the FS the patches are usually elongated. Since internal

[2] Note that the dependence of the fermionic Green functions on the flow parameter is passed on to the loops term, even though it is not made explicit in the current notation.

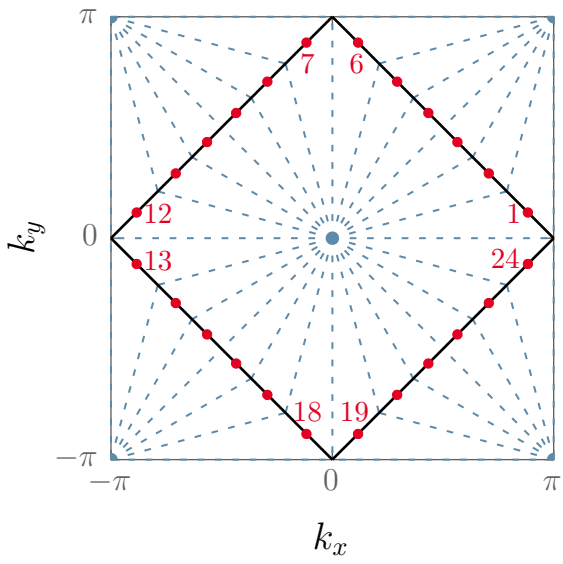

Figure 2.3. The first BZ of the one-band Hubbard model is shown. At half filling the FS takes the form of a square (black solid line). Following the schematic description given in the text, the BZ is divided into 24 patches indicated by blue dashed lines. Each patch contains a representative sampling point lying on the FS (red dots).

momenta need to be integrated over the whole BZ, projections for momenta onto the corresponding FS sampling points are necessary in order to evaluate the coupling function. However, resulting projection errors are usually small as largest contributions stem from momenta very close to the FS. Fig. 2.3 shows the FS of a one-band Hubbard model at half filling and an exemplary decomposition of the first BZ into 24 patches. As already mentioned above, a projection of momenta onto sampling points is a preceding step to the evaluation of the two-particle coupling. Assuming an N-patch discretization each patch can be labeled by an integer $i \in \{1, \ldots, N\}$, while sampling points may be called $\mathbf{k}_i^{\mathrm{SP}}$. Let $\mathbf{k}_1$, $\mathbf{k}_2$, and $\mathbf{k}_3$ be momenta within patches i_1, i_2, and i_3 respectively, then the mapping

$$V(\mathbf{k}_1, \mathbf{k}_2, \mathbf{k}_3) \to V(\mathbf{k}_{i_1}^{\mathrm{SP}}, \mathbf{k}_{i_2}^{\mathrm{SP}}, \mathbf{k}_{i_3}^{\mathrm{SP}}) \tag{2.33}$$

is used to evaluate V for the given momentum combination.

Zanchi and Schulz pioneered in applying the FS patching to the one-band Hubbard model on the square lattice (cf. Refs. [32, 33]) using a field theoretical RG scheme different from the one presented here. 1PI fRG studies followed using a momentum space cutoff (cf. Ref. [16]) and the temperature flow (cf. Refs. [25, 34, 35]) respectively. Furthermore, there are applications of extended patching schemes to this model. These extended schemes also include sampling points in the direction perpendicular to the FS (cf. Ref. [36]).

The same discretization strategy was used to investigate models on the monolayer honeycomb lattice (cf. Refs. [37–40]), as well as on bilayer (cf. Refs. [41–43]), and trilayer (cf. Ref. [44]) honeycomb lattices. As the FS often appears to consist of only two inequivalent points within these models, extended patching schemes were frequently used in order to achieve a sufficiently high resolution. Focusing on the impact of varying point distribution, Refs. [45, 46] indicate that position and number of sampling points are important parameters to the numerical setup in these cases. The authors used points which were placed on several rings with different radii around the two dot-like FSs. It was found that the critical scales as well as—at least to some degree—the kind of leading instability show a dependence on both the number and the radii of those rings.

Another class of systems to which the FS patching was frequently applied, model the iron- pnictide layer of iron-based superconductors. Most commonly, an effective five-band model describing the low-energy physics by focusing on the iron-3d orbitals was used, in which the unit cell was chosen to contain one iron site. In these materials the FS consists of several disjointed parts that form electron and hole pockets respectively, while the number of these pockets depends on both the material type and the doping level. The first patching studies tackled five-pocket models (cf. Refs. [47, 48]) and subsequent investigations compared five- and four-pocket scenarios (cf. Refs. [49–51]). Other works focused on the effect of strong hole doping (cf. Ref. [52]), included the variation of the dispersion in z direction (cf. Ref. [53]), and investigated the possible appearance of a time-reversal symmetry-breaking state (cf. Ref. [54]), respectively. There are also patching studies that did not use the standard five-band model systems. In Ref. [55] the p orbitals of the pnictide atoms are also included in the effective low-energy description leading to an eight-band model. Moreover, the analysis in Ref. [56] is based on a folded BZ that originates from a unit cell containing two iron sites.

2.3.2. Exchange Parametrization

Even though the application of the FS patching to the model systems mentioned above has brought many insights, the scheme has its weaknesses. In particular, an increase of the resolution is limited due to the scaling of the number of coupling components with respect to the number of patches, which obeys a third power behavior. In Ref. [3] C. Husemann and M. Salmhofer develop a scheme that uses a different parametrization of the two-particle coupling V. The leading idea behind rephrasing the 1PI fRG equations is the following: Starting from a regular coupling function, the only momentum dependencies that may develop singularities during the flow are the transfer momenta appearing in the fermionic loops in Eqs. (2.26)–(2.28). Following this idea, the authors of Ref. [3] split up

the coupling V into three parts plus the initial interaction U by writing

$$\begin{aligned} V(\mathbf{k_1},\mathbf{k_2},\mathbf{k_3}) = U(\mathbf{k_1},\mathbf{k_2},\mathbf{k_3}) - \Phi_{\mathrm{SC}}(\mathbf{k_1}+\mathbf{k_2},\mathbf{k_1},\mathbf{k_3}) + \Phi_{\mathrm{M}}(\mathbf{k_3}-\mathbf{k_1},\mathbf{k_1},\mathbf{k_2}) \\ + \frac{1}{2}\Phi_{\mathrm{M}}(\mathbf{k_2}-\mathbf{k_3},\mathbf{k_1},\mathbf{k_2}) - \frac{1}{2}\Phi_{\mathrm{K}}(\mathbf{k_2}-\mathbf{k_3},\mathbf{k_1},\mathbf{k_2}) \end{aligned} \tag{2.34}$$

and they define

$$\dot{\Phi}_{\mathrm{SC}}(\mathbf{k_1}+\mathbf{k_2},\mathbf{k_1},\mathbf{k_3}) = -\mathcal{T}_{\mathrm{pp}}(\mathbf{k_1},\mathbf{k_2},\mathbf{k_3})\,, \tag{2.35}$$

$$\dot{\Phi}_{\mathrm{M}}(\mathbf{k_3}-\mathbf{k_1},\mathbf{k_1},\mathbf{k_2}) = \mathcal{T}_{\text{cr-ph}}(\mathbf{k_1},\mathbf{k_2},\mathbf{k_3})\,, \tag{2.36}$$

$$\dot{\Phi}_{\mathrm{K}}(\mathbf{k_2}-\mathbf{k_3},\mathbf{k_1},\mathbf{k_2}) = -2\,\mathcal{T}_{\text{d-ph}}(\mathbf{k_1},\mathbf{k_2},\mathbf{k_3}) + \mathcal{T}_{\text{cr-ph}}(\mathbf{k_1},\mathbf{k_2},\mathbf{k_1}+\mathbf{k_2}-\mathbf{k_3})\,. \tag{2.37}$$

In the above decomposition, the first argument of each Φ equals one of the loop transfer momenta. Consequently, each Φ captures a specific kind of singular behavior, or, in other words, it represents a certain *channel*. In contrast, the other two momentum dependencies stay regular during the flow and are usually smooth. The rephrased form of the fRG in Eqs. (2.35)–(2.37) is often called *exchange parametrization*, as a further decomposition of the Φs leads to a formulation that is based on propagators that resemble those of exchange bosons. Since a detailed description of this approach is given in Ref. [3] and a similar parametrization is discussed in Ch. 3 of this thesis, there are no further details provided at this point. Generally, it can be stated that in the exchange parametrization the discretization may now be focused on the first argument of the Φs, while the other two arguments can be treated using a much smaller number of sampling points. Thus, the description is based on three objects, while each one mainly depends on one momentum leading to a linear scaling of the number of components with respect to the number of sampling points. This is in contrast to the above stated cubic behavior in the FS patching scheme.

After its development in Ref. [3], in which the scheme was used to investigate the one-band Hubbard model at van Hove filling neglecting the self-energy and frequency dependencies of the two-particle vertex, the exchange parametrization was applied to an extended Hubbard model which includes a nearest neighbor repulsion term (cf. Ref. [57]). Frequency dependencies and self-energy renormalizations were taken into account in Refs. [58, 59]. In the years that followed, the idea of decomposing the two-particle vertex in combination with an exchange parametrization of the constituents was implemented in many different contexts. In terms of 1PI fRG approaches, mention can be made of the elaboration of a scheme that facilitates flows into the phase with broken $SU(2)$ symmetry in Ref. [23] and its application to a two-pocket model in Ref. [60]. As a parallel progress, flows into $U(1)$-symmetry broken states were developed and conducted focusing on both the attractive (cf. Ref. [29]) and the repulsive one-band Hubbard model (cf. Ref. [30]). Other studies based on the exchange parametrization

stayed in the symmetric phase and analyzed, e.g., the three-band Emery model (cf. Ref. [61])—a model for describing the Cu-O plane of the high-T_c cuprate superconductors[3]—and the possibility of coexisting superconductivity and magnetic order in the repulsive one-band Hubbard model (cf. Ref. [62]).

2.3.3. Singular-Mode FRG

As already mentioned in the previous subsection, the exchange parametrization approach has been modified and developed further by different groups. One of these modifications, the so-called *Singular-Mode FRG (SMFRG)*, was presented by W.-S. Wang, Y.-Y. Xiang, Q.-H. Wang, et al. in Ref. [4]. Even though the quantities used in that scheme are parameterized according to Ref. [3] and the contributions from the right-hand side of the flow equation are assigned to different channels, there are also clear differences between the SMFRG and the exchange parametrization scheme presented by C. Husemann and M. Salmhofer in Ref. [3]. Those differences are one reason for a separate discussion of the SMFRG approach in the present thesis. A second reason is that the fRG scheme derived in Ch. 3 is strongly motivated by the one of W.-S. Wang, Y.-Y. Xiang, Q.-H. Wang, et al.. Therefore, the current subsection also serves as a reference which will be used to reveal the similarities and to emphasize the differences between the SMFRG and the method derived in the following chapter. See also Appendix A of Ref. [20] for a comprehensive comparison of both schemes.

In Ref. [4] the authors introduce the SMFRG starting with a definition of three differently projected versions of the coupling function:[4]

$$V(\mathbf{k}+\mathbf{l},-\mathbf{k},-\mathbf{p}) = \sum_{m,n} f_m^*(\mathbf{k})\, V_{m,n}^P(\mathbf{l})\, f_n(\mathbf{p})\,, \tag{2.38}$$

$$V(\mathbf{k}+\mathbf{l},\mathbf{p},\mathbf{k}) = \sum_{m,n} f_m^*(\mathbf{k})\, V_{m,n}^C(\mathbf{l})\, f_n(\mathbf{p})\,, \tag{2.39}$$

$$V(\mathbf{k}+\mathbf{l},\mathbf{p},\mathbf{p}+\mathbf{l}) = \sum_{m,n} f_m^*(\mathbf{k})\, V_{m,n}^D(\mathbf{l})\, f_n(\mathbf{p}). \tag{2.40}$$

The functions $\{f_m\}$—which are called *form factors*—form a set of orthogonal basis functions.[5] Furthermore, projection operators $\hat{P}$, $\hat{C}$, and $\hat{D}$ are defined which invert the above equations individually, i.e., $V_{m,n}^B(\mathbf{l}) = \hat{B}[V]_{m,n}(\mathbf{l})$ for

[3] In this context, it has to be mentioned that the fRG in the level-two truncation is not capable of investigating a cuprate model using realistic coupling strengths. This is due to the fact that the Cu 3*d* orbitals are strongly coupled while the level-two truncation is limited to weak and moderate coupling scenarios.

[4] In order to avoid confusion about the labeling of projected coupling functions, note that the notation used here is slightly different from the one in Ref. [4].

[5] See Sec. 3.2 for a detailed description of a basis suitable for applications to the square lattice.

$B \in \{P, C, D\}$. In the parametrization of Eqs. (2.38)–(2.40) the transfer momenta from Eqs. (2.35)–(2.37) appear again and are labeled by $\mathbf{l}$ in the respective line. Thus, as in the exchange parametrization approach, the description is based on three distinct channels. A projection of V onto one channel followed by an unprojection in the same channel—as defined in Eqs. (2.38)–(2.40)—yields a coupling function $\bar{V}$, which is equal to V in the case that the set of basis functions is complete. However, truncations of the complete set are indispensable in practice, while meaningful truncation schemes can be used to retain the most important features.

Within the SMFRG, the contributions from the right-hand side of the flow equation (cf. Eqs. (2.26)–(2.28) and Fig. 2.2) are approximated using the projected coupling functions. This yields[6]

$$\partial_\Omega V^P_{m,n} = \sum_{m',n'} V^P_{m,m'}\, \dot{\chi}^{\mathrm{pp}}_{m',n'}\, V^P_{n',n}\,, \tag{2.41}$$

$$\partial_\Omega V^C_{m,n} = \sum_{m',n'} V^C_{m,m'}\, \dot{\chi}^{\mathrm{ph}}_{m',n'}\, V^C_{n',n}\,, \tag{2.42}$$

$$\partial_\Omega V^D_{m,n} = \sum_{m',n'} \Big(\big(V^C_{m,m'} - V^D_{m,m'}\big)\, \dot{\chi}^{\mathrm{ph}}_{m',n'}\, V^D_{n',n} + V^D_{m,m'}\, \dot{\chi}^{\mathrm{ph}}_{m',n'}\, \big(V^C_{n',n} - V^D_{n',n}\big) \Big)\,, \tag{2.43}$$

where the symbol ∂_Ω is used for pointing out that each line contains contributions from only one channel. The fermionic loop terms appearing in the above equations are projections of the ones from Eq. (2.32) and are defined by

$$\dot{\chi}^{\mathrm{pp/ph}}_{m,n}(\mathbf{l}) = \int d\mathbf{p}\, f_m(\mathbf{p})\, \dot{\chi}_{\mathrm{pp/ph}}(\mathbf{l}, \mathbf{p})\, f^*_n(\mathbf{p})\,. \tag{2.44}$$

In order to calculate the full derivative of a projected coupling function $V^B_{m,n}(\mathbf{l})$ with respect to Ω, the summation of all contributions from Eqs. (2.41)–(2.43) is preceded by projections[7] onto channel B. Thus, the SMFRG flow equations read

$$\frac{d}{d\Omega} V^P_{m,n} = \quad \partial_\Omega V^P_{m,n} \quad + \hat{P}[\partial_\Omega V^C]_{m,n} + \hat{P}[\partial_\Omega V^D]_{m,n}\,, \tag{2.45}$$

$$\frac{d}{d\Omega} V^C_{m,n} = \hat{C}[\partial_\Omega V^P]_{m,n} + \quad \partial_\Omega V^C_{m,n} \quad + \hat{C}[\partial_\Omega V^D]_{m,n}\,, \tag{2.46}$$

$$\frac{d}{d\Omega} V^D_{m,n} = \hat{D}[\partial_\Omega V^P]_{m,n} + \hat{D}[\partial_\Omega V^C]_{m,n} + \quad \partial_\Omega V^D_{m,n}\,. \tag{2.47}$$

[6] In Eqs. (2.41)–(2.43) the dependence of all objects on the momentum $\mathbf{l}$ is omitted for brevity, i.e., $V^{P/C/D}_{m,n} \equiv V^{P/C/D}_{m,n}(\mathbf{l})$ and $\dot{\chi}^{\mathrm{pp/ph}}_{m,n} \equiv \dot{\chi}^{\mathrm{pp/ph}}_{m,n}(\mathbf{l})$.

[7] In this situation, the notation used is not fully explicit. For instance, a projection of $\partial_\Omega V^C$ on channel P implies an intermediate unprojection as given in Eq. (2.39) before the operator $\hat{P}$ can be applied.

As in the exchange parametrization approach presented in the previous subsection, the SMFRG is based on three flowing objects where each one is parametrized according to one channel. Consequently, the scaling of the number of coupling components with respect to the number of sampling points is equally advantageous. However, two major differences between both schemes can be revealed: Firstly, the momentum integrals that stem from Eqs. (2.26)–(2.28) are decomposed to some extend in the SMFRG while their structure is unchanged in the exchange parametrization approach. Focusing on the integrand in Eq. (2.44), two form factors take the place of the coupling functions, while those are reshaped by a separate projection operation. As the same separation is used in the derivation in Ch. 3, reference to that chapter is made for a discussion of resulting benefits. A second important difference is the type of object used in the flow. While in the exchange parametrization scheme the three Φs add up uniquely to the full two-particle coupling according to Eq. (2.34), the three projected Vs are separate representations of the full coupling in the SMFRG framework. The projected couplings can be seen as filtered forms of the full one, since most information of two channels is filtered out in a projection using a truncated form-factor basis. Consequently, ambiguities are likely when performing subsequent calculations, as the decision on using V^P, V^C, or V^D affects the result.

Since its first application to a model for electron doped graphene in Ref. [4], the SMFRG was used by Q.-H. Wang et al. to study many different model systems. Exemplarily, investigations on the Kagome lattice at van Hove filling (cf. Ref. [63]), on a model for double-layer FeSe (cf. Ref. [64]), and an analysis on doping effects in LaOCrAs (cf. Ref. [65]) are cited here.

Chapter 3.

The Truncated Unity Approach

After the derivation of the level-two truncated flow equations, a strategy for solving these equations on a high-performance computer is presented in this chapter. The new scheme is closely related to two of the approaches discussed in Sec. 2.3, the exchange parametrization and the singular-mode fRG. In order to make the connection clear, reference to that section is made in the appropriate passages. Besides the formal derivation, Sec. 3.1 contains a statement on the computational benefits associated with the new scheme. As the representation of the scheme's central quantities relies on choosing suitable basis functions, Sec. 3.2 presents a way to construct such a basis. In the last section, the program code used to solve the flow equations on a high-performance computer is described briefly, followed by an analysis of the code's scaling behavior with respect to the number of compute cores used.

Large parts of this chapter's content, especially that from Secs. 3.1 and 3.3, have already been published in Ref. [20]. Thus, the following text contains paraphrases of the one from the publication. As it is not always possible to reformulate a statement without changing its connotation, some formulations used here may be close or, in rare cases, even identical to the ones from Ref. [20]. Furthermore, the description of the 2D integration routine PAID given in Sec. 3.3 may contain formulations from Ref. [66], which is a publication of PAID's working principles.

3.1. Flow Equations of the TU Approach

Starting from Eqs. (2.25)–(2.28) the flow equations of the TU scheme are derived in this section. At first a channel-decomposed form of the two-particle coupling is introduced, in which a contribution is classified by the type of diagram it originates from. Using a set of functions that build a basis for the first BZ, the flow equations of the three channels are transformed into new representations. Afterwards, by inserting partitions of unity composed in the new basis, a further modification is performed that completes the derivation. In the last part of this

section, those reshaping steps are recapitulated using a diagrammatic language and benefits of the resulting flow equations are discussed.

3.1.1. Channel Decomposition

Similarly as the exchange parametrization scheme—which is recapitulated briefly in the second part of Sec. 2.3—, the TU approach is based on a decomposition of the two-particle coupling into contributions resulting from three distinct channels and a fourth term containing (a part of) the initial interaction. In the present formulation, the channels are specified by directly following the structure of Eq. (2.25), i.e.,

$$V(k_1,k_2,k_3) = V^{(0)}_{k_1,k_2,k_3} - \Phi^{\mathrm{P}}_{k_1+k_2,\frac{k_1-k_2}{2},\frac{k_4-k_3}{2}} + \Phi^{\mathrm{C}}_{k_1-k_3,\frac{k_1+k_3}{2},\frac{k_2+k_4}{2}} + \Phi^{\mathrm{D}}_{k_3-k_2,\frac{k_1+k_4}{2},\frac{k_2+k_3}{2}} \tag{3.1}$$

with the assignments

$$\dot{\Phi}^{\mathrm{P}}_{k_1+k_2,\frac{k_1-k_2}{2},\frac{k_4-k_3}{2}} = -\mathcal{T}_{\mathrm{pp}}(k_1,k_2,k_3)\,, \tag{3.2}$$

$$\dot{\Phi}^{\mathrm{C}}_{k_1-k_3,\frac{k_1+k_3}{2},\frac{k_2+k_4}{2}} = \mathcal{T}_{\text{cr-ph}}(k_1,k_2,k_3)\,, \tag{3.3}$$

$$\dot{\Phi}^{\mathrm{D}}_{k_3-k_2,\frac{k_1+k_4}{2},\frac{k_2+k_3}{2}} = \mathcal{T}_{\text{d-ph}}(k_1,k_2,k_3)\,. \tag{3.4}$$

While this definition classifies a contribution by its corresponding type of diagram, the three objects used in the exchange parametrization represent the pairing, the magnetic, and the charge channel, respectively. From a technical point of view both choices are rather similar, since both apply the same parametrization strategy in terms of the most important momentum dependencies: As already stated before, a coupling function regular at the initial scale may only develop singularities in the total momentum and transfer momenta appearing in the fermionic loops in Eqs. (2.26)–(2.28). Thus, each of the above defined Φs captures one specific type of singular behavior, just like the objects defined in the second part of Sec. 2.3. In contrast, the other two (weak) momentum dependencies are chosen in a more symmetric fashion in the current parametrization than in the one in Eqs. (2.35)–(2.37). A discussion from a more technical point of view on the parametrization and its implications is given in Appendix A. Due to their connection to one specific channel, the Φs are called *single-channel couplings* in the following. Finally, it is important to note that magnetic and charge channels can be obtained easily from the ones used in the present work. This is achieved by

$$\Phi^{\mathrm{M}}_{k_1-k_3,\frac{k_1+k_3}{2},\frac{k_2+k_4}{2}} = \Phi^{\mathrm{C}}_{k_1-k_3,\frac{k_1+k_3}{2},\frac{k_2+k_4}{2}}\,, \tag{3.5}$$

$$\Phi^{\mathrm{Ch}}_{k_3-k_2,\frac{k_1+k_4}{2},\frac{k_2+k_3}{2}} = -2\,\Phi^{\mathrm{D}}_{k_3-k_2,\frac{k_1+k_4}{2},\frac{k_2+k_3}{2}} + \Phi^{\mathrm{C}}_{k_3-k_2,\frac{k_1+k_4}{2},\frac{k_2+k_3}{2}}\,, \tag{3.6}$$

in which the parametrization introduced in this section was likewise applied to Φ^{M} and Φ^{Ch}.

3.1.2. Exchange Propagators

In the following, the weak momentum dependencies of each single-channel coupling—i.e., the respective second and third dependence—are described through a complete set of form factors $\{f_m(\mathbf{k})\}$, which should be regular and square integrable functions on the first BZ. For this purpose, three operators are defined that project the Φs onto the new basis. Applied to a test function $F(k_1, k_2, k_3)$ these operators read

$$\hat{P}[F]_{m,n}(l) = \int d\mathbf{k}\, d\mathbf{k}'\, f_m^*(\mathbf{k})\, f_n(\mathbf{k}')\, F\left(\frac{l}{2}+k, \frac{l}{2}-k, \frac{l}{2}-k'\right)\Big|_{k_0=k_0'=0}, \tag{3.7}$$

$$\hat{C}[F]_{m,n}(l) = \int d\mathbf{k}\, d\mathbf{k}'\, f_m^*(\mathbf{k})\, f_n(\mathbf{k}')\, F\left(k+\frac{l}{2}, k'-\frac{l}{2}, k-\frac{l}{2}\right)\Big|_{k_0=k_0'=0}, \tag{3.8}$$

$$\hat{D}[F]_{m,n}(l) = \int d\mathbf{k}\, d\mathbf{k}'\, f_m^*(\mathbf{k})\, f_n(\mathbf{k}')\, F\left(k+\frac{l}{2}, k'-\frac{l}{2}, k'+\frac{l}{2}\right)\Big|_{k_0=k_0'=0}. \tag{3.9}$$

By applying each of the above projectors to the respective single-channel coupling function, three objects are defined that depend on two form-factor indices and, in addition, on the total, and transfer momentum of that channel, respectively:

$$P_{m,n}(l) = \hat{P}[\Phi^{\mathrm{P}}]_{m,n}(l) = \int d\mathbf{k}\, d\mathbf{k}'\, f_m^*(\mathbf{k})\, f_n(\mathbf{k}')\, \Phi^{\mathrm{P}}_{l,k,k'}\Big|_{k_0=k_0'=0}, \tag{3.10}$$

$$C_{m,n}(l) = \hat{C}[\Phi^{\mathrm{C}}]_{m,n}(l) = \int d\mathbf{k}\, d\mathbf{k}'\, f_m^*(\mathbf{k})\, f_n(\mathbf{k}')\, \Phi^{\mathrm{C}}_{l,k,k'}\Big|_{k_0=k_0'=0}, \tag{3.11}$$

$$D_{m,n}(l) = \hat{D}[\Phi^{\mathrm{D}}]_{m,n}(l) = \int d\mathbf{k}\, d\mathbf{k}'\, f_m^*(\mathbf{k})\, f_n(\mathbf{k}')\, \Phi^{\mathrm{D}}_{l,k,k'}\Big|_{k_0=k_0'=0}. \tag{3.12}$$

As it is implied by the above expressions, all evaluations of the single-channel coupling functions are done at zero frequencies.[1] The further development towards a scheme that combines the treatment of momenta presented here with an efficient handling of complex frequency dependencies is left for subsequent studies. In Appendix C of Ref. [20], symmetry properties of the objects defined in Eqs. (3.10)–(3.12) are given for the case of form factors that are real-valued in momentum space.

The single-channel coupling functions are (approximately) recovered by the un-

[1] The investigations presented in Chs. 4 and 5 are performed at $T = 0$. Thus, fermionic frequencies can be set to arbitrarily small values. In the case of finite temperatures, however, one would need to work with finite fermionic frequencies, e.g., by using the value at π/β, or $-\pi/\beta$ or the average of both values.

projections

$$\Phi^{\mathrm{P}}_{l,k,k'} \approx \sum_{m,n} f_m(\mathbf{k})\, f^*_n(\mathbf{k}')\, P_{m,n}(l)\,, \tag{3.13}$$

$$\Phi^{\mathrm{C}}_{l,k,k'} \approx \sum_{m,n} f_m(\mathbf{k})\, f^*_n(\mathbf{k}')\, C_{m,n}(l)\,, \tag{3.14}$$

$$\Phi^{\mathrm{D}}_{l,k,k'} \approx \sum_{m,n} f_m(\mathbf{k})\, f^*_n(\mathbf{k}')\, D_{m,n}(l)\,. \tag{3.15}$$

In contrast to the dependence on frequencies, the momentum dependences are reproduced exactly—at least on a formal level using a complete set of basis functions. The flow equations for P, C, and D are obtained by an application of the operators (3.7)–(3.9) to Eqs. (3.2)–(3.4), which yields

$$\dot{P}_{m,n}(l) = -\hat{P}[\mathcal{T}_{\mathrm{pp}}]_{m,n}(l)\,, \tag{3.16}$$

$$\dot{C}_{m,n}(l) = \hat{C}[\mathcal{T}^{\mathrm{cr}}_{\mathrm{ph}}]_{m,n}(l)\,, \tag{3.17}$$

$$\dot{D}_{m,n}(l) = \hat{D}[\mathcal{T}^{\mathrm{d}}_{\mathrm{ph}}]_{m,n}(l)\,. \tag{3.18}$$

As it is known from previous studies (e.g., Ref. [61]), the single-channel couplings are usually slowly varying functions of their second and third momentum dependence. With regard to the projected objects, this statement means that a restriction of the form-factors basis to this kind of functions results in a reasonable approximation. In practice, a numerical solution of the flow equations (3.16)–(3.18) is only possible using a finite basis. Thus, a meaningful truncation of the (complete) basis—as the one suggested here—is a requirement for computational approaches.

Formally, the action of an interacting Fermi system can be rewritten in terms of exchange bosons, leading to a description in which the projected objects play the role of bosonic propagators. In that kind of theory, the projections of Φ^{P}, Φ^{M}, and Φ^{Ch} resemble the propagators of the bosonic fields that couple to fermion pair, spin, and charge bilinears, respectively. The corresponding form factors then characterize the momentum structure of those bilinears. Due to this connection, the projected objects P, C, and D are called *exchange propagators* in the following.[2]

3.1.3. Insertion of Truncated Partitions of Unity

The flow equations derived up to this point—or Eqs.(3.2)–(3.4), as a matter of taste—are basically the ones used in the exchange-parametrization fRG. In a next

[2] Even though D is not directly related to one of the stated physically interpretable bilinears, the term *exchange propagator* is used for this object as well.

step, these equations are modified by inserting partitions of unity in the form-factor basis. Using the completeness relation, the unity can be expanded to

$$1 = \int d\mathbf{p}'\, \delta(\mathbf{p}-\mathbf{p}') = \int d\mathbf{p}' \sum_m f_m(\mathbf{p})\, f_m^*(\mathbf{p}')\,, \tag{3.19}$$

which is inserted on both sides of the fermionic loops in Eqs. (3.16)–(3.18). After that the terms on the right-hand side are rearranged, resulting in

$$\dot{\mathbf{P}}(l) = \quad \mathbf{V}^{\mathrm{P}}(l)\, \dot{\boldsymbol{\chi}}^{\mathrm{pp}}(l)\, \mathbf{V}^{\mathrm{P}}(l)\,, \tag{3.20}$$

$$\dot{\mathbf{C}}(l) = -\mathbf{V}^{\mathrm{C}}(l)\, \dot{\boldsymbol{\chi}}^{\mathrm{ph}}(l)\, \mathbf{V}^{\mathrm{C}}(l)\,, \tag{3.21}$$

$$\dot{\mathbf{D}}(l) = 2\mathbf{V}^{\mathrm{D}}(l)\, \dot{\boldsymbol{\chi}}^{\mathrm{ph}}(l)\, \mathbf{V}^{\mathrm{D}}(l) - \mathbf{V}^{\mathrm{C}}(l)\, \dot{\boldsymbol{\chi}}^{\mathrm{ph}}(l)\, \mathbf{V}^{\mathrm{D}}(l) - \mathbf{V}^{\mathrm{D}}(l)\, \dot{\boldsymbol{\chi}}^{\mathrm{ph}}(l)\, \mathbf{V}^{\mathrm{C}}(l)\,, \tag{3.22}$$

with

$$\chi^{\mathrm{pp}}_{m,n}(l) = \int dp\; G\left(\frac{l}{2}+p\right)\, G\left(\frac{l}{2}-p\right)\, f_m^*(\mathbf{p})\, f_n(\mathbf{p})\,, \tag{3.23}$$

$$\chi^{\mathrm{ph}}_{m,n}(l) = \int dp\; G\left(p+\frac{l}{2}\right)\, G\left(p-\frac{l}{2}\right)\, f_m^*(\mathbf{p})\, f_n(\mathbf{p}) \tag{3.24}$$

and

$$\mathbf{V}^{\mathrm{P}}(l) = \hat{\mathbf{P}}[V^{(0)}](l) - \mathbf{P}(l) \qquad + \hat{\mathbf{P}}[\Phi^{\mathrm{C}}](l) + \hat{\mathbf{P}}[\Phi^{\mathrm{D}}](l)\,, \tag{3.25}$$

$$\mathbf{V}^{\mathrm{C}}(l) = \hat{\mathbf{C}}[V^{(0)}](l) - \hat{\mathbf{C}}[\Phi^{\mathrm{P}}](l) + \mathbf{C}(l) \qquad + \hat{\mathbf{C}}[\Phi^{\mathrm{D}}](l)\,, \tag{3.26}$$

$$\mathbf{V}^{\mathrm{D}}(l) = \hat{\mathbf{D}}[V^{(0)}](l) - \hat{\mathbf{D}}[\Phi^{\mathrm{P}}](l) + \hat{\mathbf{D}}[\Phi^{\mathrm{C}}](l) + \mathbf{D}(l)\,. \tag{3.27}$$

Here, $\chi^{\mathrm{pp}}_{m,n}$, and $\chi^{\mathrm{ph}}_{m,n}$ are convolutions of two-fermion loops with two form factors and the expressions for the projected couplings $\mathbf{V}^{\mathrm{P}}$, $\mathbf{V}^{\mathrm{C}}$, and, $\mathbf{V}^{\mathrm{D}}$ result from applying the projection operators (3.7)–(3.9) to the decomposed two-particle coupling. Furthermore, a new notation is introduced in Eqs. (3.20)–(3.22), and (3.25)–(3.27) in which the objects indexed by two form-factor labels are understood as matrices. For these objects bold symbols are used, while two adjoining matrices imply a usual matrix-matrix multiplication. Via Eqs. (3.13)–(3.15) the exchange propagators are fed back into the projected two-particle couplings, yielding closed flow equations given in (3.20)–(3.22). Since the form-factor basis is truncated in practice, the partition of unity used for the derivation above is truncated as well. Due to this fact, the scheme based on the resulting flow equations is called *truncated-unity (TU) approach*, or *TUfRG*.

In order to provide a more concrete expression for the terms on the right-hand sides of Eqs. (3.25)–(3.27), as an example, the third contribution to $V^{\mathrm{P}}_{m,n}(l)$ is

written out in full:[3]

$$\hat{P}[\Phi^{\mathrm{C}}]_{m,n}(l) \approx \int d\mathbf{k}\, d\mathbf{k}'\; f_m^*(\mathbf{k})\; f_n(\mathbf{k}') \times \sum_{m',n'} f_{m'}\left(\frac{\mathbf{l}+\mathbf{k}-\mathbf{k}'}{2}\right)\; f_{n'}^*\left(\frac{\mathbf{l}-\mathbf{k}+\mathbf{k}'}{2}\right)\; C_{m',n'}(k'+k)\Big|_{k_0=k_0'=0} \tag{3.28}$$

$$= \sum_{\mathbf{R_1},\mathbf{R_2},\mathbf{R_3}} \sum_{m',n'} f_m^*\left(\frac{\mathbf{R_1}}{2}+\frac{\mathbf{R_2}}{2}+\mathbf{R_3}\right)\; f_n\left(\frac{\mathbf{R_1}}{2}+\frac{\mathbf{R_2}}{2}-\mathbf{R_3}\right) \times f_{m'}(\mathbf{R_1})\; f_{n'}^*(\mathbf{R_2})\; C_{m',n'}(k_0=0,\mathbf{R_3})\; e^{-i\frac{1}{2}\mathbf{l}\cdot(\mathbf{R_1}-\mathbf{R_2})} \tag{3.29}$$

So as to avoid a four-dimensional integral, the representation in position space was used in the computations. Since the summation over $\mathbf{R_1}$, $\mathbf{R_2}$, and $\mathbf{R_3}$ contains some subtleties, details on the implementation of this part are provided in Appendix B.

In summary, the following steps of computation have to be performed in order to evaluate the right-hand sides of the flow equations, i.e., to calculate the derivatives of the exchange propagators with respect to the fRG scale:

(i) In order to obtain $\mathbf{V}^{\mathrm{P}}(l)$, $\mathbf{V}^{\mathrm{C}}(l)$, and $\mathbf{V}^{\mathrm{D}}(l)$, project the exchange propagators and the initial term $V^{(0)}$ to all channels and sum up the contributions in accordance with Eqs. (3.25)–(3.27).

(ii) Compute the integrals from Eqs. (3.23) and (3.24) in the differentiated form (w.r.t. Ω) to obtain the convolved two-fermion loops $\dot{\boldsymbol{\chi}}^{\mathrm{pp}}(l)$, and $\dot{\boldsymbol{\chi}}^{\mathrm{ph}}(l)$.

(iii) So as to evaluate $\dot{\mathbf{P}}(l)$, $\dot{\mathbf{C}}(l)$, and $\dot{\mathbf{D}}(l)$, perform the matrix multiplications in the form-factor basis as stated in Eqs. (3.20)–(3.22).

With regard to an implementation of the TUfRG flow, one has to choose, firstly, a set of form factors and, secondly, a grid of sampling points concerning the momentum dependences of the exchange propagators. The former should be chosen in a way that all important slowly varying functions are included in the basis. In view of 2D lattice systems, an approach for building up such a basis in a structured way is presented in Sec. 3.2. In contrast, the grid of sampling points has to be tailored separately to each system under investigation. Here it is important to have a dense grid in the vicinity of momenta, where a peaked structure evolves during the flow. As this requires some knowledge on the system

[3] The other contributions composing the projected two-particle couplings are given in explicit form in Appendix B.

in advance, a preceding analysis using a homogeneous grid may be advisable in the case of a completely unexplored system. This would allow for detecting potentially interesting structures and to set up a tailored grid for a more accurate study.

In a comparison of the TU approach with the SMFRG (cf. third part of Sec. 2.3 and Ref. [4]) one finds that the computational steps in both schemes are very similar. The matrix multiplications in Eqs. (3.20)–(3.22) are like the ones in Eqs. (2.41)–(2.43), there are comparable integration tasks in Eqs. (3.23)–(3.24) and Eq. (2.44), and projection operations—as defined in Eqs. (3.25)–(3.27) and Eqs. (2.45)–(2.47)—are also necessary in both schemes. The main difference between the two approaches is—besides some minor differences, e.g., coefficients $\frac{1}{2}$ in the parametrization—the choice of the central flow objects. In the TUfRG framework the exchange propagators are permanently stored during the flow, while three differently projected versions of the two-particle coupling, i.e., $\mathbf{V}^{\mathrm{P}}(l)$, $\mathbf{V}^{\mathrm{C}}(l)$, and $\mathbf{V}^{\mathrm{D}}(l)$, play this role within the SMFRG. Eqs. (3.25)–(3.27) allow for a direct calculation of the projected couplings from the exchange propagators in the TU approach. Conversely, an inversion of those equations is necessary to obtain the exchange propagators in the SMFRG scheme. This task can be mapped to an inversion of a huge matrix[4], which is computationally a very expensive problem. As a consequence of using the respective central objects, different ways of recovering the full coupling function, which is needed, e.g., for self-energy calculations, are not likewise feasible in both schemes. One way to obtain V is to calculate the single-channel couplings from the exchange propagators via Eqs. (3.13)–(3.15) and to use their relation to V given in Eq. (3.1) afterwards. Since this strategy treats all three channels on equal footing, it preserves sharp structures in all transfer and total momenta. A second way to extract an expression for V is to directly use the information contained in one of the projected two-particle couplings. This can be achieved by an unprojection analogous to Eqs. (3.13)–(3.15) in the appropriate channel. By using this strategy, only one of the (possibly singular) dependencies on total and transfer momenta can be preserved, while the choice of the projection type decides on the type of momentum structure remaining. As the second way causes ambiguities and may also—depending on the context in which V is used—lead to a loss of information, the first way is preferable. However, due to the inversion problem stated above, the first procedure is unsuitable in the SMFRG. In consideration of the fact that the computational steps are basically the same in both approaches, the above comparison of the central objects shows that the TU approach benefits from its exchange-propagator based framework.

[4] In the most accurate calculations shown in Ch. 4, the matrix would have a dimension of about 10^7.

3.1.4. Benefits of the TU Approach

In order to underline the structural changes entering the flow equations when the truncated partitions of unity are inserted, the above derivation is now recapitulated using a diagrammatic language. In this representation each contribution to the right-hand side of the flow equation for the single-channel coupling Φ^{B_1}, with $\mathrm{B}_1 \in \{\mathrm{P}, \mathrm{C}, \mathrm{D}\}$, can be classified as one of the following diagram types:

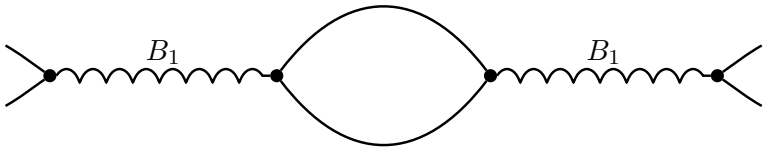

(3.30)

propagator-renormalization diagram

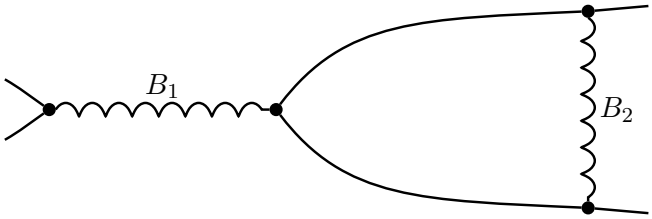

(3.31)

vertex-correction diagram

(3.32)

box diagram

The solid lines correspond to fermionic propagators while a closed loop implies an integration over frequency and momentum. Symbols of the form

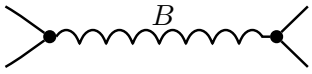

(3.33)

represent single-channel coupling functions. Whereas the couplings labeled by B_1 are the same as the one on the left-hand side of the respective flow equation, the label B_2 denotes a coupling from a different channel. The wiggly lines can be understood as 'propagation direction' of the first (strong) momentum in the respective channel. Since all B_1 couplings are parametrized equally, their propagation direction is the same. In contrast, the B_2 couplings exhibit different parametrizations leading to different propagation directions. As a consequence, those lines appear as part of the closed loops. In an implementation of

the exchange-parametrization fRG, the wiggly lines that appear inside the loops pose a numerical challenge. Since the single-channel couplings may be sharply peaked as function of their first momentum dependence, those objects can enhance the computational cost of the loop integrals significantly. By the insertion of truncated partitions of unity these numerical challenges are softened and the loop integrations become an easier task.

Focusing on the vertex-correction diagram the modifications leading to the TU approach are applied in the following. In a first step the projection operator is applied to Diagram (3.31), yielding

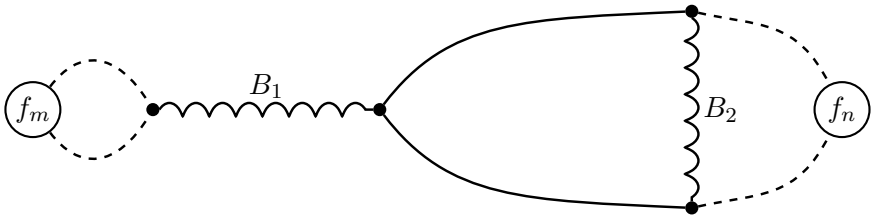

(3.34)

which represents a class of contributions appearing in Eqs. (3.16)–(3.18). In this diagrammatics, a projection integral of the form

$$\int d\mathbf{k}\, f_m^*(\mathbf{k})\, F(\mathbf{k_1}, \mathbf{k_2}, \mathbf{k_3}, \mathbf{k_4}) \tag{3.35}$$

applied to a test function $F(\mathbf{k_1}, \mathbf{k_2}, \mathbf{k_3}, \mathbf{k_4})$[5] is represented by

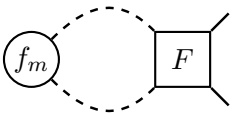

. (3.36)

Consequently, the exchange propagators from Eqs. (3.10)–(3.12) are given by the diagram

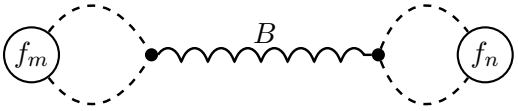

(3.37)

which can be abbreviated by

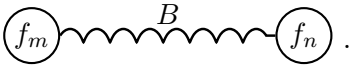

. (3.38)

The label B again serves as a placeholder for the respective channel, i.e., for either P, C, or D. As a next step the truncated partitions of unity are inserted on both

[5] Within this notation $\mathbf{k_1}$ and $\mathbf{k_2}$ label the upper left and lower left leg of the F vertex in Diagram (3.36), respectively. These momenta are superpositions of the integration variable $\mathbf{k}$ and another momentum, e.g., $\mathbf{l}$. $\mathbf{k_3}$ and $\mathbf{k_4}$ label the lower right and upper right leg of F, respectively, while both are independent of $\mathbf{k}$.

sides of the fermionic propagators separating these from the wiggly lines. After that the vertex-correction diagram takes the following form:

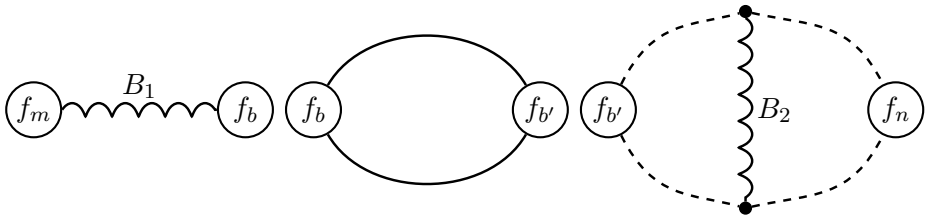

(3.39)

In the above diagram a summation over the form-factor indices b and b' is implied, which is the matrix multiplication denoted by Step (iii) in the summary of the formal derivation. The middle part of Diagram (3.39) is a convolved two-fermion loop (cf. Step (ii)) and the part on the right is a projection of a single-channel coupling on a different channel (cf. Step (i)). Formally, the TU approach is the same as the standard exchange-parametrization method with an additional approximation, that is an insertion of truncated partitions of unity in the form-factor basis. Despite this fact, in a comparison to previous exchange-parametrization implementations (e.g., Ref. [3]) the TUfRG would contain the same contributions plus additional terms, provided that a suitable form-factor basis is used.[6]

With regard to evaluating the right-hand side of the flow equations the unity insertion generates a computational advantage, which is due to the decomposition of the loop integrals. As illustrated by Diagram (3.39), the unity insertion separates the exchange propagators from the fermionic ones at the cost of introducing the projection step (i). Therefore, the loop integrands consist of two fermionic propagators accompanied by two form factors instead of two single-channel couplings. In contrast to the slowly varying form factors the coupling functions may contain strongly peaked structures. Since integrations over regions exhibiting sharp features are numerically expensive, the replacement by smooth functions makes the loop integrals an easier task.

The additional projection task shown in Eq. (3.28)—as well as the ones given in Appendix B—requires the solution of two nested momentum integrals that involve a product of four form factors and one exchange propagator. If the form factors correspond to fixed bond lengths (see Sec. 3.2), the calculation can be performed most efficiently in the real-space representation from Eq. (3.29) (cf. Ref. [4]). This is due to the fact that in this case the form factors are superpositions of Kronecker deltas, which limit the appearing sums to an upper bond length[7]. The implementation of the projection step then consists of two main constituents: A first part that evaluates overlaps of Kronecker deltas to find all index combinations resulting in non-zero contributions and a second part performing Fourier transforms of exchange propagators at all index combinations that have been detected in the

[6] See Appendix B of Ref. [20] for a detailed argumentation.

[7] Obviously, this upper summation bound is directly related to the truncation length of the form-factor basis.

first part. With regard to computational efficiency, one may utilize the fact that the exchange propagator is the only object depending on the scale parameter. Consequently, after the first iteration of the differential equation, a big part of the computation (e.g., the evaluation of Kronecker delta overlaps) can be reused during the rest of the flow. In cases in which a straight-forward implementation of the projection consumes a significant proportion of the total computation time[8], the strategy of reusing computed data can lead to huge savings of computer resources. Exemplary speedups from calculations on the honeycomb lattice are given at the end of Sec. 2 of Ref. [20]. Since the exact speedups depend on details of the implementation, general statements on maximal speedups are difficult. However, in the studies on the square lattice presented in this work, it was possible to reduce the amount of computation time needed by the projections to a few percent of the time needed by the loop integrations.[9] In Appendix B a possible implementation strategy for the projection part is presented.

3.2. Form-Factor Basis

In order to solve the TU flow equations (3.20)–(3.22) using a numerical treatment, a truncation of the previously introduced form-factor basis is necessary. The question arises how the truncation should be implemented, i.e., which functions should be kept, to retain important contributions. To address this topic, reasons for using a truncation length in real space are given in the present section's first part. Moreover, as the systems investigated in Chs. 4 and 5 are invariant with respect to C_{4v} point-group operations, form factors that transform according to the irreducible representations of that group are derived in a second part. This is done by following the procedure described in the third appendix of the review by C. Platt et al. (Ref. [13]), in which the authors focus on calculating basis functions to characterize order-parameter fields on different lattice geometries.

3.2.1. Truncation Scheme

As already mentioned in the previous section, a restriction of the form-factor basis to slowly varying functions on the first BZ is a reasonable truncation scheme. This is due to the experience gained from previous investigations on ground state properties (e.g., Ref. [61]) showing that the leading parts of the single-channel

[8] Depending on the system under investigation, the part that consumes most of the computation time is usually either the loop integration or the projection part.

[9] In the implementation used for the present work, the strategy of reusing data from previous calculation steps was not applied. The speedup compared to a previous implementation was gained solely from restructuring the summations. Thus an additional reduction of the computation time by reusing data would be possible.

two-particle couplings are well described by this type of function. For instance, in a system that exhibits a commensurate anti-ferromagnetic ground state, the leading contributions to Φ^{C} are constant in $\frac{k_1+k_3}{2}$ and $\frac{k_2+k_4}{2}$. To name another example, in the presence of a tendency towards d-wave superconductivity, the functional form of Φ^{P} with respect to $\frac{k_1-k_2}{2}$ and $\frac{k_4-k_3}{2}$ is given by

$$f_{1d_{x^2-y^2}}(\mathbf{k}) \propto \cos(k_x) - \cos(k_y)\,. \tag{3.40}$$

Performing a transformation to real-space representation, slowly-varying functions translate to short-range ones. In concrete terms, the functional form in the first example corresponds to an on-site term $f_{0s}(\mathbf{R}) \propto \delta_{\mathbf{R},(0,0)}$ and in the second example it follows the nearest-neighbor superposition $f_{1d_{x^2-y^2}}(\mathbf{R}) \propto \delta_{\mathbf{R},(1,0)} - \delta_{\mathbf{R},(0,1)} + \delta_{\mathbf{R},(-1,0)} - \delta_{\mathbf{R},(0,-1)}$.[10] Consequently, the above proposed restriction to slowly-varying functions in momentum space can be implemented by a truncation at a certain length in real space. In such a setup, functions that contain contributions from distances beyond the truncation length are not considered.

The bonds[11] that are shorter than the truncation length span a vector space of finite dimension. From a technical perspective, the bonds themselves could directly be used as form factors leading to a 'bond-based' representation. However, from a physical point of view, it is advisable to choose basis functions that transform according to the irreducible representations (IRs) of the system's point group. Such an 'IR-based' choice simplifies the determination of relevant order parameters from the fRG flow. This basis can be obtained by defining subspaces, whereby each subspace is spanned by all bonds having a certain length. Using the procedure suggested in Appendix 3 from Ref. [13], basis functions transforming as IRs of the point group can be constructed for each subspace separately. The union of basis functions from all subspaces then results in the intended basis set.

In view of a system in which the relevant order parameters are already known, it could be reasonable to reduce the number of functions contained in the basis. For instance, in Ref. [3] an investigation on the Hubbard model on the square lattice is presented using a representation based on the form factors f_{0s} and $f_{1d_{x^2-y^2}}$ only. Since the present work's focus is on refining the quantitative accuracy of the method allowing for highly resolved computations, the whole spectrum of basis functions is used for all bond lengths below the truncation bound.

Furthermore, in some cases it might be valuable to choose two separate truncation lengths: a first one used for the projections of single-channel couplings onto exchange propagators and a second one truncating the partition of unity. By using a larger value for the second length it would then be possible to reduce

[10] The second example corresponds to a square-lattice system.
[11] In this context, the term 'bond' denotes a vector from the direct lattice.

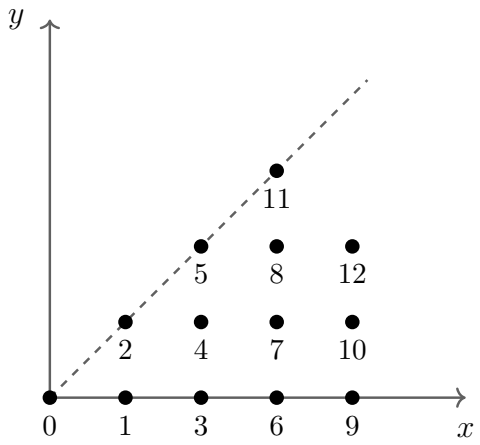

Figure 3.1. With regard to the lattice point located at the origin of the coordinate system, the first twelve nearest-neighbor lattice points are labeled by the respective neighboring degree. As the other parts of the lattice are obtained by performing symmetry operations, only one irreducible segment of the square lattice is displayed here. The dashed line denotes the angle bisector, which is an intersection line of a C_{4v} mirror plane.

the amount of information loss caused by the insertion of truncated unities. Following the argumentation given in Appendix B of Ref. [20], the unity insertion would even be an exact transformation, when the second truncation length was set to a value at least three times as long as the first one. However, an increasing number of contributions to the partition of unity directly increases the number of loop integrals. As the integration task is computationally the most expensive part regarding the models investigated here, the truncation length for the unity partition was not extended in this work. In all computations presented here, both truncation parameters were chosen to the same value.

3.2.2. C_{4v} Point Group

In the following, a form-factor basis suited to C_{4v}-symmetric square-lattice systems is constructed by applying the procedure described above. As a first step, the bonds contained in one irreducible segment of the lattice are labeled by their neighboring degree relative to the lattice site located at the origin, i.e., the ith nearest-neighbor bond is labeled by i. Fig. 3.1 shows this labeling up to the twelfth nearest neighbor. All other lattice sites that are not contained in the considered segment can be obtained by applying symmetry operations to the bonds within the segment. Since the bond length is not affected by these operations, the sites forming one of the subspaces introduced above are reached by applying all symmetry operations to one of the labeled bonds. Each subspace may now carry the same label as the corresponding bond in the irreducible segment.

$\boldsymbol{C_{4v}}$		E	C_2	$2C_4$	$2\sigma_v$	$2\sigma_d$
A_1	(s)	1	1	1	1	1
A_2	(g)	1	1	1	-1	-1
B_1	$(d_{x^2-y^2})$	1	1	-1	1	-1
B_2	(d_{xy})	1	1	-1	-1	1
E_1	(p)	2	-2	0	0	0

Table 3.1. The character table of the C_{4v} point group is shown. Rows denote different irreducible group representations and columns correspond to classes of group elements. In addition to the labels of the irreducible representations, information on the respective symmetries is included in the first column.

The construction of the form-factor basis for each subspace is now done following the description in Appendix 3 of Ref. [13]: Let g be a point-group operation, i.e., an element of $\{E, C_2, C_4, C_4^{-1}, \sigma_{v,1}, \sigma_{v,2}, \sigma_{d,1}, \sigma_{d,2}\}$. Here, E is the identity operation, C_2 (C_4) is a rotation by π ($\pi/2$), and $\sigma_{v/d,1/2}$ are the four possible reflections. The operator

$$\mathcal{P}(\Gamma_j) = \sum_g \chi_j^*(g)\, g \tag{3.41}$$

is then used to construct a function that transforms according to the IR Γ_j. Regarding the C_{4v} point group, these representations as well as the corresponding characters $\chi_j(g)$ are given in the character table 3.1. The application of the operators (3.41), for all j, to a bond from one subspace leads to a set of basis functions for that space. Note that if only one bond is used, the set is not complete. Especially the operator corresponding to the representation E_1 has to be applied to different bonds until a complete basis of linear independent functions is found.

The subspace corresponding to zero bond length is spanned by the on-site bond only. By applying the operators $\mathcal{P}(\Gamma_j)$ to this bond, only $\Gamma_j = A_1$ results in a non-zero projection. After a normalization, the resulting form factor in real space reads

$$f_{0s}(\mathbf{R}) = \delta_{\mathbf{R},0}\,, \tag{3.42}$$

which is, of course, the on-site bond itself. In this notation, the subscript denotes the neighboring degree $i(=0)$ and the symmetry (s). A transformation to momentum representation results in the constant function

$$f_{0s}(\mathbf{k}) = 1\,. \tag{3.43}$$

As the subspace labeled by $i = 1$ is four dimensional, four form factors are required to accomplish a complete basis. In this case, projections according to A_2 and B_2

vanish. A set of normalized basis functions is given by

$$f_{1s}(\mathbf{R}) = \frac{1}{2}\left(\delta_{\mathbf{R},\mathbf{x}} + \delta_{\mathbf{R},-\mathbf{x}} + \delta_{\mathbf{R},\mathbf{y}} + \delta_{\mathbf{R},-\mathbf{y}}\right), \tag{3.44}$$

$$f_{1d_{x^2-y^2}}(\mathbf{R}) = \frac{1}{2}\left(\delta_{\mathbf{R},\mathbf{x}} + \delta_{\mathbf{R},-\mathbf{x}} - \delta_{\mathbf{R},\mathbf{y}} - \delta_{\mathbf{R},-\mathbf{y}}\right), \tag{3.45}$$

$$f_{1p_x}(\mathbf{R}) = \frac{i}{\sqrt{2}}\left(\delta_{\mathbf{R},\mathbf{x}} - \delta_{\mathbf{R},-\mathbf{x}}\right), \tag{3.46}$$

$$f_{1p_y}(\mathbf{R}) = \frac{i}{\sqrt{2}}\left(\delta_{\mathbf{R},\mathbf{y}} - \delta_{\mathbf{R},-\mathbf{y}}\right) \tag{3.47}$$

in real-space, with $\mathbf{x} = (1, 0)$ and $\mathbf{y} = (0, 1)$ being the basis vectors of the lattice, and by

$$f_{1s}(\mathbf{k}) = \cos(k_x) + \cos(k_y), \tag{3.48}$$

$$f_{1d_{x^2-y^2}}(\mathbf{k}) = \cos(k_x) - \cos(k_y), \tag{3.49}$$

$$f_{1p_x}(\mathbf{k}) = \sqrt{2}\,\sin(k_x), \tag{3.50}$$

$$f_{1p_y}(\mathbf{k}) = \sqrt{2}\,\sin(k_y) \tag{3.51}$$

in momentum-space representation. Next, in the $i = 2$ subspace the projections to A_2 and B_1 vanish. The other IRs yield

$$f_{2s}(\mathbf{R}) = \frac{1}{2}\left(\delta_{\mathbf{R},\mathbf{x}+\mathbf{y}} + \delta_{\mathbf{R},-\mathbf{x}-\mathbf{y}} + \delta_{\mathbf{R},-\mathbf{x}+\mathbf{y}} + \delta_{\mathbf{R},\mathbf{x}-\mathbf{y}}\right), \tag{3.52}$$

$$f_{2d_{xy}}(\mathbf{R}) = \frac{1}{2}\left(\delta_{\mathbf{R},\mathbf{x}+\mathbf{y}} + \delta_{\mathbf{R},-\mathbf{x}-\mathbf{y}} - \delta_{\mathbf{R},-\mathbf{x}+\mathbf{y}} - \delta_{\mathbf{R},\mathbf{x}-\mathbf{y}}\right), \tag{3.53}$$

$$f_{2p_{x+y}}(\mathbf{R}) = \frac{i}{\sqrt{2}}\left(\delta_{\mathbf{R},\mathbf{x}+\mathbf{y}} - \delta_{\mathbf{R},-\mathbf{x}-\mathbf{y}}\right), \tag{3.54}$$

$$f_{2p_{x-y}}(\mathbf{R}) = \frac{i}{\sqrt{2}}\left(\delta_{\mathbf{R},\mathbf{x}-\mathbf{y}} - \delta_{\mathbf{R},-\mathbf{x}+\mathbf{y}}\right) \tag{3.55}$$

and

$$f_{2s}(\mathbf{k}) = \cos(k_x + k_y) + \cos(k_x - k_y), \tag{3.56}$$

$$f_{2d_{xy}}(\mathbf{k}) = \cos(k_x + k_y) - \cos(k_x - k_y), \tag{3.57}$$

$$f_{2p_{x+y}}(\mathbf{k}) = \sqrt{2}\,\sin(k_x + k_y), \tag{3.58}$$

$$f_{2p_{x-y}}(\mathbf{k}) = \sqrt{2}\,\sin(k_x - k_y), \tag{3.59}$$

respectively. This procedure has to be applied successively to longer bonds until the truncation length is reached. In Appendix C, generalized formulas are given that allow for evaluating form factors at any bond length. Note that subspaces corresponding to bonds which do not lie on one of the symmetry axes (e.g., $i = 4$; see Fig. 3.1) are eight dimensional. In these cases, a complete basis contains four p-symmetric form factors. Due to the arrangement of the form factors as circles

with increasing radii around the origin, the basis functions corresponding to one subspace (or to one value of i) are called form-factor 'shell' in the following.

Compared to the bond-based representation, the choice of IR-based form factors is advantageous in terms of physical interpretations of the fRG results.[12] For instance, in the case of a leading d-wave superconductivity, the flow in the IR representation will show a strong signal in the $P_{1d_{x^2-y^2},1d_{x^2-y^2}}(\mathbf{l}=0)$ component, while this feature would be split into several parts in a bond-based flow. Furthermore, as contributions to one type of order get spread across many components by using the bond basis, a quantitative comparison of competing ordering tendencies is more complicated in that representation. Thus, the results presented in Chs. 4 and 5 are obtained by an IR-based flow.

3.3. Implementation

Despite all physically motivated approximations and truncations entering the TUfRG, the development of a method that is computationally efficient—i.e., that reduces the time-to-solution significantly while it provides meaningful predictions of ground state properties—relies on the usage of high-performance computers. During the last decade the building blocks of large computing architectures changed from single-core CPUs to compute nodes containing multiple cores, while large numbers of these nodes are interconnected in complex and heterogeneous networks. In order to take advantage of such massively parallel designs, a modern fRG implementation should be able to make use of a large number of compute cores. To this purpose, in the present implementation it is made extensive use of the directive-based OpenMP as well as the Message Passing Interface (MPI) API, which are the most used standards for achieving shared- and distributed-memory parallelization, respectively.

The code presented here is written in the programming language C++. In the following, the implementation of the TU flow equations is described briefly with a focus on the parallelization strategy. Afterwards, parallelization speedups are presented as they result from running the code on the JURECA compute cluster.

[12] However, in view of computational performance it might be beneficial to transform the exchange propagators into a bond-based representation before performing the inter-channel projection step and to transform back afterwards. In this way, the evaluation of overlaps between basis functions in real space should be significantly accelerated.

3.3.1. Brief Description of the Program Code

As discussed in Sec. 3.1, the computational advantage of the TU approach arises from the fact that the exchange propagators have been completely pulled out of the loop integrals. Consequently, the integrals defined as step (ii) on page 38 are generally more well behaved than in the exchange-parametrization approach. All loop integrations for different combinations of form factors and momentum are completely independent of each other and, therefore, embarrassingly parallel. In a distributed-memory parallelization, this step only requires communication between MPI processes for sharing the results of the integration tasks. Thus, a comparison of the time spent for communication to the one needed to perform calculations shows that the communication overhead is negligible in step (ii).

As the implementation has been developed further on a continuous basis, the code versions used in Chs. 4 and 5 for the integration step differ from each other. Both versions have in common that MPI is used to distribute external momenta across the available compute nodes. On the node level, however, different strategies for realizing shared-memory parallelization are applied in the codes. In the older version from Ch. 4 single integration tasks, i.e., the tasks with fixed form-factor indices, were distributed across the compute cores using OpenMP. Each integral, with fixed form-factor indices and momentum value, was then computed sequentially using the adaptive quadrature routine DCUHRE, which was written in FORTRAN 77 and published by J. Berntsen et al. in Ref. [67]. The newer code version from Ch. 5 is, however, based on the 'Parallel Adaptive Integration in two Dimensions' (PAID) library. PAID was originally developed by T. Vidović, J. Winkelmann, and E. Di Napoli. In a close collaboration of the aforenamed computer scientists, D. Sánchez de la Peña, and myself, PAID was further refined and tailored to the needs of the TUfRG. In contrast to the previous implementation, the newer version collects all integration tasks corresponding to a certain momentum value in one container and computes them adaptively. The tasks are thereby executed under just one parallel region exploiting the shared memory of a compute node. This way of implementation allows for controlling the global error of the integrations and, furthermore, reduces the load imbalance which, in turn, enhances the code's scaling properties with respect to the number of compute cores used. In a direct comparison with the DCUHRE implementation, the PAID version yielded speedups from $2\times$ up to $4\times$. Details on PAID's underlying algorithm and its parallel implementation can be found in Ref. [66].

For the implementation of the inter-channel projections, denoted by step (i) on page 38, the real-space representation as given in Eq. (3.29) was used. Even though this part of the code has continuously been improved as well, there are no structural differences between the versions from Chs. 4 and 5. As in the integration step, a hybrid scheme combining distributed- and shared-memory parallelization is applied. Here, MPI is used to distribute the sum over the indices

m' and n'—from the equation's right-hand side—across the compute nodes. For a fixed value of (m', n') the different components of the projected single-channel coupling, i.e., the objects specified by the indices m and n, are computed in parallel using OpenMP. A more detailed description of the implementation of step (i) can be found in Appendix B.

As the matrix multiplications from step (iii) are of minor importance in terms of computation time, the corresponding part of the program code is not optimized. The implementation is based on nested *for* loops, in which the ones iterating external indices are parallelized across the shared-memory level. Even though distributed-memory parallelism is unused, the computation time consumed by this step is negligible compared to the ones of steps (i) and (ii) for computations using up to 128 nodes.

After executing steps (i)–(iii) the right-hand sides of the ordinary differential equations (ODEs) (3.20)–(3.22)—the TU flow equations—are computed at a certain value of the fRG scale parameter. The iterative solution of an order one ODE is a standard task that is dealt with by an explicit solver from the 'Odeint' library (see Ref. [68]). The solver used here is based on the 'Adams-Bashforth' multi-step method. In order to reduce the number of evaluations per step, this type of ODE solver saves some part of the history and reuses the results from previous evaluations. Thus, if the computation of the ODE's right-hand side is particularly expensive—as it is in the present case—multi-step methods are preferable.

3.3.2. Scalability Properties on a High-Performance Cluster

The parallel performance of the implementation[13] was analyzed using the JURECA compute cluster, located at Jülich Supercomputing Centre. Every node is equipped with two Intel Xeon E5-2680 v3 Haswell CPUs having 12 cores each, working at 2.5 GHz. Due to simultaneous multithreading (SMT) every node of the JURECA cluster module supports 48 threads in total. As the TUfRG in the current implementation is limited by its consumption of computation time rather than its memory consumption, cluster nodes with small-sized main memory (128 GB) have been used. For the scaling tests the implementation was applied to the t-t' Hubbard model on the square lattice at van Hove filling and model parameters $t' = -0.3\,t$ and $U = 3\,t$. The timings used to calculate speedups, which are presented in the following, were obtained from measuring the runtime needed for one computation of the ODE's right-hand side at an fRG scale of $\Omega = 2{\times}10^{-3}\,t$.

In order to investigate the scaling behavior of the shared-memory parallelization, a single compute node was used to run the code at various numbers of OpenMP threads in the range from 1 to 48. As a purely sequential computation—one thread running on one node—has to be performed in this step, a restriction to relatively

[13] Here, the code used for the calculations presented in Ch. 4 is analyzed.

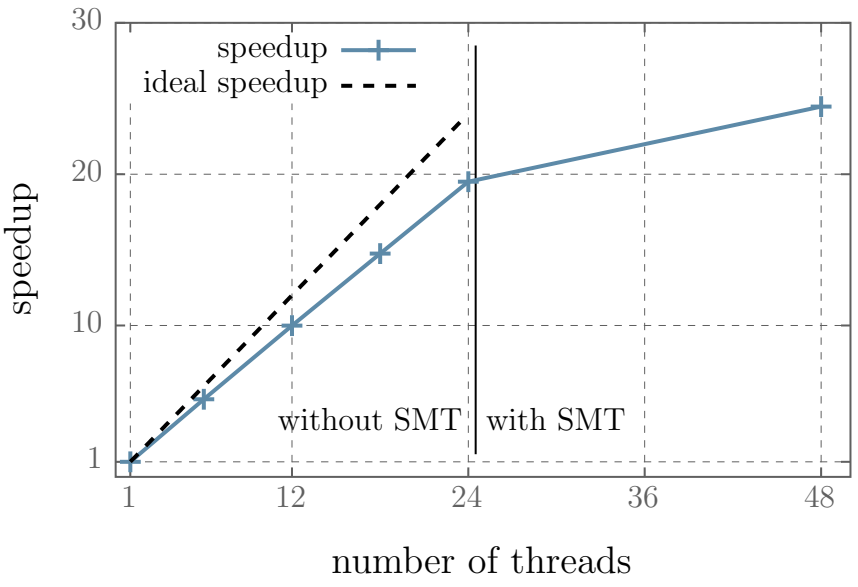

Figure 3.2. The plot shows the speedup gained from the shared-memory parallelization against the number of threads relative to sequential execution. For thread numbers up to 24 only a single thread is executed on each core. At 48 threads each core runs two threads at a time using simultaneous multithreading (SMT). The test was conducted on the JURECA compute cluster by applying the code to the Hubbard model on the square lattice. Details can be found in the main text.

low resolutions of momenta and a short truncation length compared with highly parallelized executions is necessary. Thus, the truncation of the form-factor basis is set to the fourth shell, i.e., only shells from $i = 0$ to $i = 4$ are included, and the density of momentum sampling points is drastically reduced compared to the ones shown in Fig. 4.1. The speedup[14] gained from the parallelization over shared memory is depicted in Fig. 3.2. In this context it is worth mentioning that the dashed line labeled by the term 'ideal speedup' is a bit misleading due to a technical feature of the CPUs called 'turbo boost'. This feature leads to higher CPU clocks when only a few cores are used and, thereby, reduces the value of the ideal speedup for higher numbers of threads. As this effect is not included in the dashed line plotted in Fig. 3.2, these values can not be reached in usual cases. Despite this fact, the speedup scales well in the range from 1 to 24 threads, reaching a value of 19.5 at an execution in 24 threads. In this range each thread runs exclusively on one core. Beyond that by using 48 threads, i.e., two per core, the underlying hardware parallelism is exploited resulting in a speedup of 24.5.

[14] The term speedup denotes the ratio of the runtime needed for the computation when a reference configuration is used and the time consumed by an improved computational setup. Here, the reference configuration runs the code purely sequential, while the accelerated setups use a higher number of threads for an execution on one node.

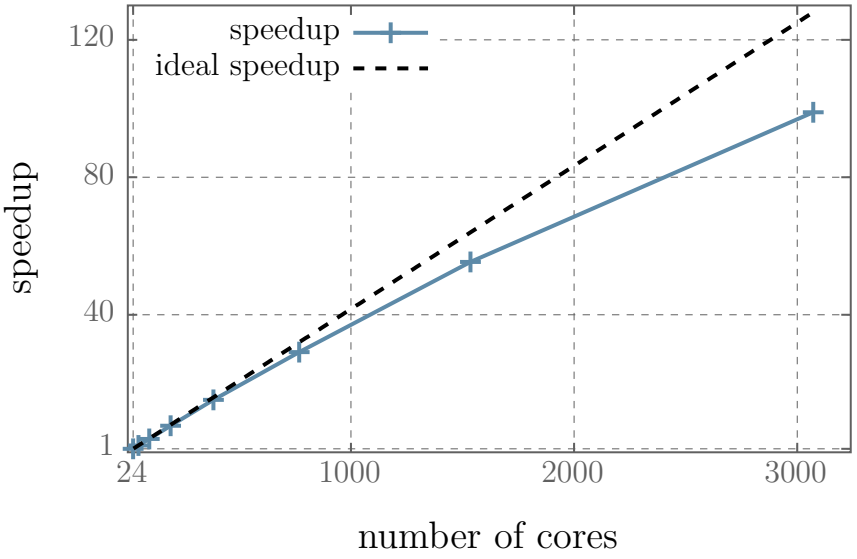

Figure 3.3. The plot shows the speedup gained from the distributed-memory parallelization against the number of used cores relative to an execution on a single node (24 cores). Here, each node is used exclusively by one MPI process running 48 threads. The test was conducted on the JURECA compute cluster by applying the code to the Hubbard model on the square lattice. Details can be found in the main text.

In a next step, the performance of the code in terms of distributed-memory parallelism is investigated. Fig. 3.3 shows resulting speedups relative to an execution on a single node, i.e., 24 cores, using 48 threads. In contrast to the previous scaling test, it is now possible to use the same momentum resolution as in the applications in Chs. 4 and 5. Furthermore, the form-factor basis is truncated at the fifth shell in this analysis, which is closer to the production conditions used in the applications. The implementation scales well in the investigated range while the curve plotted in Fig. 3.3 flattens slightly above 1500 cores ($\sim$64 nodes). The setup resulting in the fastest execution uses almost 3100 cores (128 nodes) and leads to a speedup of about 98.

Chapter 4.

Application: The Hubbard Model on a Square Lattice

In this first application of the TU approach, the focus is on the examination of the method's functionality. As the Hubbard model on the square lattice is well studied (cf. Refs. [25, 59, 62, 69, 70]) and was investigated by various fRG schemes, it is the ideal testing ground for the TUfRG implementation. The functionality of the scheme was studied in two ways: Firstly, as converged results—in terms of a smallest suitable form-factor truncation length—are a requirement for meaningful applications, a convergence test was conducted. Secondly, due to the relation to the exchange-parametrization scheme, a comparison with results generated by that scheme was drawn. Besides these technical aspects, the high momentum-space resolution of the implementation was utilized to conduct an analysis on ordering vectors of magnetic instabilities. Sec. 4.1 introduces the model Hamiltonian and specifies the numerical setup used. The results of the investigations are presented in Sec. 4.2.

Large parts of this chapter's content have already been published in Ref. [20]. Thus, the following text contains paraphrases of the one from the publication. As it is not always possible to reformulate a statement without changing its connotation, some formulations used here may be close or, in rare cases, even identical to the ones from Ref. [20].

After the publication of Ref. [20] an inaccuracy was detected in the computation of the projection part denoted by step (i) on page 38. The correction of that part led to only mild changes of the results in most of the investigated parameter range. Even though the scales close to the transition between ferromagnetic and superconducting phases—especially on the magnetic side—are affected to some extent, the correction does not affect the validity of the statements made within this chapter. However, discrepancies to the Hubbard results shown in Ch. 5 around the aforementioned transition point are explained by changes in the computation of the projection task.

4.1. The Hubbard Model on a Square Lattice

This section is meant to define the parameter values—the technical ones as well as the model parameters—that are used for calculating the results presented in the next section. For this purpose the model Hamiltonian, on which the TU approach was applied, is defined in the first part. After that, a description of the technical setup in terms of initial values and sampling point densities is given.

4.1.1. Model Hamiltonian

The one-orbital model Hamiltonian investigated here reads in second-quantization notation

$$H = \underbrace{-\sum_{\mathbf{r},\mathbf{r}',\sigma} t_{\mathbf{r},\mathbf{r}'}\, c^\dagger_{\sigma,\mathbf{r}}\, c_{\sigma,\mathbf{r}'}}_{=H_0} + \underbrace{\sum_{\mathbf{r}} U\, n_{\uparrow,\mathbf{r}}\, n_{\downarrow,\mathbf{r}}}_{=H_I}\,, \tag{4.1}$$

with lattice vectors $\mathbf{r}$ and $\mathbf{r}'$, spin orientation σ, and electron density operator $n_{\sigma,\mathbf{r}} = c^\dagger_{\sigma,\mathbf{r}}\, c_{\sigma,\mathbf{r}}$. The kinetic part H_0 is characterized by the hopping amplitudes $t_{\mathbf{r},\mathbf{r}'}$ between lattice sites $\mathbf{r}$ and $\mathbf{r}'$. In this work, the nearest-neighbor amplitude t as well as the second-nearest neighbor amplitude t' are taken into account. Together with the chemical potential μ, the hopping parameters determine the single-particle dispersion given by

$$\epsilon(\mathbf{k}) = -2\,t\,(\cos(k_x) + \cos(k_y)) - 4\,t'\,\cos(k_x)\,\cos(k_y) - \mu\,. \tag{4.2}$$

In addition to these three parameters, the on-site repulsion strength U appears in the interaction part H_I of the Hamiltonian. As a simultaneous rescaling of all four parameters will leave the physics of the system invariant, all energies are measured relative to t in the following.

Since this first application of the TU approach is meant for drawing a comparison to results from previous exchange parametrization studies (those of Refs. [3, 58]), the parameter values are chosen in accordance with these investigations. Thus, the computations are performed using $U = 3\,t$ and van Hove filling, i.e., $\mu = 4\,t'$, leaving t' as the only free parameter.

4.1.2. Numerical Setup

Within this analysis of the Hubbard model the initial scale is chosen to $\Omega_0 = 100\,t$ and the initial coupling is assigned to the scale-independent part of Eq. (3.1), i.e., $V^{(0)}_{k_1,k_2,k_3} = U$, while Φ^{P}, Φ^{C}, and Φ^{D} are initialized to zero in all components. It turned out that the results are very stable against increasing the initial scale further.

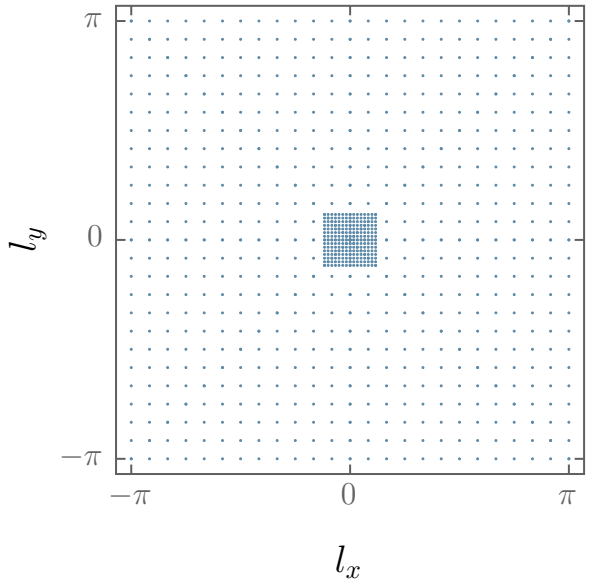

a) $\mathbf{P}(\mathbf{l})$: 992 sampling points

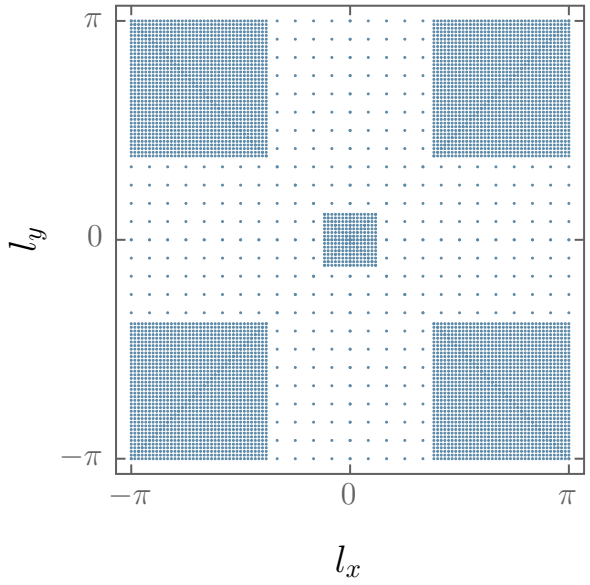

b) $\mathbf{C}(\mathbf{l})$ and $\mathbf{D}(\mathbf{l})$: 6632 sampling points each

Figure 4.1. Sampling-point distributions in the first BZ used for the discretization of the exchange propagators' momentum dependences are shown in the figures. As the channels differ in number and location of potentially singular momentum values, $\mathbf{P}(\mathbf{l})$ is discretized differently than $\mathbf{C}(\mathbf{l})$ and $\mathbf{D}(\mathbf{l})$.

The grids of sampling points used to describe the momentum dependence of the exchange propagators are shown in Fig. 4.1. From previous studies on this model (e.g., Ref. [3]) relevant ordering tendencies are already known, so that a denser grid is used around momenta at which the exchange propagators potentially develop strong peaks. As d-wave superconductivity (dSC) dominates in a part of the investigated parameter range, the vicinity of $\mathbf{l} = \mathbf{0}$ is sampled densely in the particle-particle channel (Fig. 4.1a). In the particle-hole channels, ferromagnetism (FM) appears at the ordering vector $\mathbf{l} = \mathbf{0}$ and (in)commensurate antiferromagnetism (AFM) emerges at (close to) $\mathbf{l} = (\pi, \pi)$. Fig. 4.1b exhibits high grid-point densities around those momenta accordingly.

4.2. Convergence Tests and Results

Before the results gained from applying the TUfRG to the Hubbard model are presented, in the first part of this section it is explained how physical information is extracted from the TU flow. Afterwards, the question is considered whether the insertion of truncated partitions of unity is a suitable approximation leading to meaningful results. For answering this question, two different indicators were examined: Firstly, the convergence behavior of the results with respect to increasing truncation length was tested and, secondly, a comparison to findings from previous exchange-parametrization studies was drawn. In the last part of this section, the high momentum-space resolution of the implementation was utilized to investigate ordering vectors in the magnetic channel.

4.2.1. Analysis of the TU flow

Using the initial conditions described above, the TU flow equations are solved iteratively generating exchange-propagator values at lower scales. Close to a model-parameter dependent scale—which is called *critical scale* (Ω_c) in the following—a specific exchange-propagator component strongly grows indicating a singularity in the coupling function.[1] The singularity in the coupling function in turn signals an instability in the metallic state and the transition towards some kind of ordered phase. However, due to bosonic fluctuations at scales below Ω_c, the temperature corresponding to the critical scale is only an upper bound for the onset of the phase transition. As the current fRG formalism is not suited for continuing the flow into a symmetry broken state, the computation is stopped at a scale slightly above the singularity. In the calculations presented here, the flow was stopped when the largest absolute value of the exchange propagators reached $20\,t$, which is

[1] Note that the existence of a critical scale depends on the system under investigation. Even in systems that exhibit a (semi)metallic state at high scales, the flow to low scales does not necessary lead to an instability of that state (cf. Ref. [71]).

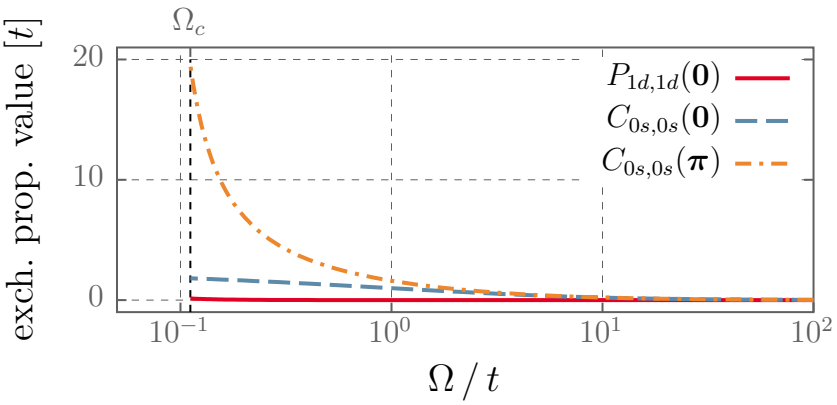

a) $t' = -0.1\,t$

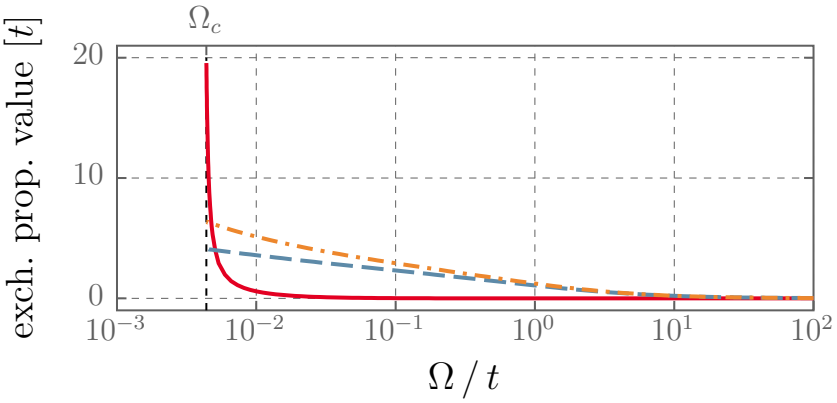

b) $t' = -0.3\,t$

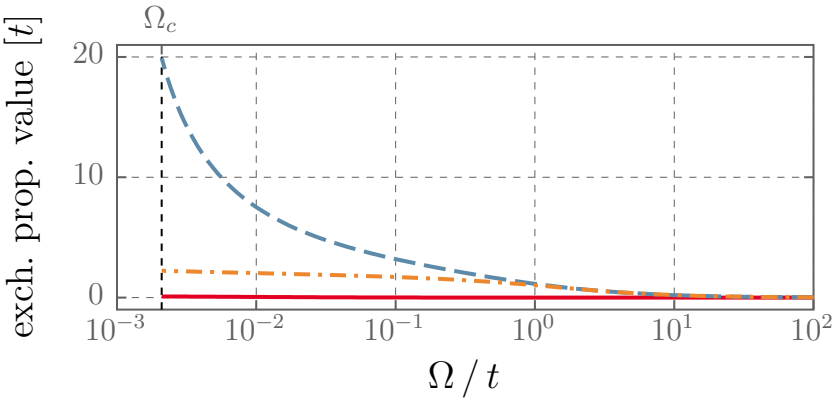

c) $t' = -0.4\,t$

Figure 4.2. The flows of the exchange-propagator components decisive for dSC (red, solid), FM (blue, dashed), and commensurate AFM (orange, dash-dotted) ordering are plotted against the fRG scale for three different values of the model parameter t'. While all model parameters are set according to Sec. 4.1, the computational setup from Ch. 5, in the variant that omits the long-range interactions, was used to calculate the values shown in this figure. The form-factor basis was truncated at the eighth shell.

of the order of the system's bandwidth. The scale at which a component reaches this bound is then used as an estimate for Ω_c. One may now investigate the properties of the ordered state by applying mean-field (MF) theory to the fRG outcome according to the procedure described in Ref. [24]. In the present work, however, a different path was followed, that is, the exchange-propagator component causing the termination of the flow was directly associated with the leading type of ground state. The ground state properties have been identified by means of the corresponding channel (pairing, magnetic, or charge), ordering vector ($\mathbf{l}$ value of the respective component), and the component's form-factor symmetry. This approach is less accurate than the fRG + MF combination, but it serves as a sufficient estimate for the needs of a method-focused study though.

For three different sets of model parameters Fig. 4.2 shows the resulting flows to strong coupling. These examples cover the ground-state types that have been observed during the course of this study.[2] Plot 4.2a indicates a transition towards an AFM state with ordering vector $\mathbf{l} = \boldsymbol{\pi} = (\pi, \pi)$, while another instability in the magnetic channel is shown in Plot 4.2c indicating FM order. An example for dSC, in which the total momentum of the two coupled particles is zero, is given in Plot 4.2b.

4.2.2. Convergent Phase Diagram

In order to investigate the convergence behavior of the TU flow with respect to an increasing form-factor truncation length, it was analyzed how the resulting scales change. As it is sensitive to changes in methodical details and, at the same time, allows for a simple comparison, the critical scale is used as main indicator for convergence in this study. The flow was performed in the parameter range from $t' = -0.1\,t$ to $t' = -0.45\,t$ using different truncations of the form-factor basis. Starting from a truncation at the first form-factor shell, the number of form factors was successively increased until all functions from the first six shells were included in the basis. Fig. 4.3 shows the critical scales against t' and marks three parameter regions, each being dominated by one of the ordering tendencies discussed before. For reasons of clarity the transitions between different phases are only shown sketchily in this plot. For both transitions, however, the transition values of t' turn out to change very mildly with respect to the truncation length.

In view of AFM order, Fig. 4.3 reveals that the critical scales are nearly unchanged by increasing the number of form factors. This shows that the important feedback coming from other channels—which lowers the critical scales compared to those from single-channel calculations—is already contained in the TU flow using a first shell truncation. Within the dSC-dominated parameter region the

[2] In this statement no distinction is made between commensurate AFM occurring at $\mathbf{l} = (\pi, \pi)$ and incommensurate AFM with an ordering vector close but not equal to (π, π).

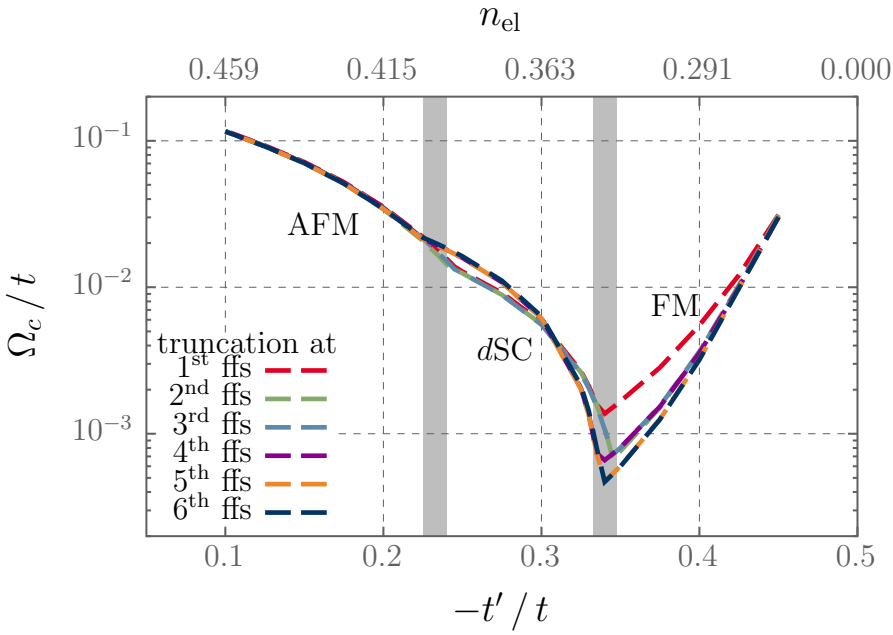

Figure 4.3. Critical scales are plotted against the model parameter t', while the electron density (top horizontal axis) is adjusted concurrently to keep the system at van Hove filling. The colors denote truncations at different form-factor shells (ffs). Gray bars separate the parameter regions of the observed instabilities, which are explained in the first part of this section.

critical scales change when the form factors corresponding to the fourth shell are added. However, except for t' values close to the phase transition towards FM, this correction is small. Moreover, Fig. 4.3 illustrates that systems located close to that transition are the most challenging ones in a numerical treatment. These convergence problems around $t' \approx -0.34\,t$ reflect the fact that the nature of this transition is controversial. There are fRG studies that observe a quantum critical point between the two phases (e.g., Refs. [25, 59]) while others—like the present one—do not indicate such a phenomenon (e.g., Ref. [3]). In the rightmost parameter region shown in Fig. 4.3, in which FM tendencies are strongest, a larger jump in the scales occurs from the first-shell to the second-shell truncation. Beyond that, the inclusion of longer-bond form factors has only a small impact on the results.

In summary, Fig. 4.3 reveals that the influence of form factors from shells beyond the second one is rather low within the investigated parameter range, except for values of t' close to the phase transition between dSC and FM.

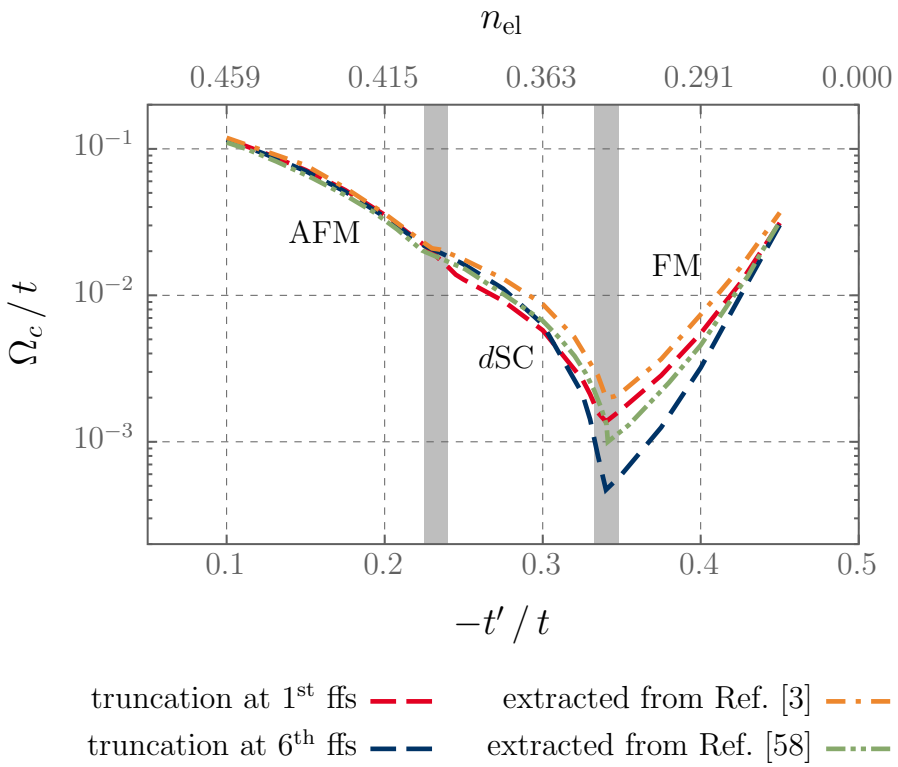

Figure 4.4. Critical scales are plotted against the model parameter t', while the electron density (top horizontal axis) is adjusted concurrently to keep the system at van Hove filling. The gray bars, separating the parameter regions, and the dashed lines (red and blue) are the same as in Fig. 4.3. For comparison, the dash-dotted lines (orange and green) are extracted from Refs. [3] and [58], respectively.

4.2.3. Comparison to Previous Studies

In Fig. 4.4 a comparison to findings from previous fRG studies is drawn. Data have been extracted from Fig. 6 of Ref. [3] and from curve (i) in the left part of Fig. 3 shown in Ref. [58] and are plotted together with the first-shell and sixth-shell truncation results from the present investigation. Since these reference studies analyzed the same model using exchange-parametrization fRG in the same truncation of the flow equation hierarchy as the current work, a direct comparison of critical scales is reasonable.

The curves in Fig. 4.4 are very similar in both the AFM and the dSC parameter region. In the region with dominating FM tendencies and around the transition point between dSC and FM, however, the scales from the older studies are closer to the current results from the first-shell truncation than to the higher-order findings. Generally, it is not surprising that critical scales are reduced by increasing the inter-channel feedback—which is the consequence of taking more form-factors into

account—when the influence of the subleading ordering tendency (dSC) on the dominant one (FM) has destructive character. Hence, the higher-shell truncation results from the present study can be seen as quantitative corrections to the critical scales from the two previous investigations within the FM region.

4.2.4. Incommensurate Antiferromagnetic Ordering Vectors

Due to the high momentum resolution of the magnetic channel around $\mathbf{l} = (\pi, \pi)$ it was possible to distinguish incommensurate from commensurate AFM phases and to determine the ordering vectors in the respective parameter region. Fig. 4.5 shows the momentum dependence—regarding one corner of first BZ—of the corresponding exchange-propagator component as it results from the TU flow at the critical scale. The data were extracted from computations on two systems with parameters $t' = -0.1\,t$ and $t' = -0.225\,t$, respectively, using the fifth-shell truncation. While in the upper plot the maximum value is located directly at $\mathbf{l} = (\pi, \pi)$ indicating commensurate AFM, the maximum in the lower plot is split yielding degenerate ordering vectors which are clearly away from the commensurate case. The ordering vectors obtained from the plots in Fig. 4.5 are drawn in Fig. 4.6 together with ordering vectors corresponding to intermediate values of t'. For reasons of comparison, ordering vectors resulting from bare AFM susceptibilities are shown in Fig. 4.7. These susceptibilities were evaluated at the critical scale of the respective system and the position of the largest value was taken as an ordering vector estimate. As this kind of estimate is based on information originating from the magnetic channel only, the comparison to fRG data reveals how the coupling between channels affects the AFM order. Since in each of the investigated systems the fRG ordering vector is closer to (π, π) than the one obtained from the bare susceptibility, the comparison yields that the inter-channel feedback generates support for commensurate orderings.

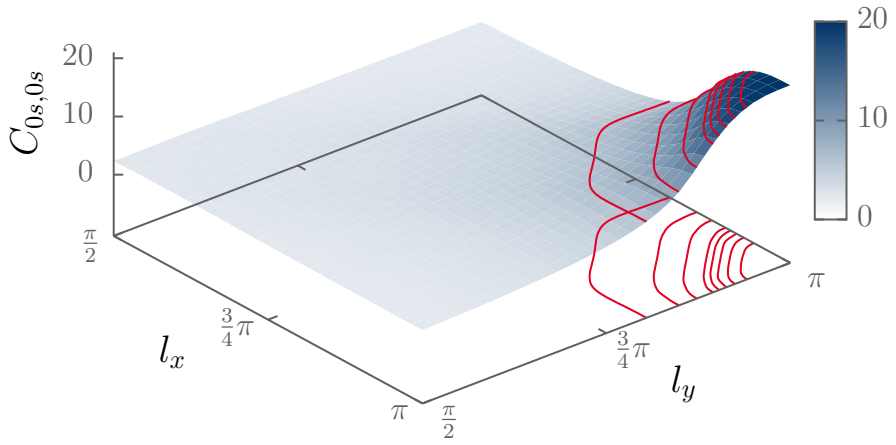

a) $t' = -0.1\,t$

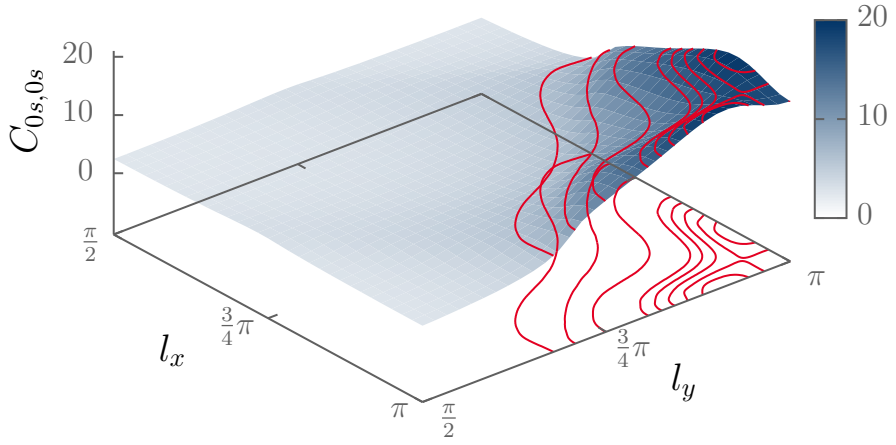

b) $t' = -0.225\,t$

Figure 4.5. For two different values of t' the momentum dependence of $C_{0s,0s}$ at the critical scale is shown in the plots regarding one corner of the first BZ. The data have been computed using a fifth-shell truncation of the form-factor basis.

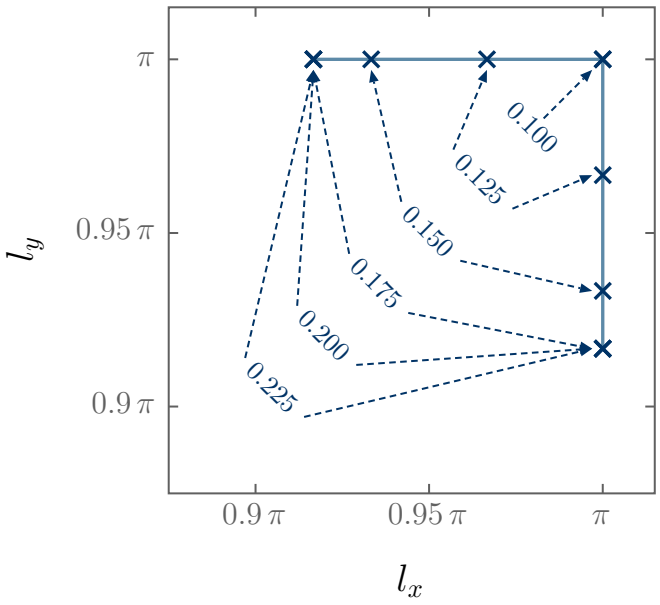

Figure 4.6. For different values of t' the figure shows leading AFM ordering vectors resulting from the TU flow, i.e., the respective maximum position of $C_{0s,0s}(\mathbf{l})$ at the critical scale (cf. Fig. 4.5). The labels denote the corresponding values of $-t'/t$. Note that in the case of incommensurate AFM order the ordering vector is degenerate.

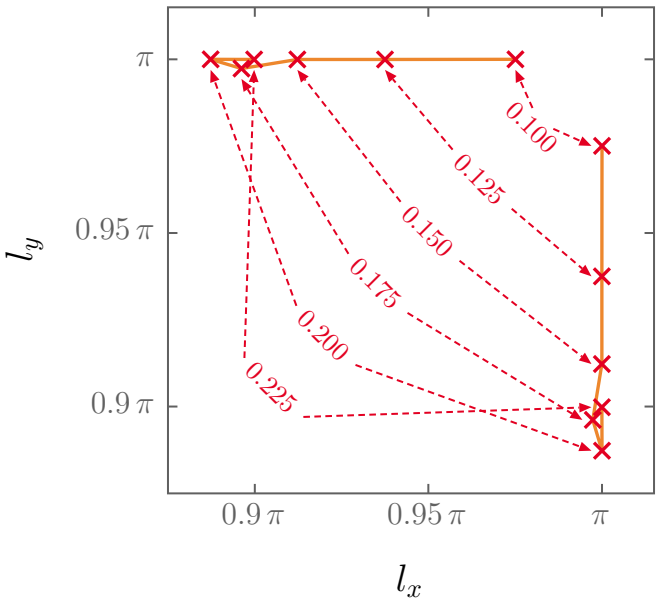

Figure 4.7. For different values of t' the figure shows leading AFM ordering vectors resulting from bare susceptibilities, i.e., the respective maximum position of the fermionic particle-hole loop $\chi_{\mathrm{ph}}(\mathbf{l})$ evaluated at the TU flow's critical scale. The labels denote the corresponding values of $-t'/t$. Note that in the case of incommensurate AFM order the ordering vector is degenerate.

Chapter 5.

Application: Study on Long-Range Interactions

As in the previous chapter, a translation invariant system on a square lattice is considered. However, in addition to the purely local Hubbard U, a Coulomb-like long-range term is now taken into account leading to a *Hubbard-Coulomb model*. In Sec. 5.1, a solution is presented on how the long-range interaction can be implemented in a momentum space fRG scheme without encountering singularities. Furthermore, different strategies to absorb the initial values in the channel decomposed interaction are discussed. Building on these deliberations, Sec. 5.2 presents convergence tests on the fRG results with respect to the value of the initial scale and to the number of form-factor shells. The tests are used to detect optimal values for those two technical parameters. After having established the setup for TUfRG investigations on the Hubbard-Coulomb model, the results obtained are presented in the last section. This involves phase diagrams comparing the Hubbard-Coulomb with the Hubbard model and the evolution of charge screening as function of the fRG scale.

5.1. Initial Interaction

The purely local interaction term from Eq. (4.1) is now extended by a long-range Coulomb tail, resulting in a Hubbard-Coulomb interaction of the form

$$H_I = \sum_{\mathbf{r}} U\, n_{\uparrow,\mathbf{r}}\, n_{\downarrow,\mathbf{r}} + \frac{1}{2} \sum_{\substack{\mathbf{r},\mathbf{r}' \\ \mathbf{r}\neq\mathbf{r}'}} \frac{e^2}{|\mathbf{r}-\mathbf{r}'|} \sum_{\sigma,\sigma'} n_{\sigma,\mathbf{r}}\, n_{\sigma',\mathbf{r}'} \tag{5.1}$$

with the density operator $n_{\sigma,\mathbf{r}} = c^\dagger_{\sigma,\mathbf{r}}\, c_{\sigma,\mathbf{r}}$ and the electron charge e. Due to the fRG setup described in Ch. 3, a Fourier transform to momentum space is necessary, which appears to be divergent in the case of zero transfer momentum as the sum $\sum_{\mathbf{r}\neq 0} \frac{1}{|\mathbf{r}|}$ does not converge. Since numeric treatments require a description based on regular expressions, the pure Coulomb interaction from Eq. (5.1) cannot be

used as an initial interaction within a momentum space fRG scheme. At this point it comes in handy that the initial scale Ω_0 of the fRG flow is large but finite. As the energy modes above the initial scale give rise to screening effects—at least in the case of a metallic system—, the divergence at zero momentum gets regularized.

In the following, the high energy screening effects are included into the initial interaction in two steps. At first, the action of the fermionic system is rewritten in terms of bosonic fields mediating the interaction between charges. After an integration of fermionic degrees of freedom, a closed expression for the screened interaction is derived. This procedure is closely related to the one demonstrated in Ref. [72]. In the second step, the expression found is evaluated numerically.

According to Eq. (3.1) the two-particle coupling splits up into four distinct parts within the TUfRG framework. The last part of this section provides a discussion on different possibilities to sort the Hubbard-Coulomb interaction into these four containers.

5.1.1. RPA Screening of a 2D Coulomb Repulsion

In order to sum up the screening contributions at energies above Ω_0, the interaction part of the Hamiltonian is transformed into momentum space

$$H_I = \frac{1}{2N} \sum_{\mathbf{k_1},\mathbf{k_2},\mathbf{k_3}} \sum_{\sigma,\sigma'} V(\mathbf{k_3} - \mathbf{k_2})\, c^\dagger_{\sigma,\mathbf{k_1}+\mathbf{k_2}-\mathbf{k_3}}\, c^\dagger_{\sigma',\mathbf{k_3}}\, c_{\sigma',\mathbf{k_2}}\, c_{\sigma,\mathbf{k_1}} \tag{5.2}$$

with the two-particle coupling

$$V(\mathbf{l}) = e^2\, \bar{V}(\mathbf{l}) = U + \sum_{\mathbf{r}\neq 0} \frac{e^2}{|\mathbf{r}|} e^{i\mathbf{r}\cdot\mathbf{l}}\,. \tag{5.3}$$

Then, the quartic part of the action can be expressed as

$$\mathcal{S}_I = \frac{T}{2N} \sum_l \rho(-l)\, e^2\, \bar{V}(\mathbf{l})\, \rho(l) \tag{5.4}$$

with the combined index $l = (l_0, \mathbf{l})$ and the collective charge field

$$\rho(l) = \sum_{\sigma,k} \bar{\psi}_\sigma(k+l)\, \psi_\sigma(k)\,, \tag{5.5}$$

in which $\bar{\psi}$ and ψ are fermionic fields. By a Hubbard-Stratonovich transformation, bosonic fields $\phi(l)$ are introduced that couple to the charge fields. This yields

$$\begin{aligned} e^{-\mathcal{S}_I} = \text{const.} \times \int \mathcal{D}[\phi^*, \phi] \, \exp\left\{ -\sum_l \phi^*(l) \, (\bar{V}(\mathbf{l}))^{-1} \, \phi(l) \right\} \\ \times \exp\left\{ ie\sqrt{\frac{T}{2N}} \sum_l \Big(\rho(-l) \, \phi(l) + \phi^*(l) \, \rho(l) \Big) \right\} \end{aligned} \tag{5.6}$$

which can be inserted into the right-hand side of the field integral representation of the partition function at scale Ω_0

$$Z^{\Omega_0} = \int \mathcal{D}[\bar{\psi}, \psi] e^{-\mathcal{S}_0^{\Omega_0} - \mathcal{S}_I} \, . \tag{5.7}$$

In the reformulation of the action in Eq. (5.6), the two-particle coupling $\bar{V}(\mathbf{l})$ has moved to the term quadratic in the bosonic fields. The bosons can be interpreted as mediators of the two-fermion interaction, whereat $\bar{V}(\mathbf{l})$ is the bare propagator[1] belonging to the bosonic degrees of freedom. Since the cutoff function in $\mathcal{S}_0^{\Omega_0}$ suppresses the fermionic degrees of freedom at scales below Ω_0, the integration over the fields ψ and $\bar{\psi}$ includes the high energy fermion modes into an effective bosonic description for the fermionic interaction at scales lower than Ω_0. After integrating out the fields ψ and $\bar{\psi}$ the effective action becomes

$$\mathcal{S}_{\text{eff}}^{\Omega_0} = \sum_l \phi^*(l) \, (\bar{V}(\mathbf{l}))^{-1} \, \phi(l) - 2 \, \text{tr}(\ln M^{\Omega_0}) \tag{5.8}$$

with the matrix M^{Ω_0} given by

$$M_{k,k'}^{\Omega_0} = -(G_0^{\Omega_0}(k))^{-1} \, \delta_{k,k'} - ie\sqrt{\frac{2T}{N}} \, \phi(k - k') \, . \tag{5.9}$$

An expansion of the second term in Eq. (5.8) in powers of the electron charge results in the action

$$\mathcal{S}_{\text{eff}}^{\Omega_0} = \sum_l \phi^*(l) \left[(\bar{V}(\mathbf{l}))^{-1} - e^2 \frac{2T}{N} \sum_k G_0^{\Omega_0}(k) \, G_0^{\Omega_0}(k + l) \right] \phi(l) + \mathcal{O}(e^4 \phi^4) \, , \tag{5.10}$$

in which constant terms have been omitted. Compared to Eq. (5.8), a second contribution appears as part of the quadratic action in Eq. (5.10). This additional term has the form of a fermionic particle-hole loop which is real valued and negative in the case of zero transfer frequency l_0 and close to zero transfer momentum $\mathbf{l}$. Taking into account the minus sign in front of the loop term, a positive value adds to the inverse interaction at $\mathbf{l} \to 0$ and leads to a regularization

[1] In this context, the term 'bare propagator' denotes the one-boson Green function, when the coupling between fermions and bosons—i.e., the second line of Eq. (5.6)—is omitted.

of the divergence of the bare interaction. At large values of Ω, the fermionic loop scales like Ω^{-1}, while the next higher order contribution shows a Ω^{-3} dependence. Consequently, higher order corrections can be neglected at high fRG scales. As the initial scale Ω_0 is usually chosen to be much larger than the bandwidth, this approximation—known as *Random Phase Approximation (RPA)*—is applicable at the initial stage. Hence, the two-fermion coupling that includes the effect of modes above Ω_0 in RPA is defined as

$$(\bar{V}^{\Omega_0}_{\mathrm{RPA}}(l))^{-1} = (\bar{V}(\mathbf{l}))^{-1} \underbrace{-e^2 \frac{2T}{N} \sum_k G_0^{\Omega_0}(k)\, G_0^{\Omega_0}(k+l)}_{=:\left(\lambda^{\Omega=\Omega_0}(l)\right)^{-1}}, \tag{5.11}$$

in which the momentum and frequency dependent screening length $\lambda^{\Omega}(l)$ is introduced.[2] Hereafter, the definition $\lambda_0 := \lambda^{\Omega=\Omega_0}(l_0 = 0, \mathbf{l})$ reflects the fact that at high scales and at zero frequency the particle-hole loop is structureless.

5.1.2. Numerical Evaluation

Prior to the evaluation of the RPA coupling from Eq. (5.11), the ratio between the bare on-site and nearest neighbor interactions has to be fixed to a reasonable value. In the current notation, this ratio can be expressed as U/e^2, while $U = 3\,t$ is chosen to be the same as in the previous chapter for reasons of comparison. Assuming that the underlying Wannier functions are sufficiently localized—which means that they decay on a length scale smaller than the lattice constant—, the above ratio should be chosen to a value greater than one. In order to obtain a more quantitative benchmark, ab initio parameters are good objects of comparison. Ref. [73] provides effective one-band parameters for 2D lattice systems on a Si(111) substrate derived by a combination of density functional theory and constrained random phase approximation. Those values indicate that a ratio of 2–3 between the on-site and nearest neighbor interactions is reasonable.[3] In the following $e^2 = t$ is used, which leads to the ratio $U/e^2 = 3$.

With regard to the evaluation of $V^{\Omega_0}_{\mathrm{RPA}}$, the Fourier transform of the bare coupling from Eq. (5.3) can be approximated by a finite number of Fourier components. This is due to the fact that the presence of a finite screening length λ_0 suppresses contributions corresponding to long distances $|\mathbf{r}| \gg \lambda_0$, i.e., terms with $|\mathbf{r}| > R$ are negligible provided that R is chosen to a large enough value. Using $\Omega_0 = 1000\,t$,

[2] As the lattice constant is set to unity within the present thesis, the object defined here as screening 'length' is dimensionless.

[3] Even though these values correspond to triangular lattice systems, they should be suitable for deducing meaningful magnitudes also for square lattice systems. This applies in particular to the present study, as it is not focused on one specific material but on the impact of long-range interactions from a more general point of view.

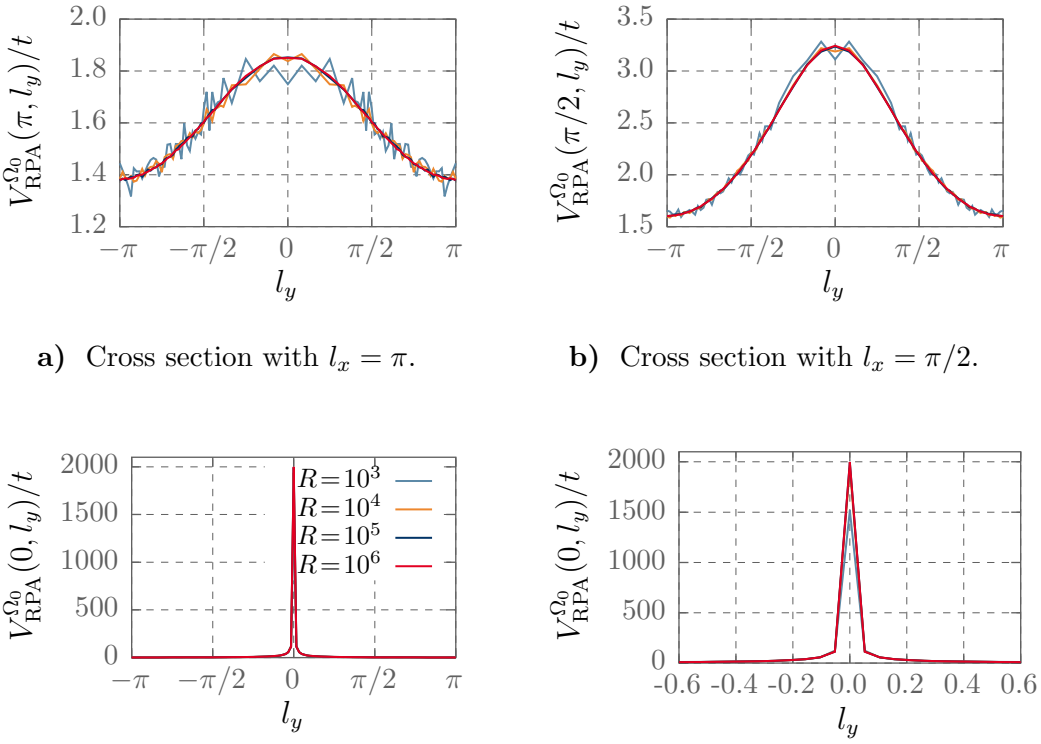

a) Cross section with $l_x = \pi$.

b) Cross section with $l_x = \pi/2$.

c) Cross section with $l_x = 0$.

d) Zoom of Fig. 5.1c.

Figure 5.1. The momentum dependence in l_y direction of the RPA coupling function $V^{\Omega_0}_{\mathrm{RPA}}$ at $\Omega_0 = 1000\,t$ is plotted for different values of l_x, while the frequency l_0 is set to zero. The Fourier transform of the bare coupling was evaluated using different truncation radii R that exclude all terms with $|\mathbf{r}| > R$ from the summation. At $R = 10^6$ the (red) curve is close to convergence.

which results in an initial screening length $\lambda_0 = 2000$ in units of the lattice constant, the convergence behavior of $V^{\Omega_0}_{\mathrm{RPA}}$ with respect to an increasing value of R was investigated. Fig. 5.1 shows the momentum structure of $V^{\Omega_0}_{\mathrm{RPA}}$—as in Ch. 4 the frequency l_0 will be set to zero—, in which the sum over lattice sites from Eq. (5.3) is truncated at different radii R. At $R = 10^3$ the coupling strength appears to be strongly buckled at the border of the BZ and to be significantly smaller than $e^2\lambda_0$ at $\mathbf{l} = 0$. However, the bare coupling V is divergent at $\mathbf{l} = 0$ and thus a good approximation should give an RPA coupling value close to $e^2\lambda_0$ at vanishing momentum. A comparison of the curves from Fig. 5.1 shows that with increasing R the buckling disappears and the peak at $\mathbf{l} = 0$ grows towards the expected value. In the following, the coupling function computed with $R = 10^6$ is used as starting point for fRG calculations, as the corresponding values are sufficiently close to convergence.

In Section 2.1 the statement is made that at high scales a small interaction is re-

quired to *ensure* the validity of the level-two truncation. As Fig. 5.1 shows, initial long-range interactions close to $\mathbf{l} = 0$ can be huge compared to the bandwidth of the system. The question arises whether a treatment of this special kind of interaction profile using the present fRG scheme can be valid nonetheless. In the literature, traditional approaches to study screening effects in electron systems—e.g., Thomas-Fermi approximation or RPA—are only justified in the case of very high electron densities (cf. Refs. [72, 74]). In many cases, this condition is not met as it is not in the present system. However, following the argumentation given above, RPA is valid at high scales Ω due to the regulation of the bare propagator. This in turn means that an fRG treatment is justified at high scales, as it contains all RPA contributions. On the one hand, with decreasing Ω this argument loses its sharpness, but at the same time the peak at $\mathbf{l} = 0$ gets screened on the other hand. The contrary nature of these two effects makes it difficult to conclude whether the regime of high scales—as defined in Ref. [15]—is treated correctly within the level-two truncation. In any case, an fRG study on long-range interactions provides quantitative corrections to RPA-screening theory and is suitable for revealing qualitative changes in the interplay between different ordering tendencies compared to investigations on purely local interactions.

5.1.3. Channel Decomposition

The TU approach is based on splitting the two-particle coupling into four parts according to Eq. (3.1). This opens up a variety of different ways to sort the above found initial interaction into these four containers. On the level of Eq. (3.1), the only restriction is that the three Φs and $V^{(0)}$ must add up to the initial coupling. However, as soon as the operators defined in Eqs. (3.7)–(3.9) are used to project the single-channel couplings onto a truncated form-factor basis, truncation errors lead to inequivalent fRG results for different handlings of the initial long-range interaction. Those differences are caused by non-convergent numerics due to inappropriate parametrization: The projections of the coupling at the initial scale $V^{\Omega_0}_{\mathrm{RPA}}(\mathbf{k_3} - \mathbf{k_2})$ are given by

$$\hat{P}[V^{\Omega_0}_{\mathrm{RPA}}]_{m,n}(\mathbf{l}) = \hat{C}[V^{\Omega_0}_{\mathrm{RPA}}]_{m,n}(\mathbf{l}) = \int d\mathbf{k}\, d\mathbf{k}'\, f_m(\mathbf{k})\, f_n(\mathbf{k}')\, V^{\Omega_0}_{\mathrm{RPA}}(\mathbf{k} - \mathbf{k}')\,, \tag{5.12}$$

and

$$\begin{aligned} \hat{D}[V^{\Omega_0}_{\mathrm{RPA}}]_{m,n}(\mathbf{l}) &= \int d\mathbf{k}\, d\mathbf{k}'\, f_m(\mathbf{k})\, f_n(\mathbf{k}')\, V^{\Omega_0}_{\mathrm{RPA}}(\mathbf{l}) \\ &= V^{\Omega_0}_{\mathrm{RPA}}(\mathbf{l})\, \delta_{m,0s}\, \delta_{n,0s}\,. \end{aligned} \tag{5.13}$$

The expression in Eq. (5.13) contains all information already within the on-site form-factor contribution. In contrast, the integral in Eq. (5.12) is proportional to

r_{mn}^{-1}, i.e., it decreases slowly with respect to the form-factor bond length.[4] If one chooses, for instance, $V^{(0)}$ to contain the initial long-range coupling as a whole, in a metallic system screening effects will cause a strongly growing $D_{0s,0s}(\mathbf{l}=0)$ leading to a cancellation of the Coulomb peak $V_{\mathrm{RPA}}^{\Omega_0}(\mathbf{l}=0)$. The cancellation will work fine in calculations in the direct particle-hole channel. In the other two channels, however, the projections of $D_{m,n}$ and $V^{(0)}$ will be highly inaccurate—as argued above—leading to an inexact cancellation of the corresponding terms in Eqs. (3.25) and (3.26).

Such problems can be avoided by initializing the density-density interaction from the long-range tail in $D_{0s,0s}$. In this case, screening effects will lead to a direct decrease of the peak at zero momentum in the same object, which prevents the formation of a counter term. Though the local Hubbard U is intended to originate from a density-density interaction in the present study, it is accurately described in each channel. In that case, each of the projections

$$\hat{P}[U]_{m,n}(l) = \hat{C}[U]_{m,n}(l) = \hat{D}[U]_{m,n}(l) = U\,\delta_{m,0s}\,\delta_{n,0s} \tag{5.14}$$

contains all the information in the component with both indices labeling on-site form factors. Thus, all possible initializations of U are equivalent. In this study, the on-site interaction is—for the sake of simplicity—contained in $D_{0s,0s}$ together with the long-range tail.

5.2. Convergence Tests

In the numerical evaluation of the initial two-particle coupling, $\Omega_0 = 1000\,t$ was used as initial scale. However, it has not yet been clarified whether this is a reasonable choice. Since at all scales above Ω_0 only contributions from the charge channel are summed up, a too small initial scale would lead to a loss of information from other channels and of inter-channel feedback. Then again, a too large initial scale causes additional iterations within the fRG-flow procedure, but without producing other information than RPA does. Thus, it would lead to higher consumptions of computation time without additional value. In order to find the most reasonable value for Ω_0, it is therefore necessary to examine the convergence behavior of the fRG results respect to a successive increase of the initial scale. Furthermore, an appropriate size of the form-factor basis that is suited to the current model needs to be found. Even though, this has been investigated in Ch. 4 with regard to the Hubbard model, a separate analysis adjusting the number of form factors to the Hubbard-Coulomb model is advisable. This is because long-range interactions do potentially generate contributions that are not present in the case of purely local interactions and, at the same time, require form-factor shells from longer-distant bonds.

[4] This statement holds, if both form factors f_m, and f_n belong to the same bond length r_{mn} and if λ_0 is much larger than r_{mn}.

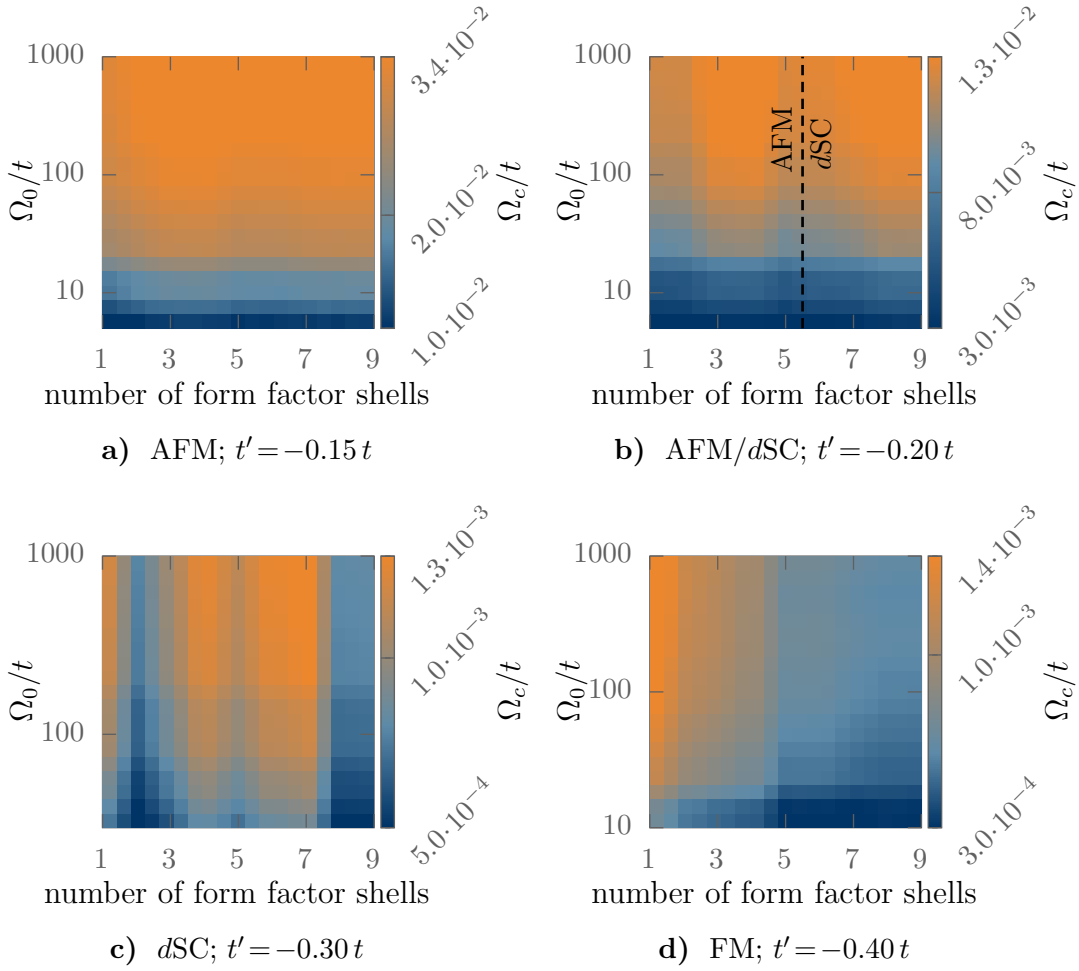

a) AFM; $t' = -0.15\,t$ **b)** AFM/dSC; $t' = -0.20\,t$

c) dSC; $t' = -0.30\,t$ **d)** FM; $t' = -0.40\,t$

Figure 5.2. Using four different sets of system parameters, the critical scale Ω_c is shown as function of the initial scale Ω_0 (vertical axis) and the number of form-factor shells (horizontal axis). While the interaction parameters are chosen as stated in Sec. 5.1, the next-to-nearest neighbor hopping amplitude t' is changed from plot to plot in order to cover the different ordering tendencies (given separately for each plot) that were found in the previous chapter. In each case, the value of the chemical potential is adapted to adjust the filling at the van Hove point.

Aiming at optimal values for both the initial scale Ω_0 and the number of form-factor shells n_{ffs},[5] a two dimensional convergence test was applied to the model using four different sets of system parameters. While the chemical potential μ was adjusted to keep the system at van Hove filling, the next-to-nearest neighbor hopping amplitude t' was set to $-0.15\,t$, $-0.20\,t$, $-0.30\,t$, and $-0.40\,t$, respectively. As different electronic orders are supported by distinct contributions, the values of t' were selected in order to cover all dominant ordering tendencies found in Ch. 4. Initially, $-0.20\,t$, $-0.30\,t$, and $-0.40\,t$ were chosen as representatives for AFM, dSC, and FM dominated situations, respectively. During the computation, $t' = -0.20\,t$ turned out to switch from an AFM to a dSC dominated system when the long-range interaction term in Eq. (5.1) was added. Thereupon, $t' = -0.15\,t$ was included as a clear representative of an AFM system. The parameters controlling the interaction part of the model Hamiltonian were chosen as described in the previous section.

Fig. 5.2 shows the resulting critical scales as function of the parameters under investigation. As in the previous chapter, the critical scale is used to study the convergence, since it is sensitive to changes in methodical details and, at the same time, allows for a simple comparison. In the vertical direction, the four plots in Fig. 5.2 show a clear saturation of the critical scale. Especially in the range from $\Omega_0 = 100\,t$ to $\Omega_0 = 1000\,t$ the value of Ω_c is nearly unchanged indicating that the scheme produces converged results at $\Omega_0 = 1000\,t$. In the horizontal direction, however, the parameter sets tested show very different behaviors. Focusing on the plot corresponding to $t' = -0.15\,t$, which represents an AFM ground state, the critical scale is almost constant in the whole range from 1 to 9 form-factor shells. As in the second plot the type of dominant ordering tendency changes from 5 to 6 form-factor shells, the system in which the next-to-nearest neighbor hopping amplitude is set to $-0.20\,t$ appears to be located directly at the transition between AFM and dSC dominated ground states. While the switch from one ordered state to the other is accompanied by a dip of the critical scale, the plot exhibits a plateau in its top-right corner ranging from 7 to 9 shells in horizontal direction. By going deeper into the dSC parameter region and investigating $t' = -0.30\,t$, the convergence behavior gets more unclear. Since contributions even from the 8th form-factor shell have an important impact on the scale at which the system becomes unstable, the plateau shrinks to the range from 8 to 9 shells. This result indicates that convergence is possibly achieved at $n_{\text{ffs}} = 8$, but it does not allow for a final conclusion. Thus, a further investigation—i.e., a computation using 10 form-factor shells—is necessary to clarify the situation. As a representative of an FM scenario, the last plot is computed using $t' = -0.40\,t$ and exhibits a broader

[5] In addition, the number and position of momentum sampling points for representing the exchange propagators are important adjustment parameters. A careful investigation on the convergence behavior of the results from fRG calculations with respect to the density of these sampling points has to be conducted. In such a test, the grid point distribution from Fig. 4.1 proved to be sufficiently dense also in the present case of long-range initial interactions.

plateau from 5 to 9 shells.

Since an analysis on competing instabilities is presented in the next section, the investigated parameters should be set to values that lead to converged results in consideration of all relevant ordering tendencies. Summarizing the information obtained from Fig. 5.2, setting $\Omega_0 = 1000\,t$ and $n_{\text{ffs}} = 8$ is reasonable, while especially the latter requires further verification. Before the analysis of the convergence in horizontal direction is expanded, Fig. 5.3 shows a cross section of Fig. 5.2 in vertical direction with a fixed $n_{\text{ffs}} = 8$. Due to the reduced dimensionality of the plot, the degree of convergence can be estimated more accurately. The figure illustrates clearly that at $\Omega_0 = 1000\,t$ the critical scale saturates up to a few percent. In view of the behavior of Ω_c as function of n_{ffs}, the investigated parameter region was extended by computations using 10 form-factor shells in the case of leading dSC ordering tendency, i.e., in the systems with $t' = -0.20\,t$, and $t' = -0.30\,t$. Due to limited computer resources, higher order shells were not accessible. In Fig. 5.4 a cross section in horizontal direction—while setting $\Omega_0 = 1000\,t$—is plotted including both additional data points at $n_{\text{ffs}} = 10$. The figure provides further evidence that the most important contributions are included in computations based on 8 form-factor shells. Even though the results on $t' = -0.30\,t$ do not exclude all doubts about the previous statement, it is reasonable that the importance of the feedback originating from increasingly long-distant form factors to the nearest-neighbor d-wave ordering tendency is monotonically decreasing. Thus, it is likely that contributions from shells beyond the ones investigated here are of minor relevance.

5.3. Results

The model system derived in the two preceding sections is now used to study particles on a square lattice that interact via a long-range Coulomb repulsion. In a first investigation, the impact of adding the non-local interaction terms to the on-site Hubbard U is studied and comparative phase diagrams are presented. The second investigation is focused on charge screening, which is quantified by the extraction of screening lengths from the fRG flow. These values are compared with results calculated in RPA.

5.3.1. Comparative Phase Diagrams

Fig. 5.5 shows critical scales and leading instabilities at van Hove filling as function of t'.[6] While the blue (dashed) curve is computed using the model derived in

[6] Note that the electron density that corresponds to van Hove filling changes as t' is varied. The top horizontal axis of Fig. 5.5 provides values of the respective van Hove density.

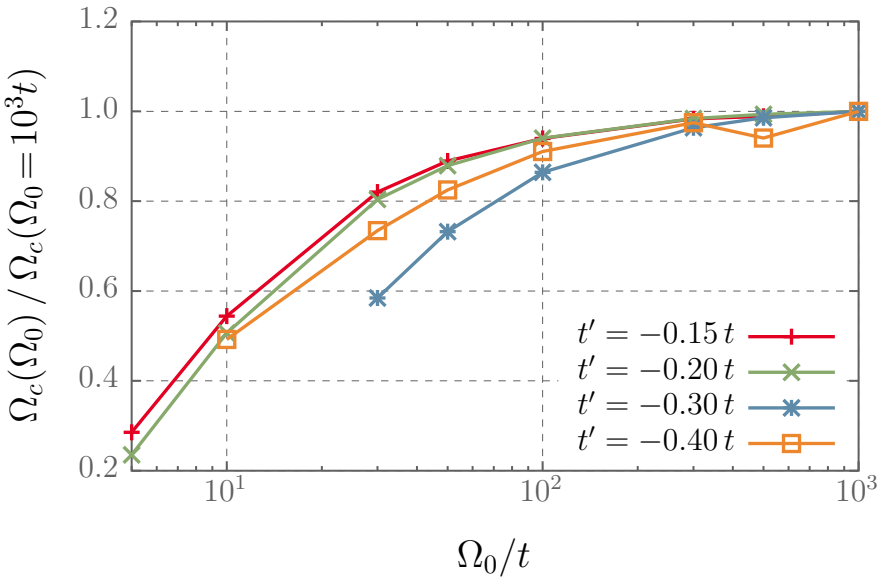

Figure 5.3. A cross-sectional view on the plots from Fig. 5.2 is shown at $n_{\text{ffs}} = 8$, providing a closer look at the convergence behavior with respect to Ω_0. In favor of comparability, the curves are rescaled so as to coincide at $\Omega_0 = 1000\,t$.

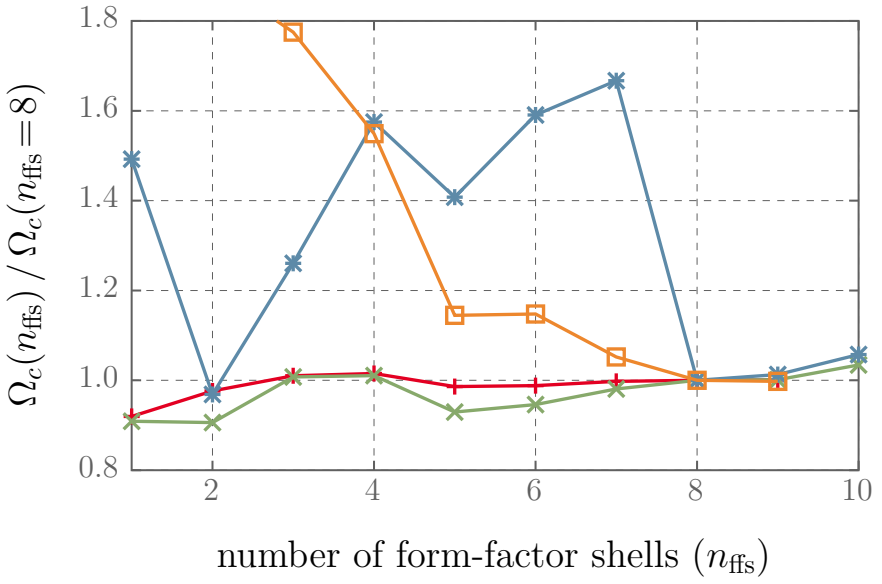

Figure 5.4. As in the previous figure, a cross-sectional view on the plots from Fig. 5.2 is shown. Here, the initial scale is fixed to $1000\,t$ providing a closer look at the dependence of Ω_c on the number of form-factor shells. In addition to the data shown in Fig. 5.2, resulting scales at $n_{\text{ffs}} = 10$ are given for dSC dominated systems. In favor of comparability, the curves are rescaled so as to coincide at $n_{\text{ffs}} = 8$. Colors and symbols are the same as in the previous figure.

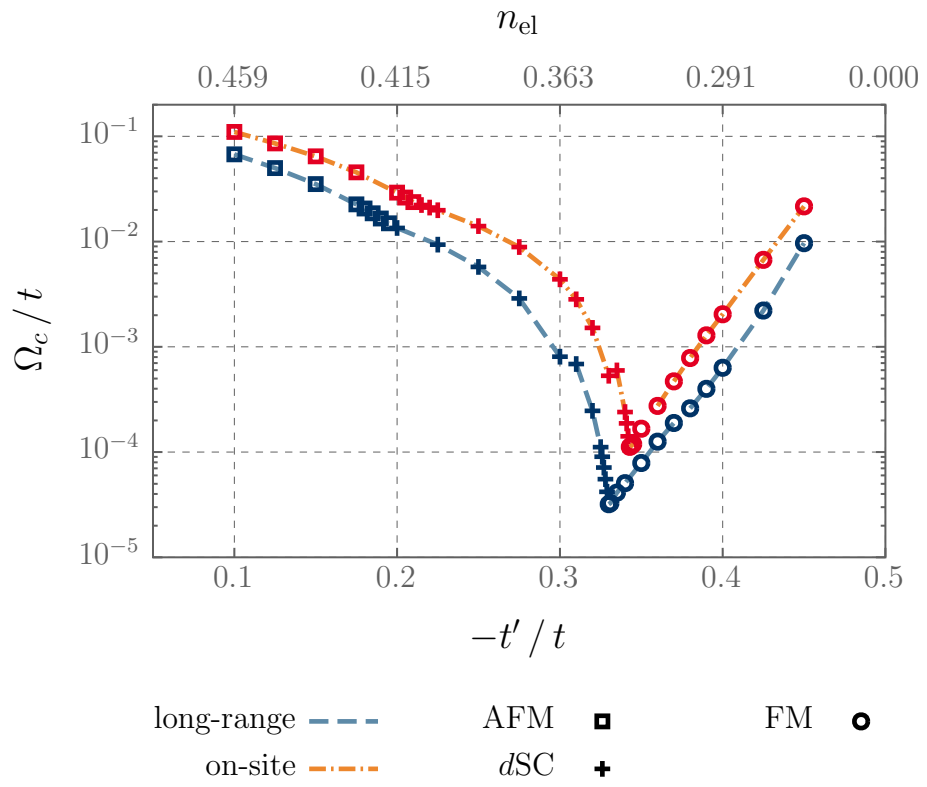

Figure 5.5. Critical scales are plotted against the model parameter t', while the electron density (top horizontal axis) is adjusted concurrently to keep the system at van Hove filling. Information on the dominant ordering tendency is contained in the symbols. The results from using long-range interactions are compared with the scales found by using the on-site term only. Due to huge computational effort at low scales, the number of form-factor shells had to be reduced to 6 in the intervals $t' \in [-0.37\,t,\, -0.31\,t]$ in the long-range case and $t' \in [-0.350\,t,\, -0.335\,t]$ in the on-site case, respectively.

the two preceding sections, the red (dash-dotted) line corresponds to the case of using the on-site Hubbard U term only. Technically, the latter scenario is deduced from the long-range model by setting $e^2 \to 0$. Even though the number of form factor shells should at least be set to eight in order to get converged results, the form-factor basis had to be truncated earlier at parameter values close to the transition between dSC and FM order. This is due to the extremely low critical scales in that parameter region, which were not accessible within the available computer resources using eight form-factor shells. Instead, the basis was truncated at the sixth shell within the t' intervals given in the figure caption. The resulting discontinuities of the curves at the interval borders reflect the drop of quantitative accuracy between two neighboring points.

In Ref. [71] the same method was applied to an electronic model for graphene. There it was found that the inclusion of the long-range Coulomb tail leads to a

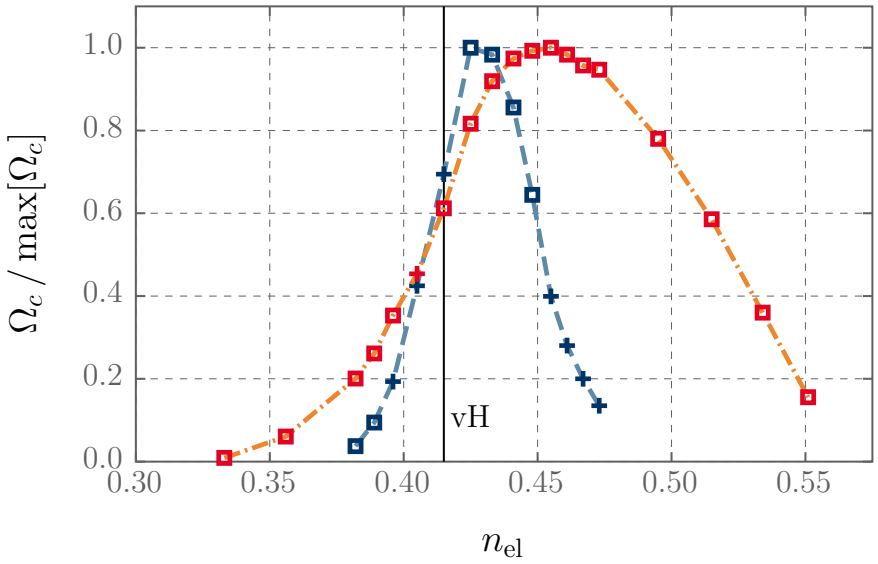

Figure 5.6. While t' is fixed to $-0.2\,t$, the critical scale is shown as function of the electron density in the vicinity of van Hove filling. As in Fig. 5.5, the model with long-range interaction is compared with one including the on-site term only. For better comparability, the curves are rescaled independently to a maximum value of one. In absolute numbers, the maximum values are about $0.019\,t$ and $0.048\,t$ in the cases of long-range and purely on-site interaction, respectively. Lines, colors, and symbols are the same as in Fig. 5.5.

competition between various (charge type) ordering tendencies, which are represented by different patterns on the direct lattice. Many of those patterns are pairwise incompatible resulting in geometrical frustration and in a stabilization of the semimetal. Of course, the situation is not the same in a square-lattice system—especially when it is set to van Hove filling—, but the geometrical frustration still has an effect on the critical scales. In contrast to graphene, the AFM order is not completely suppressed due to a non-vanishing density of states at the Fermi level in the system under investigation. However, Fig. 5.5 shows that the critical scales are reduced by almost a factor of two in the parameter region dominated by AFM order. The region that shows FM tendencies is even more strongly affected. As instabilities towards d-wave SC are driven by an AFM spin-fluctuation mechanism in this system[7], a weakening of the magnetic channel is directly passed on to that kind of SC. Consequently, the critical scales in the corresponding parameter region are lower in the long-range case. Furthermore, it is striking that the transition to FM dominated ground states happens earlier, which again emphasizes a diminished spin-fluctuation mechanism.

[7] In the present system, the AFM spin-fluctuation mechanism is known to be the driving force behind interactions becoming attractive in the particle-particle channel.

Results of an investigation on systems with electron densities away from the van Hove point are shown in Fig. 5.6. Here, t' is fixed to $-0.2\,t$ and the fRG flow is performed for different densities studying both the long-range and the purely on-site interaction. For better comparability, the two curves are rescaled independently to a maximum value of one. Starting at the van Hove density, electron doping leads to higher critical scales in both cases, even though the density of states at the Fermi level decreases. As shown in Ref. [16], this effect can be related to the appearance of AFM hot spots, i.e., intersections of the FS with the lines that connect $(\pm\pi, 0)$ and $(0, \pm\pi)$, supporting commensurate AFM order.[8] Since the latter mechanism is absent on the hole-doped side, the scales are drastically decreasing with respect to a reduction of the electron density. The different widths of the peaks on the electron doped side indicate that the magnetic ordering tendency is less robust when long-range interactions are taken into account. Again, the competition in the charge sector is likely to suppress magnetic order, which narrows the window of high-scale AFM. In the system with $t' = -0.2\,t$, AFM and dSC order are very close (cf. Fig. 5.5). Due to its relation to AFM spin fluctuations, d-wave SC is suppressed as well in the long-range scenario. However, the figure shows that the parameter region of leading dSC is expanded compared with the on-site case.

5.3.2. Screening Lengths

In Sec. 5.1, an RPA scheme is used to find meaningful values for the coupling at the initial stage of the fRG flow. The resulting expression in Eq. (5.11) is given in a form that allows to identify the second part of the right-hand side as a screening term at the initial scale, which is now generalized to scales below Ω_0, yielding

$$\lambda^{\Omega}_{\mathrm{RPA}}(l) = \left(-e^2 \frac{2T}{N} \sum_{k} G^{\Omega}_0(k)\, G^{\Omega}_0(k+l) \right)^{-1} . \tag{5.15}$$

Since only the $\mathbf{l} = 0$ term is interpretable as a screening length in real space, $\lambda^{\Omega}_{\mathrm{RPA}} = \lambda^{\Omega}_{\mathrm{RPA}}(l = 0)$ is considered in the following.[9] As argued in Sec. 5.1, the approximation used to derive this expression is only valid at values of Ω much larger than the band width. Nevertheless, the above formula has been evaluated at all orders of magnitude—from the initial scale down to the critical scale—serving as an object of comparison for the fRG data.

[8] In Ref. [69], it is shown that in the presence of hot spots self-energy renormalizations play an important role. Due to a flattening of the FS the critical scales get strongly enhanced compared with flows that ignore self-energy corrections. However, it seems unlikely that such a behavior affects the main statements of this section.

[9] Since bosonic frequencies are set to zero in all fRG calculations presented here, $l_0 = 0$ is used in the calculation of RPA screening lengths as well in order to allow for a comparison.

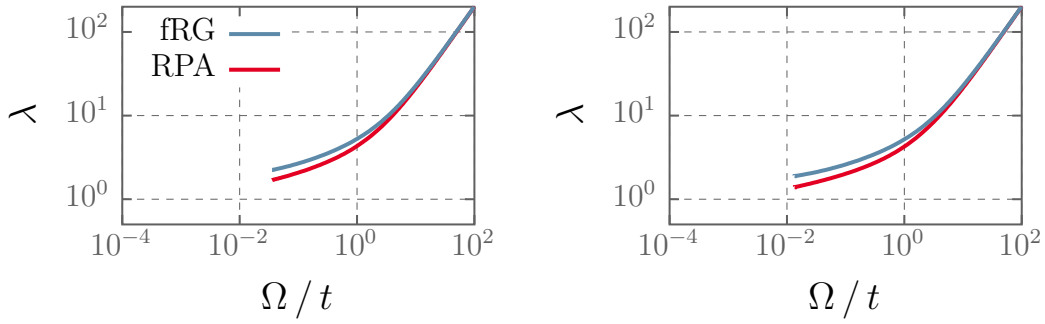

a) $t' = -0.15\,t$; van Hove filling

b) $t' = -0.20\,t$; van Hove filling

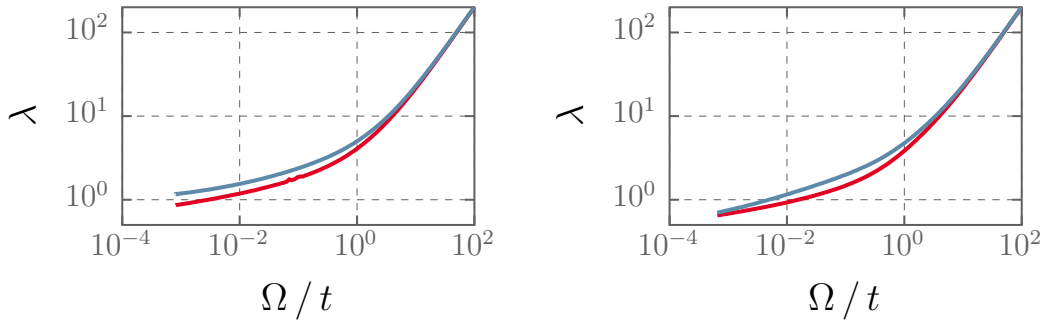

c) $t' = -0.30\,t$; van Hove filling

d) $t' = -0.40\,t$; van Hove filling

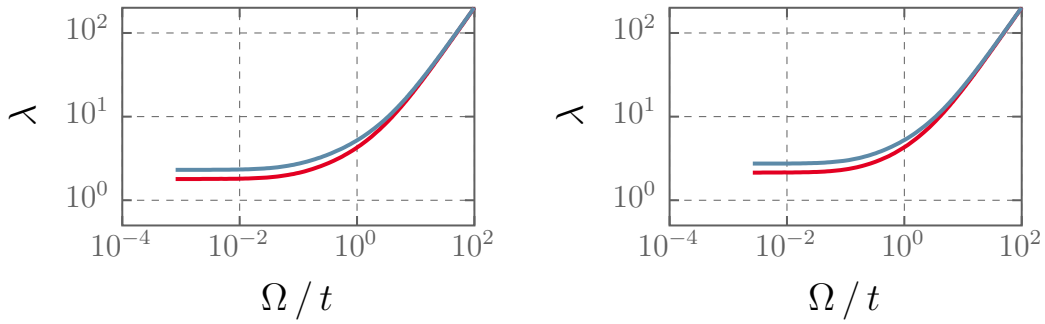

e) $t' = -0.20\,t$; $n_{\mathrm{el}} = 0.382$

f) $t' = -0.20\,t$; $n_{\mathrm{el}} = 0.473$

Figure 5.7. Plots of the screening length vs. the fRG scale are shown for six combinations of t' and electron filling. The figures compare the screening length computed from the fRG flow with the one resulting from RPA. Since the critical scale differs from one parameter set to the other, the curves end at differently low scales. Details on how these values are obtained can be found in the text.

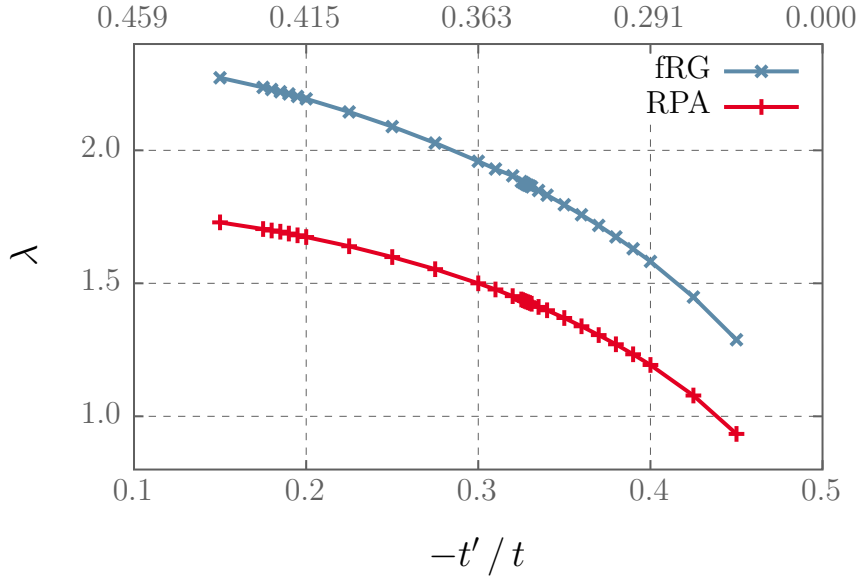

Figure 5.8. Screening lengths at scale $\Omega = 0.04\,t$ are plotted against the model parameter t', while the electron density (top horizontal axis) is adjusted concurrently to keep the system at van Hove filling. The figure compares the screening length computed from the fRG flow with the one resulting from RPA.

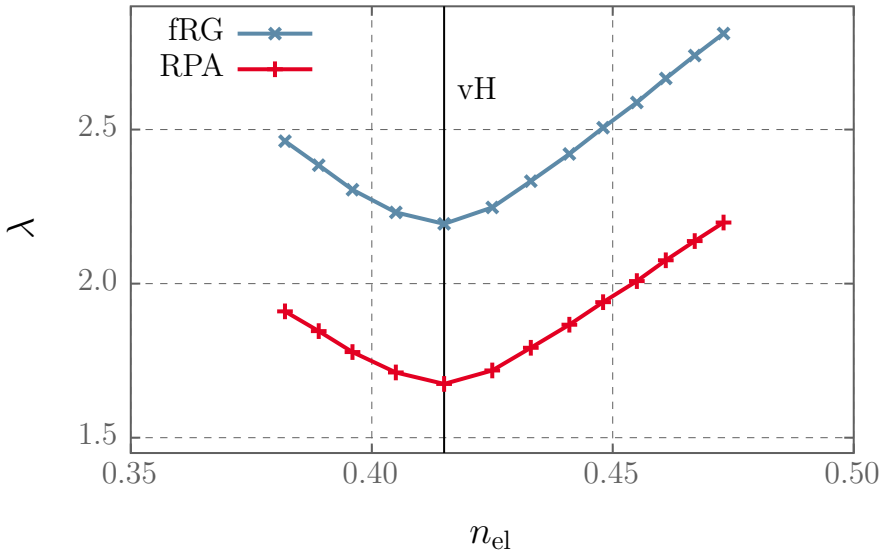

Figure 5.9. While t' is fixed to $-0.20\,t$, the screening length at scale $\Omega = 0.04\,t$ is shown as function of the electron density in the vicinity of van Hove filling. As in Fig. 5.8, the screening length computed from the fRG flow is compared with the one resulting from RPA.

In order to extract the screening length from the exchange propagators that are obtained from the fRG procedure, the particle-hole channels must be combined to the physical charge channel. The term

$$C^{\text{ch.}}_{0s,0s}(l) = D_{0s,0s}(l) - \frac{1}{2}C_{0s,0s}(l) \tag{5.16}$$

works as the mediator for interactions between charges and is therefore the analog to Eq. (5.11). Thus, the screening length is read off from the $l = 0$ component by

$$\lambda^{\Omega}_{\text{fRG}} = \frac{1}{e^2}\left[D_{0s,0s}(l=0) - \frac{1}{2}C_{0s,0s}(l=0)\right] . \tag{5.17}$$

The definitions that are used here to characterize the charge screening are certainly not unique, since the screening length's order of magnitude is much more meaningful than its exact number of lattice constants. In favor of a simple comparison, $\lambda^{\Omega}_{\text{RPA}}$ and $\lambda^{\Omega}_{\text{fRG}}$ are chosen to be compatible, i.e., their values are identical at the initial scale.

Fig. 5.7 compares the screening values from fRG and RPA as function of Ω for six different sets of model parameters. All six plots show a common characteristic: At high scales the curves run on top of each other. Thus the charge screening is not effected by other channels in this region. Between $\Omega = 10^1\, t$ and $\Omega = 10^0\, t$—i.e., at the order of the bandwidth—the curves split indicating an onset of important inter-channel feedback. According to Eq. (5.15), the RPA result is given by the inverse of the particle-hole loop, which at $\mathbf{l} = 0$ tends to the density of states at the Fermi level as Ω goes to zero. As the system is set to van Hove filling in the Plots 5.7a–5.7d, the density of states at the Fermi level exhibits a logarithmic divergence causing an inverse logarithmic decrease towards zero of the RPA curves at low Ω. The fRG data show a similar behavior, while in the Plots 5.7a–5.7c the screening effect is reduced in the fRG—i.e., the screening length is larger—compared to RPA. In the system corresponding to Plot 5.7d, however, the curves get close to each other again at the critical scale indicating that at lower scales screening effects could even get enhanced by inter-channel coupling in the FM dominated parameter region. In Plots 5.7e and 5.7f the situation is qualitatively different. The system parameter t' is set to the same value as in 5.7b but the electron densities are changed by hole and electron doping, respectively. Thus the density of states at the Fermi level changes from being singular to finite values. Consequently, the RPA curves tend towards a finite screening length as the scale goes to zero. The inter-channel coupling contained in the fRG reduces the strength of the screening leading to larger λ values, while the saturating behavior at low scales is unchanged.

In order to get a closer look at the values, Fig. 5.8 shows the screening lengths resulting from van Hove filled systems at a fixed value of the scale parameter. To be able to provide a broad view on most of the investigated parameter region,

this scale value is chosen to be larger than most of the critical scales found. Both curves from Fig. 5.8 follow a common trend, that is, the screening effects get enhanced continuously while changing t' from $-0.15\,t$ (AFM system) to $-0.45\,t$ (FM system). At the scale used here the screening length calculated in fRG is constantly larger than the one obtained in RPA by a factor of about 1.3. However, as shown in Fig. 5.7d this factor changes drastically at $t' = -0.4\,t$ when the scale is decreased.

To investigate the dependence of the screening length on the electron density, t' was fixed to $-0.2\,t$ and the scale was set to the same value as before. For these parameter values Fig. 5.9 shows that in the vicinity of van Hove filling the resulting fRG and RPA values of λ exhibit a similar behavior. While the strongest screening appears at van Hove filling, the screening lengths increase as the density of states at the Fermi level decreases. Like in the above investigation, the fRG curve is separated from the RPA one by an almost constant factor, which is again about 1.3. The Plots 5.7e and 5.7f show that the outermost data points in Fig. 5.9 are already close to their saturation value in the limit $\Omega \to 0$, while the curves in 5.7b suggest that at the van Hove point the fRG value—as the RPA value—tends to zero in that limit.

Chapter 6.

Conclusion and Outlook

In this thesis I report on the progress made during my PhD studies regarding investigations on interacting Fermi systems on square lattices using the fRG formalism. The progress described in the preceding chapters can be divided into four phases. In the first phase, a novel fRG scheme was developed on a formal level with a focus on efficient parametrization and—in terms of a numerical treatment—beneficially structured equations. The derivation of this scheme, introduced as TU approach or TUfRG, builds upon the level-two truncation of the fRG-equation hierarchy and uses a channel decomposition of the two-particle coupling in an exchange-parametrized form as introduced in Ref. [3]. It is argued that such a formulation results in an efficient representation. As shown in Ch. 3, the projection of weak momentum dependencies onto a form-factor basis followed by an insertion of truncated partitions of unity in this basis results in the TU equations that are reminiscent of the ones used in the SMFRG introduced in Ref. [4]. The relation of the TU approach and the SMFRG was analyzed and the benefits of the TUfRG as an exchange-propagator based approach were revealed. In a comparison to the original exchange-parametrization approach from Ref. [3] it was argued that the insertion of truncated partitions of unity simplifies the appearing integrations by separating fermionic and exchange propagators. Thereby, a computational advantage over the previous scheme was generated. This advantage was achieved at the cost of adding a projection task which, however, contains a high potential for optimization of its numerical evaluation. By exploiting this potential, its computational cost was reduced significantly below the one of the integration task.

In the second phase of this work, a program code for solving the equations derived in the first phase was implemented. To be able to treat highly resolved coupling functions, the code was designed to run on high-performance computers using a large number of compute cores in parallel. Thanks to the advantageous structure of the TU equations, both shared-memory and distributed-memory parallelizations were easily implemented, while the performance of the latter was not affected by inter-process communication. An investigation of the code's parallel performance conducted on the JURECA compute cluster showed convincing

speedups of 24.5 in the shared-memory case and an additional speedup of about 98 gained from distributed-memory parallelism. In these tests the highest speedups were obtained using almost 3100 cores. Consequently, by realizing these speedups it is shown that the program code developed in this work is capable of utilizing a few thousand compute cores.

The third phase was focused on the functionality of the developed approach. With this in view, the application of the TUfRG to the Hubbard model on the square lattice—a commonly used test case for fRG schemes—revealed promising conclusions, that is, the insertion of truncated partitions of unity turned out to be a suitable approximation leading to meaningful results. This was proved by the examination of two indicators: Firstly, in most of the investigated parameter range, a fast convergence of the results with respect to increasing truncation length was observed. Secondly, a comparison to the previous exchange-parametrization studies [3, 58] showed that the findings from the latter investigations are approximately reproduced by using a short truncation length within the TU approach, while quantitative corrections to those results are obtained by using higher-shell truncations. After this analysis on the method itself, the high momentum-space resolution of the implementation was utilized to study AFM ordering vectors. By comparing the ordering vectors resulting from the TU flow with ones from single-channel calculations, it was revealed that the interplay of different channels supports commensurate AFM order.

Finally, in the fourth phase the effects of adding a Coulomb-like long-range term to the local Hubbard U were investigated. To be able to do so, a solution on how a long-range interaction can be treated in a momentum-space fRG scheme without encountering singularities was developed. Since the additional long-range part has the potential to strongly influence the inter-channel feedback during the flow, a separate convergence test was necessary to reveal the best choices for technical adjustment parameters. As a result of such a test, in the space spanned by those parameters a convergence area was detected, in which the smallest suitable truncation length turned out larger than the one found in the study on the Hubbard model. By building on this accomplished preparatory work, converged results in a sufficiently high resolution were achieved in this study on long-range interactions. Regarding the comparison between the Hubbard-Coulomb and the Hubbard model at van Hove filling, a significant decrease in the critical scales was observed when the long-range part was added. In combination with the results from Ref. [71] these findings yield a consistent picture of destructive competition effects between incompatible ordering tendencies seeded by the initial long-range interaction. The second comparative study addressed the impact of varying electron densities on the critical scale in the AFM dominated region. This analysis showed that in the Hubbard-Coulomb model the appearance of AFM hot spots is crucial for high critical scales as it is in the Hubbard model (cf. Ref. [16]). However, the parameter range in which high-scale order appears is drastically reduced by the inclusion of initially long-range interactions, which underlines the

importance of the destructive competition effects found in Ref. [71]. Concerning the investigation on charge screening, this work pioneered in the extraction of screening lengths from the fRG flow. In a comparison of these screening lengths with those generated in RPA, a good agreement of the values was observed at high scales, while at low scales quantitative differences were found. However, the results indicate that the screening in the charge channel is not changed qualitatively by the feedback from other channels, i.e., as in RPA a divergent density of states at the Fermi level causes a vanishing fRG screening length.

In summary, the TU approach and its implementation presented here pioneer the combination of an efficiently parametrized coupling function within the fRG framework and a program code developed with focus on high-performance computation. These two aspects are essential for improving the quantitative accuracy of fRG methods far beyond the current state of the art. The level of accuracy can only be evaluated by conducting convergence tests as done in the applications presented here. Although form-factor representations had been used in other works before, the present study is the first that documents convergence with respect to a truncated expansion. Furthermore, the investigations presented in Ch. 5 are a first step towards examinations on infinitely long-range interactions in square-lattice systems. A similar investigation on the honeycomb lattice presented in Ref. [71] reveals qualitative changes compared to results computed using local interactions. Additional studies exploring the effects of long-range interactions in other systems seem worthwhile. In view of possible future investigations of that type, the following is important to note: In the present work, the treatment of such kind of interactions and, especially, the *quantitative* comparison to the results using a local interaction have only been possible due to the high resolution in momentum space and the large form-factor basis, as those properties were essential for including quantitatively important corrections.

Certainly, as it was shown by many studies (e.g., Refs. [58, 69]) that self-energy effects and frequency dependencies can have a strong impact on fRG flows, the TUfRG in the form presented here does only constitute a basic framework for further method developments. A thorough extension of the TU approach by these two named aspects would lift its predictive power to new levels.

Appendix A.

Parametrization of Single-Channel Couplings

The parametrization of the single-channel couplings is now discussed in more detail. As a starting point the channel decomposition of the two-particle coupling from Eq. (3.1) is repeated. However, in contrast to Eq. (3.1) the parametrization according to purely fermionic momenta is kept and frequency dependencies are ignored:

$$V(\mathbf{k_1},\mathbf{k_2},\mathbf{k_3}) = V^{(0)}_{\mathbf{k_1},\mathbf{k_2},\mathbf{k_3}} - \bar{\Phi}^{\mathrm{P}}(\mathbf{k_1},\mathbf{k_2},\mathbf{k_3}) + \bar{\Phi}^{\mathrm{C}}(\mathbf{k_1},\mathbf{k_2},\mathbf{k_3}) + \bar{\Phi}^{\mathrm{D}}(\mathbf{k_1},\mathbf{k_2},\mathbf{k_3}) \quad \text{(A.1)}$$

In the following the focus is on the particle-particle channel, while the other two channels can be treated analogously. Assuming a translation invariant system, the Fourier transformation that connects the coupling function in momentum-space representation with the direct-space one reads

$$\bar{\Phi}^{\mathrm{P}}(\mathbf{k_1},\mathbf{k_2},\mathbf{k_3}) = \sum_{\mathbf{R_1},\mathbf{R_2},\mathbf{R_3}} e^{i(\mathbf{k_1}\cdot\mathbf{R_1}+\mathbf{k_2}\cdot\mathbf{R_2}-\mathbf{k_3}\cdot\mathbf{R_3})}\ \bar{\Phi}^{\mathrm{P}}(\mathbf{R_1},\mathbf{R_2},\mathbf{R_3},\mathbf{0})\,. \quad \text{(A.2)}$$

The parametrization used in Eq. (3.1) can now be implemented in a transparent way by choosing

$$\mathbf{l} = \mathbf{k_1} + \mathbf{k_2} \quad ; \quad \mathbf{k} = \frac{\mathbf{k_1} - \mathbf{k_2}}{2} \quad ; \quad \mathbf{k}' = \frac{\mathbf{k_4} - \mathbf{k_3}}{2} \quad \text{(A.3)}$$

$$\text{with} \qquad \mathbf{k_4} = \mathbf{k_1} + \mathbf{k_2} - \mathbf{k_3}\,.$$

By resolving this for the fermionic momenta

$$\mathbf{k_1} = \mathbf{k} + \frac{\mathbf{l}}{2} \quad ; \quad \mathbf{k_2} = -\mathbf{k} + \frac{\mathbf{l}}{2} \quad ; \quad \mathbf{k_3} = -\mathbf{k}' + \frac{\mathbf{l}}{2} \quad \text{(A.4)}$$

and inserting those momenta back into Eq. (A.2), the single-channel coupling yields

$$\Phi^{\mathrm{P}}_{\mathbf{l},\mathbf{k},\mathbf{k}'} = \sum_{\mathbf{R_1},\mathbf{R_2},\mathbf{R_3}} e^{i\mathbf{l}\cdot(\frac{1}{2}(\mathbf{R_1}+\mathbf{R_2})-\frac{1}{2}\mathbf{R_3})}\ e^{i\mathbf{k}\cdot(\mathbf{R_1}-\mathbf{R_2})}\ e^{i\mathbf{k}'\cdot\mathbf{R_3}} \times\bar{\Phi}^{\mathrm{P}}(\mathbf{R_1},\mathbf{R_2},\mathbf{R_3},\mathbf{0})\,. \quad \text{(A.5)}$$

In this formulation the momenta $\mathbf{k}$ and $\mathbf{k}'$ are conjugate to the relative position vectors of the involved particles before and after the virtual process, respectively. As the coupling in this channel contains particle-particle contributions that cause superconducting instabilities, the important contributions in this channel usually appear at small absolute values of those relative position vectors. For instance, in the *d*SC case observed in this work the absolute value is equal to one lattice constant and close to an *s*-wave SC phase, as it appears in the attractive Hubbard model, the dominant relative vector is zero. Thus, the parametrization chosen in Eq. (A.3) appears as a reasonable choice in order to distinguish different ordering tendencies in this channel. Furthermore, it allows for treating the dependencies on $\mathbf{k}$ and $\mathbf{k}'$ as 'weak', which justifies the truncation of the form-factor basis at an upper length in the direct space.

Eq. (A.5) also illustrates the periodicity of $\Phi^{\mathrm{P}}_{\mathbf{l},\mathbf{k},\mathbf{k}'}$. As $\mathbf{R_1}$, $\mathbf{R_2}$, and $\mathbf{R_3}$ are lattice vectors, all information from the dependence on $\mathbf{k}$ and $\mathbf{k}'$ is contained in the first BZ. The vector conjugate to $\mathbf{l}$, however, is equal to half a lattice vector, i.e., a part of the components from the sum is invariant under a shift of $\mathbf{l}$ by any vector from the reciprocal lattice, while the other components can pick up a minus sign under these operations. In an implementation based on the above parametrization this property has to be considered.

Appendix B.

Implementational Details on Projection Operations

The feedback terms that have to be evaluated in the projection step read:

$$\begin{aligned}\hat{P}[\Phi^{\mathrm{C}}]_{m,n}(l) \approx & \int d\mathbf{k}\, d\mathbf{k}'\ f_m^*(\mathbf{k})\ f_n(\mathbf{k}') \\ & \times \sum_{m',n'} f_{m'}\left(\frac{\mathbf{l}+\mathbf{k}-\mathbf{k}'}{2}\right)\ f_{n'}^*\left(\frac{\mathbf{l}-\mathbf{k}+\mathbf{k}'}{2}\right)\ C_{m',n'}(k'+k)\Big|_{k_0=k_0'=0}\end{aligned} \tag{B.1}$$

$$\begin{aligned}= & \sum_{\mathbf{R_1},\mathbf{R_2},\mathbf{R_3}} \sum_{m',n'} f_m^*\left(\frac{\mathbf{R_1}}{2}+\frac{\mathbf{R_2}}{2}+\mathbf{R_3}\right)\ f_n\left(\frac{\mathbf{R_1}}{2}+\frac{\mathbf{R_2}}{2}-\mathbf{R_3}\right) \\ & \times f_{m'}(\mathbf{R_1})\ f_{n'}^*(\mathbf{R_2})\ C_{m',n'}(k_0=0,\mathbf{R_3})\ e^{-i\frac{1}{2}\mathbf{l}\cdot(\mathbf{R_1}-\mathbf{R_2})}\end{aligned} \tag{B.2}$$

$$\begin{aligned}\hat{P}[\Phi^{\mathrm{D}}]_{m,n}(l) \approx & \int d\mathbf{k}\, d\mathbf{k}'\ f_m^*(\mathbf{k})\ f_n(\mathbf{k}') \\ & \times \sum_{m',n'} f_{m'}\left(\frac{\mathbf{l}+\mathbf{k}+\mathbf{k}'}{2}\right)\ f_{n'}^*\left(\frac{\mathbf{l}-\mathbf{k}-\mathbf{k}'}{2}\right)\ D_{m',n'}(k-k')\Big|_{k_0=k_0'=0}\end{aligned} \tag{B.3}$$

$$\begin{aligned}= & \sum_{\mathbf{R_1},\mathbf{R_2},\mathbf{R_3}} \sum_{m',n'} f_m^*\left(\frac{\mathbf{R_1}}{2}+\frac{\mathbf{R_2}}{2}+\mathbf{R_3}\right)\ f_n\left(-\frac{\mathbf{R_1}}{2}-\frac{\mathbf{R_2}}{2}+\mathbf{R_3}\right) \\ & \times f_{m'}(\mathbf{R_1})\ f_{n'}^*(\mathbf{R_2})\ D_{m',n'}(k_0=0,\mathbf{R_3})\ e^{-i\frac{1}{2}\mathbf{l}\cdot(\mathbf{R_1}-\mathbf{R_2})}\end{aligned} \tag{B.4}$$

$$\begin{aligned}\hat{C}[\Phi^{\mathrm{P}}]_{m,n}(l) \approx & \int d\mathbf{k}\, d\mathbf{k}'\ f_m^*(\mathbf{k})\ f_n(\mathbf{k}') \\ & \times \sum_{m',n'} f_{m'}\left(\frac{\mathbf{k}-\mathbf{k}'+\mathbf{l}}{2}\right)\ f_{n'}^*\left(\frac{\mathbf{k}'-\mathbf{k}+\mathbf{l}}{2}\right)\ P_{m',n'}(k+k')\Big|_{k_0=k_0'=0}\end{aligned} \tag{B.5}$$

$$= \sum_{\mathbf{R_1},\mathbf{R_2},\mathbf{R_3}} \sum_{m',n'} f_m^*\left(\frac{\mathbf{R_1}}{2} + \frac{\mathbf{R_2}}{2} + \mathbf{R_3}\right)\, f_n\left(\frac{\mathbf{R_1}}{2} + \frac{\mathbf{R_2}}{2} - \mathbf{R_3}\right) \times f_{m'}(\mathbf{R_1})\; f_{n'}^*(\mathbf{R_2})\; P_{m',n'}(k_0 = 0, \mathbf{R_3})\; e^{-i\frac{1}{2}\mathbf{l}\cdot(\mathbf{R_1}-\mathbf{R_2})} \tag{B.6}$$

$$\hat{C}[\Phi^{\mathrm{D}}]_{m,n}(l) \approx \int d\mathbf{k}\, d\mathbf{k}'\; f_m^*(\mathbf{k})\; f_n(\mathbf{k}') \times \sum_{m',n'} f_{m'}\left(\frac{\mathbf{k}+\mathbf{k}'+\mathbf{l}}{2}\right)\; f_{n'}^*\left(\frac{\mathbf{k}+\mathbf{k}'-\mathbf{l}}{2}\right)\; D_{m',n'}(k-k')\Big|_{k_0=k_0'=0} \tag{B.7}$$

$$= \sum_{\mathbf{R_1},\mathbf{R_2},\mathbf{R_3}} \sum_{m',n'} f_m^*\left(\frac{\mathbf{R_1}}{2} - \frac{\mathbf{R_2}}{2} + \mathbf{R_3}\right)\, f_n\left(-\frac{\mathbf{R_1}}{2} + \frac{\mathbf{R_2}}{2} + \mathbf{R_3}\right) \times f_{m'}(\mathbf{R_1})\; f_{n'}^*(\mathbf{R_2})\; D_{m',n'}(k_0 = 0, \mathbf{R_3})\; e^{-i\frac{1}{2}\mathbf{l}\cdot(\mathbf{R_1}+\mathbf{R_2})} \tag{B.8}$$

$$\hat{D}[\Phi^{\mathrm{P}}]_{m,n}(l) \approx \int d\mathbf{k}\, d\mathbf{k}'\; f_m^*(\mathbf{k})\; f_n(\mathbf{k}') \times \sum_{m',n'} f_{m'}\left(\frac{\mathbf{k}-\mathbf{k}'+\mathbf{l}}{2}\right)\; f_{n'}^*\left(\frac{\mathbf{k}-\mathbf{k}'-\mathbf{l}}{2}\right)\; P_{m',n'}(k+k')\Big|_{k_0=k_0'=0} \tag{B.9}$$

$$= \sum_{\mathbf{R_1},\mathbf{R_2},\mathbf{R_3}} \sum_{m',n'} f_m^*\left(\frac{\mathbf{R_1}}{2} - \frac{\mathbf{R_2}}{2} + \mathbf{R_3}\right)\, f_n\left(\frac{\mathbf{R_1}}{2} - \frac{\mathbf{R_2}}{2} - \mathbf{R_3}\right) \times f_{m'}(\mathbf{R_1})\; f_{n'}^*(\mathbf{R_2})\; P_{m',n'}(k_0 = 0, \mathbf{R_3})\; e^{-i\frac{1}{2}\mathbf{l}\cdot(\mathbf{R_1}+\mathbf{R_2})} \tag{B.10}$$

$$\hat{D}[\Phi^{\mathrm{C}}]_{m,n}(l) \approx \int d\mathbf{k}\, d\mathbf{k}'\; f_m^*(\mathbf{k})\; f_n(\mathbf{k}') \times \sum_{m',n'} f_{m'}\left(\frac{\mathbf{k}+\mathbf{k}'+\mathbf{l}}{2}\right)\; f_{n'}^*\left(\frac{\mathbf{k}+\mathbf{k}'-\mathbf{l}}{2}\right)\; C_{m',n'}(k-k')\Big|_{k_0=k_0'=0} \tag{B.11}$$

$$= \sum_{\mathbf{R_1},\mathbf{R_2},\mathbf{R_3}} \sum_{m',n'} f_m^*\left(\frac{\mathbf{R_1}}{2} - \frac{\mathbf{R_2}}{2} + \mathbf{R_3}\right)\, f_n\left(-\frac{\mathbf{R_1}}{2} + \frac{\mathbf{R_2}}{2} + \mathbf{R_3}\right) \times f_{m'}(\mathbf{R_1})\; f_{n'}^*(\mathbf{R_2})\; C_{m',n'}(k_0 = 0, \mathbf{R_3})\; e^{-i\frac{1}{2}\mathbf{l}\cdot(\mathbf{R_1}+\mathbf{R_2})} \tag{B.12}$$

For the implementation of the projection step, the position-space representations of the above formulas were used. In the following, some details regarding the implementation of those formulas are provided in note form:

- The sums over m' and n' are implemented as outermost loops (even further out than the loops over m, n, and $\mathbf{l}$) and are distributed over the compute nodes using MPI. This is done to be able to do the Fourier transforms of one exchange propagator component (characterized by m', n') only once.

- In order to improve the load balancing of the shared-memory parallelization, the m', n' loops contain two separate blocks:

  - The first block loops over all m, n, $\mathbf{R_1}$, and $\mathbf{R_2}$ combinations—this loop is parallelized using OpenMP—and searches for all non-vanishing overlaps of the four form factors. At a fixed combination of m, n, $\mathbf{R_1}$, and $\mathbf{R_2}$ the sum over $\mathbf{R_3}$ is performed, while for each non-vanishing contribution the product of the form factors and the exchange propagator is evaluated and added to the sum. The result of this summation and its 'identifying values' m, n, $\mathbf{R_1}$, and $\mathbf{R_2}$ are stored in a container. Here, it is crucial for the runtime of the code that only the non-vanishing contributions are stored, i.e., the identifiers are discarded if the R_3 sum did not yield any overlap of the form factors.

  - In the second block the non-vanishing contributions and their identifiers are successively taken from the container. This is done in an OpenMP-parallelized loop. Within an internal loop over $\mathbf{l}$, the contributions are multiplied with the remaining exponential term and added to the corresponding component of the projected two-particle coupling.

- As discussed in Appendix A, for the position space vector that is conjugate to the momentum dependence of the exchange propagators, one has to consider halves of lattice vectors, i.e., in the notation from Eqs. (B.1)–(B.12) $\mathbf{R_3}$ can be written as $\frac{1}{2}\mathbf{R}$ with $\mathbf{R}$ being a lattice vector. However, despite the fact that the periodicity of the exchange propagators in momentum space is different from the one of the reciprocal lattice, the Fourier transformation can be performed within the first BZ. The reason is the following: As the lattice vectors $\mathbf{R_1}$ and $\mathbf{R_2}$ control both the periodicity of the exchange propagator and the value of $\mathbf{R_3}$ (lattice vector or half a lattice vector) in the same way, pulling the m', n' sums into the Fourier integral of the exchange propagator leads to an integrand that always exhibits the periodicity of the reciprocal lattice.

Furthermore, additional ideas, that are not implemented in the current code version but may be worthwhile for future works, are listed next:

- As the overlapping form-factor combinations do not change during the flow, it is possible to perform the search for quadruples $(m, n, \mathbf{R_1}, \mathbf{R_2})$ leading to non-vanishing contributions only once, for fixed m' and n'. Reusing—as compared with recomputing—these data may save computation time.

- During the code development it was observed that reusing the Fourier transformed (position space) exchange propagators—within one evaluation of the flow equation's right-hand side—could save a huge part of the computation time used by the projection step. Thus, as the set of possible $\mathbf{R_3}$ vectors is limited, computing and tabulating all relevant Fourier transforms at the beginning of the projection step could be worthwhile.

Appendix C.

Full Description of the Form-Factor Basis

The set of form factors corresponding to a bond with position vector $\mathbf{R} = n\,\mathbf{x} + l\,\mathbf{y}$ from an irreducible segment of the square lattice (here $n \geq 0$ and $0 \leq l \leq n$ is used; see Fig. 3.1) can be read off in momentum-space representation from the following case differentiation:

If $n = 0$:

$$f_s(\mathbf{k}) = 1$$

Otherwise, if $l = 0$:

$$f_s(\mathbf{k}) = \cos(n\,k_x) + \cos(n\,k_y)$$

$$f_{d_{x^2-y^2}}(\mathbf{k}) = \cos(n\,k_x) - \cos(n\,k_y)$$

$$f_{p_x}(\mathbf{k}) = \sqrt{2}\,\sin(n\,k_x)$$

$$f_{p_y}(\mathbf{k}) = \sqrt{2}\,\sin(n\,k_y)$$

Otherwise, if $n = l$:

$$f_s(\mathbf{k}) = \cos(n\,(k_x + k_y)) + \cos(n\,(k_x - k_y))$$

$$f_{d_{xy}}(\mathbf{k}) = \cos(n\,(k_x + k_y)) - \cos(n\,(k_x - k_y))$$

$$f_{p_{x+y}}(\mathbf{k}) = \sqrt{2}\,\sin(n\,(k_x + k_y))$$

$$f_{p_{x-y}}(\mathbf{k}) = \sqrt{2}\,\sin(n\,(k_x - k_y))$$

Otherwise:

$$f_s(\mathbf{k}) = \frac{1}{\sqrt{2}} \big(\cos(n\,k_x + l\,k_y) + \cos(-l\,k_x + n\,k_y) + \cos(n\,k_x - l\,k_y) + \cos(l\,k_x + n\,k_y) \big)$$

$$f_g(\mathbf{k}) = \frac{1}{\sqrt{2}} \big(\cos(n\,k_x + l\,k_y) + \cos(-l\,k_x + n\,k_y) - \cos(n\,k_x - l\,k_y) - \cos(l\,k_x + n\,k_y) \big)$$

$$f_{d_{x^2-y^2}}(\mathbf{k}) = \frac{1}{\sqrt{2}} \big(\cos(n\,k_x + l\,k_y) - \cos(-l\,k_x + n\,k_y) + \cos(n\,k_x - l\,k_y) - \cos(l\,k_x + n\,k_y) \big)$$

$$f_{d_{xy}}(\mathbf{k}) = \frac{1}{\sqrt{2}} \big(\cos(n\,k_x + l\,k_y) - \cos(-l\,k_x + n\,k_y) - \cos(n\,k_x - l\,k_y) + \cos(l\,k_x + n\,k_y) \big)$$

$$f_{p_1}(\mathbf{k}) = \sqrt{2}\,\sin(n\,k_x + l\,k_y)$$

$$f_{p_2}(\mathbf{k}) = \sqrt{2}\,\sin(l\,k_x + n\,k_y)$$

$$f_{p_3}(\mathbf{k}) = \sqrt{2}\,\sin(n\,k_x - l\,k_y)$$

$$f_{p_4}(\mathbf{k}) = \sqrt{2}\,\sin(-l\,k_x + n\,k_y)$$

Bibliography

[1] Sebastian Luehrs, Daniel Rohe, Alexander Schnurpfeil, Kay Thust, and Wolfgang Frings. Flexible and Generic Workflow Management. *Advances in Parallel Computing*, 27(Parallel Computing: On the Road to Exascale):431–438, 2016.

[2] Jülich Supercomputing Centre. JURECA: General-purpose supercomputer at Jülich Supercomputing Centre. *Journal of large-scale research facilities*, 2(A62), 2016.

[3] C. Husemann and M. Salmhofer. Efficient parametrization of the vertex function, Ω scheme, and the t, t' Hubbard model at van Hove filling. *Phys. Rev. B*, 79:195125, May 2009.

[4] Wan-Sheng Wang, Yuan-Yuan Xiang, Qiang-Hua Wang, Fa Wang, Fan Yang, and Dung-Hai Lee. Functional renormalization group and variational Monte Carlo studies of the electronic instabilities in graphene near $\frac{1}{4}$ doping. *Phys. Rev. B*, 85:035414, Jan 2012.

[5] P. W. Anderson. More Is Different. *Science*, 177(4047):393–396, 1972.

[6] John Hubbard. Electron correlations in narrow energy bands. *Proceedings of the Royal Society of London A: Mathematical, Physical and Engineering Sciences*, 276(1365):238–257, 1963.

[7] Martin C. Gutzwiller. Effect of Correlation on the Ferromagnetism of Transition Metals. *Phys. Rev. Lett.*, 10:159–162, Mar 1963.

[8] Junjiro Kanamori. Electron Correlation and Ferromagnetism of Transition Metals. *Progress of Theoretical Physics*, 30(3):275–289, 1963.

[9] P. W. Anderson. The Resonating Valence Bond State in La2CuO4 and Superconductivity. *Science*, 235(4793):1196–1198, 1987.

[10] D. J. Scalapino, E. Loh, and J. E. Hirsch. *d*-wave pairing near a spin-density-wave instability. *Phys. Rev. B*, 34:8190–8192, Dec 1986.

[11] Kenneth G. Wilson and J. Kogut. The renormalization group and the ϵ expansion. *Physics Reports*, 12(2):75 – 199, 1974.

[12] Walter Metzner, Manfred Salmhofer, Carsten Honerkamp, Volker Meden, and Kurt Schönhammer. Functional renormalization group approach to correlated fermion systems. *Rev. Mod. Phys.*, 84:299–352, Mar 2012.

[13] C. Platt, W. Hanke, and R. Thomale. Functional renormalization group for multi-orbital Fermi surface instabilities. *Advances in Physics*, 62(4-6):453–562, 2013.

[14] Christof Wetterich. Exact evolution equation for the effective potential. *Physics Letters B*, 301(1):90 – 94, 1993.

[15] Manfred Salmhofer and Carsten Honerkamp. Fermionic Renormalization Group Flows: Technique and Theory. *Progress of Theoretical Physics*, 105(1):1–35, 2001.

[16] C. Honerkamp, M. Salmhofer, N. Furukawa, and T. M. Rice. Breakdown of the Landau-Fermi liquid in two dimensions due to umklapp scattering. *Phys. Rev. B*, 63:035109, Jan 2001.

[17] C. Karrasch, R. Hedden, R. Peters, Th. Pruschke, K. Schönhammer, and V. Meden. A finite-frequency functional renormalization group approach to the single impurity Anderson model. *Journal of Physics: Condensed Matter*, 20(34):345205, 2008.

[18] A. A. Katanin. Fulfillment of Ward identities in the functional renormalization group approach. *Phys. Rev. B*, 70:115109, Sep 2004.

[19] Daniel Rohe. Hierarchical parallelisation of functional renormalisation group calculations hp-fRG. *Computer Physics Communications*, 207:160 – 169, 2016.

[20] J. Lichtenstein, D. Sánchez de la Peña, D. Rohe, E. Di Napoli, C. Honerkamp, and S.A. Maier. High-performance functional Renormalization Group calculations for interacting fermions. *Computer Physics Communications*, 213:100–110, 2017.

[21] John W. Negele and Henri Orland. *Quantum Many-Particle Systems*. Addison-Wesley, 1988.

[22] Andreas Eberlein and Walter Metzner. Parametrization of Nambu Vertex in a Singlet Superconductor. *Progress of Theoretical Physics*, 124(3):471–491, 2010.

[23] Stefan A. Maier and Carsten Honerkamp. Renormalization group flow for fermions into antiferromagnetically ordered phases: Method and mean-field models. *Phys. Rev. B*, 86:134404, Oct 2012.

[24] Jing Wang, Andreas Eberlein, and Walter Metzner. Competing order in correlated electron systems made simple: Consistent fusion of functional renormalization and mean-field theory. *Phys. Rev. B*, 89:121116, Mar 2014.

[25] Carsten Honerkamp and Manfred Salmhofer. Temperature-flow renormalization group and the competition between superconductivity and ferromagnetism. *Phys. Rev. B*, 64:184516, Oct 2001.

[26] Carsten Honerkamp, Daniel Rohe, Sabine Andergassen, and Tilman Enss. Interaction flow method for many-fermion systems. *Phys. Rev. B*, 70:235115, Dec 2004.

[27] Manfred Salmhofer, Carsten Honerkamp, Walter Metzner, and Oliver Lauscher. Renormalization Group Flows into Phases with Broken Symmetry. *Progress of Theoretical Physics*, 112(6):943–970, 2004.

[28] R Gersch, C Honerkamp, and W Metzner. Superconductivity in the attractive Hubbard model: functional renormalization group analysis. *New Journal of Physics*, 10(4):045003, 2008.

[29] Andreas Eberlein and Walter Metzner. Effective interactions and fluctuation effects in spin-singlet superfluids. *Phys. Rev. B*, 87:174523, May 2013.

[30] Andreas Eberlein and Walter Metzner. Superconductivity in the two-dimensional t-t'-Hubbard model. *Phys. Rev. B*, 89:035126, Jan 2014.

[31] C. Platt. *A Common Thread in Unconventional Superconductivity: The Functional Renormalization Group in Multi-Band Systems*. PhD thesis, Universität Würzburg, 2012.

[32] D. Zanchi and H. J. Schulz. Weakly correlated electrons on a square lattice: A renormalization group theory. *EPL (Europhysics Letters)*, 44(2):235, 1998.

[33] D. Zanchi and H. J. Schulz. Weakly correlated electrons on a square lattice: Renormalization-group theory. *Phys. Rev. B*, 61:13609–13632, May 2000.

[34] Carsten Honerkamp and Manfred Salmhofer. Magnetic and Superconducting Instabilities of the Hubbard Model at the Van Hove Filling. *Phys. Rev. Lett.*, 87:187004, Oct 2001.

[35] Honerkamp, C., Salmhofer, M., and Rice, T. M. Flow to strong coupling in the two-dimensional Hubbard model. *Eur. Phys. J. B*, 27(1):127–134, 2002.

[36] Honerkamp, C. Electron-doping versus hole-doping in the 2D t-t' Hubbard model. *Eur. Phys. J. B*, 21(1):81–91, 2001.

[37] Carsten Honerkamp. Density Waves and Cooper Pairing on the Honeycomb Lattice. *Phys. Rev. Lett.*, 100:146404, Apr 2008.

[38] S. Raghu, Xiao-Liang Qi, C. Honerkamp, and Shou-Cheng Zhang. Topological Mott Insulators. *Phys. Rev. Lett.*, 100:156401, Apr 2008.

[39] Maximilian L. Kiesel, Christian Platt, Werner Hanke, Dmitry A. Abanin, and Ronny Thomale. Competing many-body instabilities and unconventional superconductivity in graphene. *Phys. Rev. B*, 86:020507, Jul 2012.

[40] Wei Wu, Michael M. Scherer, Carsten Honerkamp, and Karyn Le Hur. Correlated Dirac particles and superconductivity on the honeycomb lattice. *Phys. Rev. B*, 87:094521, Mar 2013.

[41] Michael M. Scherer, Stefan Uebelacker, and Carsten Honerkamp. Instabilities of interacting electrons on the honeycomb bilayer. *Phys. Rev. B*, 85:235408, Jun 2012.

[42] Thomas C. Lang, Zi Yang Meng, Michael M. Scherer, Stefan Uebelacker, Fakher F. Assaad, Alejandro Muramatsu, Carsten Honerkamp, and Stefan Wessel. Antiferromagnetism in the Hubbard Model on the Bernal-Stacked Honeycomb Bilayer. *Phys. Rev. Lett.*, 109:126402, Sep 2012.

[43] David Sánchez de la Peña, Michael M. Scherer, and Carsten Honerkamp. Electronic instabilities of the AA-honeycomb bilayer. *Annalen der Physik*, 526(9-10):366–371, 2014.

[44] Michael M. Scherer, Stefan Uebelacker, Daniel D. Scherer, and Carsten Honerkamp. Interacting electrons on trilayer honeycomb lattices. *Phys. Rev. B*, 86:155415, Oct 2012.

[45] Daniel D. Scherer, Michael M. Scherer, and Carsten Honerkamp. Correlated spinless fermions on the honeycomb lattice revisited. *Phys. Rev. B*, 92:155137, Oct 2015.

[46] Yanick Volpez, Daniel D. Scherer, and Michael M. Scherer. Electronic instabilities of the extended Hubbard model on the honeycomb lattice from functional renormalization. *Phys. Rev. B*, 94:165107, Oct 2016.

[47] Fa Wang, Hui Zhai, Ying Ran, Ashvin Vishwanath, and Dung-Hai Lee. Functional Renormalization-Group Study of the Pairing Symmetry and Pairing Mechanism of the FeAs-Based High-Temperature Superconductor. *Phys. Rev. Lett.*, 102:047005, Jan 2009.

[48] Fa Wang, Hui Zhai, and Dung-Hai Lee. Antiferromagnetic correlation and the pairing mechanism of the cuprates and iron pnictides: A view from the functional renormalization group studies. *EPL (Europhysics Letters)*, 85(3):37005, 2009.

[49] Fa Wang, Hui Zhai, and Dung-Hai Lee. Nodes in the gap function of LaFePO, the gap function of the Fe(Se,Te) systems, and the STM signature of the $s_{\pm}$ pairing. *Phys. Rev. B*, 81:184512, May 2010.

[50] W. Hanke, Ch. Platt, and R. Thomale. Order-parameter anisotropies in the pnictides: An optimization principle for multi-band superconductivity. *Annalen der Physik*, 523(8-9):638–644, 2011.

[51] Ronny Thomale, Christian Platt, Werner Hanke, and B. Andrei Bernevig. Mechanism for Explaining Differences in the Order Parameters of FeAs-Based and FeP-Based Pnictide Superconductors. *Phys. Rev. Lett.*, 106:187003, May 2011.

[52] Ronny Thomale, Christian Platt, Werner Hanke, Jiangping Hu, and B. Andrei Bernevig. Exotic *d*-Wave Superconducting State of Strongly Hole-Doped $\mathbf{K}_x\mathrm{Ba}_{1-x}\mathrm{Fe}_2\mathrm{As}_2$. *Phys. Rev. Lett.*, 107:117001, Sep 2011.

[53] Christian Platt, Ronny Thomale, and Werner Hanke. Superconducting state of the iron pnictide LiFeAs: A combined density-functional and functional-renormalization-group study. *Phys. Rev. B*, 84:235121, Dec 2011.

[54] Christian Platt, Ronny Thomale, Carsten Honerkamp, Shou-Cheng Zhang, and Werner Hanke. Mechanism for a pairing state with time-reversal symmetry breaking in iron-based superconductors. *Phys. Rev. B*, 85:180502, May 2012.

[55] J. Lichtenstein, S. A. Maier, C. Honerkamp, C. Platt, R. Thomale, O. K. Andersen, and L. Boeri. Functional renormalization group study of an eight-band model for the iron arsenides. *Phys. Rev. B*, 89:214514, Jun 2014.

[56] Ronny Thomale, Christian Platt, Jiangping Hu, Carsten Honerkamp, and B. Andrei Bernevig. Functional renormalization-group study of the doping dependence of pairing symmetry in the iron pnictide superconductors. *Phys. Rev. B*, 80:180505, Nov 2009.

[57] Christoph Husemann and Walter Metzner. Incommensurate nematic fluctuations in the two-dimensional Hubbard model. *Phys. Rev. B*, 86:085113, Aug 2012.

[58] C. Husemann, K.-U. Giering, and M. Salmhofer. Frequency-dependent vertex functions of the (t, t') Hubbard model at weak coupling. *Phys. Rev. B*, 85:075121, Feb 2012.

[59] Kay-Uwe Giering and Manfred Salmhofer. Self-energy flows in the two-dimensional repulsive Hubbard model. *Phys. Rev. B*, 86:245122, Dec 2012.

[60] Stefan A. Maier, Andreas Eberlein, and Carsten Honerkamp. Functional renormalization group for commensurate antiferromagnets: Beyond the mean-field picture. *Phys. Rev. B*, 90:035140, Jul 2014.

[61] Stefan A. Maier, Jutta Ortloff, and Carsten Honerkamp. Multiorbital effects in the functional renormalization group: A weak-coupling study of the Emery model. *Phys. Rev. B*, 88:235112, Dec 2013.

[62] Hiroyuki Yamase, Andreas Eberlein, and Walter Metzner. Coexistence of Incommensurate Magnetism and Superconductivity in the Two-Dimensional Hubbard Model. *Phys. Rev. Lett.*, 116:096402, Mar 2016.

[63] Wan-Sheng Wang, Zheng-Zhao Li, Yuan-Yuan Xiang, and Qiang-Hua Wang. Competing electronic orders on kagome lattices at van Hove filling. *Phys. Rev. B*, 87:115135, Mar 2013.

[64] Yuan-Yuan Xiang, Yang Yang, Wan-Sheng Wang, Zheng-Zao Li, and Qiang-Hua Wang. Functional renormalization group study of pairing symmetry and pairing mechanism in iron-selenide superconductors. *Phys. Rev. B*, 88:104516, Sep 2013.

[65] Wan-Sheng Wang, Miao Gao, Yang Yang, Yuan-Yuan Xiang, and Qiang-Hua Wang. Possible superconductivity in the electron-doped chromium pnictide LaOCrAs. *Phys. Rev. B*, 95:144507, Apr 2017.

[66] Julian Lichtenstein, Jan Winkelmann, David Sánchez de la Peña, Toni Vidović, and Edoardo Di Napoli. Parallel Adaptive Integration in High-Performance Functional Renormalization Group Computations. In Edoardo Di Napoli, Marc-André Hermanns, Hristo Iliev, Andreas Lintermann, and Alexander Peyser, editors, *JHPCS 2016: High-Performance Scientific Computing*, volume 10164 of *Lecture Notes in Computer Science*, pages 170–184, Cham, 2017. Springer International Publishing.

[67] Jarle Berntsen, Terje O. Espelid, and Alan Genz. Algorithm 698: DCUHRE: An Adaptive Multidemensional Integration Routine for a Vector of Integrals. *ACM Trans. Math. Softw.*, 17(4):452–456, December 1991.

[68] Karsten Ahnert and Mario Mulansky. Odeint Solving Ordinary Differential Equations in C++. *AIP Conference Proceedings*, 1389(1):1586–1589, 2011.

[69] Andreas Eberlein. Self-energy effects in functional renormalization group flows of the two-dimensional t-t' Hubbard model away from van Hove filling. *Phys. Rev. B*, 92:235146, Dec 2015.

[70] J. P. F. LeBlanc, Andrey E. Antipov, Federico Becca, Ireneusz W. Bulik, Garnet Kin-Lic Chan, Chia-Min Chung, Youjin Deng, Michel Ferrero, Thomas M. Henderson, Carlos A. Jiménez-Hoyos, E. Kozik, Xuan-Wen Liu,

Andrew J. Millis, N. V. Prokof'ev, Mingpu Qin, Gustavo E. Scuseria, Hao Shi, B. V. Svistunov, Luca F. Tocchio, I. S. Tupitsyn, Steven R. White, Shiwei Zhang, Bo-Xiao Zheng, Zhenyue Zhu, and Emanuel Gull. Solutions of the Two-Dimensional Hubbard Model: Benchmarks and Results from a Wide Range of Numerical Algorithms. *Phys. Rev. X*, 5:041041, Dec 2015.

[71] David Sánchez de la Peña, Julian Lichtenstein, Carsten Honerkamp, and Michael M. Scherer. Antiferromagnetism and competing charge instabilities of electrons in strained graphene from Coulomb interactions. *Phys. Rev. B*, 96:205155, Nov 2017.

[72] Naoto Nagaosa. *Quantum Field Theory in Condensed Matter Physics*. Springer, 1999.

[73] P. Hansmann, T. Ayral, L. Vaugier, P. Werner, and S. Biermann. Long-Range Coulomb Interactions in Surface Systems: A First-Principles Description within Self-Consistently Combined *GW* and Dynamical Mean-Field Theory. *Phys. Rev. Lett.*, 110:166401, Apr 2013.

[74] D Pines and P Nozières. *The Theory of Quantum Liquids: Normal Fermi liquids*. Addison-Wesley Publishing Co., 1989.

List of Publications

While I have compiled this thesis solely by myself, parts of it have already been published in previous articles. The work presented in these articles has been done in collaboration with the authors listed below, which I cordially appreciate. The following publication forms the basis of Chs. 3, and 4 and is also incorporated in Chs. 1, and 6:

- J. Lichtenstein, D. Sánchez de la Peña, D. Rohe, E. Di Napoli, C. Honerkamp, and S.A. Maier. High-performance functional Renormalization Group calculations for interacting fermions. *Computer Physics Communications*, 213:100–110, 2017.

Moreover, the work presented in the next publication is recapitulated in a small part of Ch. 3:

- J. Lichtenstein, J. Winkelmann, D. Sánchez de la Peña, T. Vidović, and E. Di Napoli. Parallel Adaptive Integration in High-Performance Functional Renormalization Group Computations. In E. Di Napoli, M.-A. Hermanns, H. Iliev, A. Lintermann, and A. Peyser, editors, *JHPCS 2016: High-Performance Scientific Computing*, volume 10164 of *Lecture Notes in Computer Science*, pages 170–184, Cham, 2017. Springer International Publishing.

Further articles that I contributed to during my time as a PhD student are not part of this thesis:

- D. Sánchez de la Peña, J. Lichtenstein, and C. Honerkamp. Competing electronic instabilities of extended Hubbard models on the honeycomb lattice: A functional renormalization group calculation with high-wave-vector resolution. *Phys. Rev. B*, 95:085143, Feb 2017.

- D. Sánchez de la Peña, J. Lichtenstein, C. Honerkamp, and M. M. Scherer. Antiferromagnetism and competing charge instabilities of electrons in strained graphene from Coulomb interactions. *Phys. Rev. B*, 96:205155, Nov 2017.

The following publication, which outgrew my Master's thesis, is likewise not part of the present thesis:

- J. Lichtenstein, S. A. Maier, C. Honerkamp, C. Platt, R. Thomale, O. K. Andersen, and L. Boeri. Functional renormalization group study of an eight-band model for the iron arsenides. *Phys. Rev. B*, 89:214514, Jun 2014.